LASER-ASSISTED ADVANCED ASSEMBLY FOR MEMS FABRICATION

A Dissertation
Submitted to the Graduate Faculty
of the
North Dakota State University
of Agriculture and Applied Science

By

Yuriy Andreev Atanasov

In Partial Fulfillment of the Requirements
for the Degree
DOCTOR OF PHILOSOPHY

Major Program:
Materials and Nanotechnology

May 2014

Fargo, North Dakota

North Dakota State University
Graduate School

Title

LASER-ASSISTED ADVANCED ASSEMBLY FOR MEMS FABRICATION

By

Yuriy Andreev Atanasov

The Supervisory Committee certifies that this ***disquisition*** complies with North Dakota State University's regulations and meets the accepted standards for the degree of

DOCTOR OF PHILOSOPHY

SUPERVISORY COMMITTEE:

Dr. Val Marinov
Chair

Dr. Orven Swenson

Dr. Xinnan Wang

Dr. Fardad Azarmi

Dr. Benjamin Braaten

Approved:

05/16/2014 — Date

Dr. Erik Hobbie — Department Chair

ABSTRACT

Micro Electro-Mechanical Systems (MEMS) are currently fabricated using methods originally designed for manufacturing semiconductor devices, using minimum if any assembly at all. The inherited limitations of this approach narrow the materials that can be employed and reduce the design complexity, imposing limitations on MEMS functionality. The proposed Laser-Assisted Advanced Assembly (LA^3) method solves these problems by first fabricating components followed by assembly of a MEMS device. Components are micro-machined using a laser or by photolithography followed by wet/dry etching out of any material available in a thin sheet form. A wide range of materials can be utilized, including biocompatible metals, ceramics, polymers, composites, semiconductors, and materials with special properties such as memory shape alloys, thermoelectric, ferromagnetic, piezoelectric, and more. The approach proposed allows enhancing the structural and mechanical properties of the starting materials through heat treatment, tribological coatings, surface modifications, bio-functionalization, and more, a limited, even unavailable possibility with existing methods. Components are transferred to the substrate for assembly using the thermo-mechanical Selective Laser Assisted Die Transfer (*tm*SLADT) mechanism for microchips assembly, already demonstrated by our team. Therefore, the mechanical and electronic part of the MEMS can be fabricated using the same equipment/method. The viability of the Laser-Assisted Advanced Assembly technique for MEMS is demonstrated by fabricating magnetic switches for embedding in a conductive carbon-fiber metamaterial for use in an Electromagnetic-Responsive Mobile Cyber-Physical System (E-RMCPS), which is expected to improve the wireless communication system efficiency within a battery-powered device.

ACKNOWLEDGEMENTS

First, I would like to thank my adviser, Dr. Val Marinov, for his continuous support in the Ph.D. program. Dr. Marinov is the person responsible for my involvement in the laser-assisted fabrication and manipulation research and the Ph. D. program. He has always been there to listen and give advice, and taught me that there is always more than one way to approach a research problem and that persistence is the key to accomplishing any goal.

Besides my adviser, I would also like to thank the rest of my dissertation committee: Dr. Orven Swenson who was always there to answer my questions related to lasers, Dr. Bejamin Braaten for bringing forward an appropriate application for my research work, and Dr. Fardad Azarmi and Dr. Xinnan Wang for taking interest in my dissertation research and agreeing to be members of my thesis committee.

I am deeply indebted to Matt Semler and Ross Miller for their helpful discussions and for training me on the operation of the laser transfer station.

The technical assistance of the following NDSU personnel is appreciatively recognized: Greg Strommen, Kevin Mattson, Frederik Haring, and Scott Payne.

I give my most special thanks to my family: my wife, Salzitsa, for her continuous encouragement to follow my interests even when those interests crossed the borders of language and geography, and my daughters, Dahlia and Aya, whose patience, serenity, and love enabled me to complete this work.

Last, but not least, I thank my parents, Nina Docheva and Andrey Atanassov, for giving me life in the first place and for the priceless first years of my education, as well as my brother, Alexander Atanasov, for his support.

TABLE OF CONTENTS

ABSTRACT iii

ACKNOWLEDGEMENTS iv

LIST OF TABLES vii

LIST OF FIGURES viii

CHAPTER 1. INTRODUCTION 1

1.1. Overview 3

CHAPTER 2. LITERATURE REVIEW 4

2.1. Metamaterials 4

2.2. What are MEMS and Where Do They Stand Today? 5

2.3. Devices, Systems, and Application Areas of MEMS 8

2.4. MEMS-Based Metamaterials 12

2.5. Non-Laser Based Methods for MEMS Fabrication and Assembly 14

2.6. MEMS Assembly 36

2.7. Laser-Based MEMS Fabrication 39

2.8. Laser-Assisted Assembly for MEMS 50

2.9. Laser-Induced Forward Transfer (LIFT) 60

CHAPTER 3. THERMO-MECHANICAL RELEASE (*tm*SLADT) 71

3.1. Laser Enabled Advanced Packaging (LEAP) for Ultrathin Dies in Flexible Substrates 75

3.2. Wafer and Sample Preparation Steps for LEAP Experiments 82

3.3. Summary 86

CHAPTER 4. LASER-ASSISTED ADVANCED ASSEMBLY (LA^3) FOR MEMS FABRICATION 88

CHAPTER 5. EXPERIMENTAL RESULTS AND DISCUSSION 92

5.1. Thermo-Mechanical Selective Laser-Assisted Transfer of Silicon Components 92

5.2. Thermo-Mechanical Selective Laser-Assisted Transfer of Metal Components 98

5.3. Technology Demonstrator: E-RMCPS (Electromagnetic-Responsive Mobile Cyber-Physical System) 106

5.4. Magnetically Actuated Switches 108

5.5. Laser-Assisted Advanced Assembly (LA^3) of Magnetic Switches 121

5.6. Switch Functionality Testing 137

CHAPTER 6. CONCLUSIONS 144

CHAPTER 7. FUTURE WORK 146

BIBLIOGRAPHY 148

LIST OF TABLES

Table | Page

1. Successfully integrated MEMS devices and their current market [7] 11
2. Types of lasers used in MEMS micromachining [12] 40
3. RIE parameters used for thinning and dicing of Si wafers 83
4. Transfer parameters used in two independent experiments. 100
5. Washer dimensions and transfer rate 105
6. Laser parameters used for receiving substrate micromachining 122
7. Laser parameters used for carrier substrate micromachining 128
8. Switch resistance values for laser assembled micro switches 139
9. Switch resistance for “small” macro switches 141
10. Surface roughness of laser micromachined copper and copper foil 141

LIST OF FIGURES

Figure Page

1. Constituents of MEMS field (adapted from [6]). 6
2. A sample of commercially important MEMS devices; clockwise from top left, ink jet printer head, medical pressure sensor, noise-cancelling microphone, silicon clock, gyroscope, and Digital Light Processor (DLP) (adapted from [7]). 9
3. Refraction in conventional material vs. left-handed material. 13
4. SRR based metamaterial structure (left) and SEM photograph of the same metamaterial after rotating different elements out of the plane by rapid thermal annealing [15]. 14
5. Isotropic (left) vs. anisotropis chemical wet etch (adapted from [20]). 16
6. Isotropic chemical etching undercut profiles without (*left*) and with (*right*) stirring of the solution (adapted from [6]). 16
7. Anisotropic wet etching on a <100> Si wafer (*left*) and <110> Si wafer (*right*) (adapted from [6]). 17
8. Surface micromachining of a cantilever (*left*) and beam structure (*right*). 18
9. Processing difference between (*left*) bulk and (*right*) surface micromachining used to fabricate a simple cantilever structure (adapted from [21]). 20
10. Stiction effects resulting in bridge structure collapse. 21
11. Principal steps in silicon on insulator (SOI) wafer stack fabrication [22]. 22
12. Principles of deep reactive ion etching or "Bosch process" (Adapted from [25]). 26
13. SEM of "conventional" two-step DRIE (*left*) and Plasma-Therm (*right*) patented three-step deep silicon etch (DSE^{TM}) [9]. 27
14. Schematic of LIGA for high aspect ratio MEMS component (adapted from [6]). 29
15. Hot embossing for microfluidic components fabrication (adapted from [6]). 31
16. Vapor (dry) phase etching using HF [27]. 32
17. Schematic of electro-discharge micromachining (adapted from [28]). 33
18. Focused ion beam micromachining material interaction [29]. . 34
19. Schematic of a typical laser micromachining setup. 35

20. Schematic of light-solid interaction for different types of lasers (adapted from [42]). 41

21. Traditional LIGA showing vertical structures (*left*) vs. laser-LIGA (*right*) continuous relief (adapted from [12]). 44

22. Pulsed laser deposition of thin films (adapted from [59]). 46

23. Schematic of UV laser stereolithography. 48

24. Single-level process (*left*) vs. multi-level hybrid fabrication approach (*right*) [47]. 49

25. Self-actuated micro mirror; vibromotors, using comb drives move the front and rear sliders for out of plane rotation of the mirror [73]. 51

26. Hybrid laser-assisted micro assembly of parts for MEMS [12]. 53

27. Welding of transparent with absorbing material using nanosecond-pulse laser [80]. 55

28. Femtosecond lasers joining of transparent materials (adapted from [80]). 56

29. Bond-and-release component joining method [47]. 57

30. Accuracy and precision in micro-manipulation. 58

31. Possible outcomes of a micro assembly process. 59

32. Component placement accuracy; increasing precision and accuracy will allow to increase resolution and to use smaller components (adapted from [82]). 60

33. Measured variation in release velocity vs. laser fluence for 100 µm thick Ni structures by ablative release using a single pulse from a 248 nm KrF laser; solid line is the predicted from equation 1 [77]. 66

34. Measured variation in release velocity vs. laser fluence for 130 µm thick Si structures by ablative release using a single pulse from a Q-switched 1064 nm Nd:YAG laser; solid line is the predicted from equation 1 [83]. 67

35. *tm*SLADT with a two layer configuration blister formation and component release [104]. . 73

36. Laser-transferred 18 to 20µm thick, 250µm square silicon dies transferred using *tm*SLADT and shown on the receiving substrate. 74

37. Process sequence in the Laser Enabled Advanced Packaging [105]. 76

38. An SEM picture of a part of silicon wafer after laser dicing, showing the accumulation of debris around the 20-µm wide streets (*left*); a close-up view of a street ablated using a Nd:YVO4 HIPPO laser (*center*); a close-up view of an RIE-etched street (*right*) [104]. .. 78

39. Chemical structure diagram of the PE7 polymer adhesive material [104]. 80

40. SEM image of 670×670 µm, 50 µm thick laser-cut Si dies on the receiving substrate after transfer. The transfer was initiated by scanning three concentric circles while focused on the DRL as seen in Figure 43. The average power of the laser was 200 mW [104]. ... 86

41. Schematic of Laser-Assisted Advance Assembly (LA^3) process for hybrid assembly. ... 90

42. Main steps in LA^3 for starting material in thin sheet form. ... 91

43. SEM image of laser-singulated die site after transfer (*left*), SEM image of RIE-singulated die site after transfer (*right*) [104]. ... 93

44. SEM images of DRL after scanning with various laser parameters, 150 mW power, 300 mm/s scan speed (*left*). The blister formed in the DRL is largely intact, 200 mW power, 400 mm/s scan speed (*center*). The blister is partially ruptured, 250 mW power; 300 mm/s scan speed (*right*). The blister is completely ruptured. The streaking seen in the SEM images was due to charging of the polyimide, and was not actually present in the layer [104]. ... 95

45. XY scatter plots of transferred 670×670 µm, 50 µm thick Si dice, showing lateral displacements in µm for laser-singulated (*left*) and RIE-singulated (*right*) dies from their release positions. The circle represents the 6σ region, where σ is the standard deviation; the center of the circle represents the mean radial displacement [104]. ... 97

46. Various shapes cut from aluminum foil after transfer to a receiving substrate. ... 99

47. Transferred aluminum squares (670 x 670 µm); image through carrier substrate showing very good precision of transfer (*left*), and image of a receiving substrate with check board patterned transferred dies (*right*). ... 101

48. Transfer of aluminum square tiles (670 x 670 µm) with thermo-mechanical Selective Laser Assisted Die Transfer (*tm*SLADT) mechanism; image through carrier substrate. ... 102

49. Poor precision of transfer of 350 by 350 µm aluminum squares by ablative release mechanism. ... 103

50. Circles and washers of various shapes and designs on a receiving substrate. ... 104

51. Damage to Dynamic Release Layer sustained in machining of very small circle; image through quartz carrier with back-light. ... 105

52. Schematic representation of Electromagnetic-Responsive Mobile Cyber-Physical System E-RMCPS [118]. ... 107

53. MEMS switches in DC field and basic device schematic [118]. ... 108

54. Magnetic switch first prototype; switch parts schematic (*left*) and assembled switch (*right*). ... 111

55. Magnetic particles in a transparent box placed between two magnets; the particles easily bridge the gap of 7 mm between the top and bottom surface. Distance between the magnets is 36 mm, corresponding to a magnetic field strength of 500 Gauss for this set of magnets. 113

56. Switch during resistance test. 114

57. Magnetic field strength vs. distance between the magnets; orange diamonds are values measured, line is the fit. 114

58. Resistance as a function of magnetic field strength for switches with different R-values; note the similar behavior, but different scale on the y-axis. 116

59. Resistance behavior of a sample of large cavity switches (cavity height of 125 μm) as a function of R-value for different magnetic field strength. 117

60. Resistance as a function of magnetic field strength for large (*left*) and small (*right*) switches for two different R-values, 20 (*top*) and 40 (*bottom*). Note the different x- and y-axis scales, but similar behavior. 119

61. Resistance behavior of small cavity switches (cavity height of 125 μm) as a function of R-value for different magnetic field strength. 120

62. Schematic of two-step laser micro-machined cavity design; tipped on its side (*right*). 122

63. Finished cavity cross section obtained with a contact profilometer. 123

64. Contact surface of receiving substrate cavity pre- (*left*) and post- (*right*) plasma cleaning; 20X magnification (*top*) and 100X magnification (*bottom*). 125

65. Top view of a micro-machined cavity partially filled with Ni-coated magnetic particles; the three consecutive rings are marks used for aligning before laser transfer. 125

66. Steps in copper tape preparation for "caps" fabrication. 127

67. Alignment device for laser transfer of components. 129

68. Schematic of substrate alignment. 130

69. Experimental set-up for Laser-Assisted Advanced Assembly [104]. 131

70. Laser beam top hat profile used in *tm*SLADT. The profile is captured before the beam waist where the optical beam exits the scanhead [102]. 132

71. Main steps in magnetic switch fabrication and assembly by Laser-Assisted Advanced Assembly. 133

72. Measuring precision of transfer with OGP Flash 200 system. 135

73. Precision of transfer for laser-assembled switch top contacts; the red square is the position of the center of a perfect transfer, the blue cross-hairs shows the actual position of the center of each cap transferred. The scale for both graphs is in mm. 136

74. Measurement of rotation for transferred top contacts. 137

75. Average resistance values for all 21 switches assembled by Laser-Assisted Advanced Assembly method. Insert is a close-up view. 138

76. Switch with possible very large R-value. 140

77. Surface roughness and contact patch (*inserts*) of laser micro-machined copper (*top*) and copper foil (*bottom*). 143

CHAPTER 1. INTRODUCTION

Micro Electro-Mechanical Systems (MEMS) are presently manufactured using methods originally developed for manufacturing semiconductor devices. Semiconductor devices, such as integrated circuit (IC) chips or dies, do not require assembly during their primary fabrication steps. Assembly comes as a secondary step when these dies need to be integrated into a functional device.

The design and device complexity and functionality of MEMS today are limited due to the domination of silicon based materials and manufacturing approaches used. Because the traditional MEMS fabrication methods are so well established and understood, the advances in MEMS fabrication and assembly today are motivated more by research curiosity rather than being driven by market interest. Other reasons for this stark contrast compared to electronics manufacturing, for example, are the substantial capital investment needed for large scale MEMS fabrication, procedure unification, and the lack of involvement, contribution, and cooperation to research from large scale manufacturers.

Relatively recently some novel methods for device fabrication and assembly have been introduced, many of them based on the application of laser energy. The penetration of lasers in MEMS fabrication technology can be attributed to the unique characteristics offered such as excellent resolution, low thermal load, the ability to create truly 3D structures, and the capacity to micro-machine virtually any material including transparent glass and polymers, to name a few. Some variations of classic approaches that have adapted the assistance of laser energy have already been successfully applied in production, i.e. laser-LIGA and laser assisted chemical etching and deposition. Other innovative laser based systems are still only lab and journal paper examples, but all of them have the potential to disrupt the MEMS manufacturing field.

Even more critical for the advancement of the MEMS technology are the limitations of the methods currently used for MEMS assembly, most of which derived from the methods used in the macro-scale and, in general, lack the capabilities to efficiently and at a high rate handle the ultra-small MEMS components.

The process proposed and demonstrated in the following dissertation is based on the idea of laser propulsion where the energy of a laser is utilized to propel a tiny component over a small air gap for assembly onto substrate and subsequently into a functional device. The Laser-Assisted Advanced Assembly (LA^3) method solves the problems outlined in the preceding paragraphs by first fabricating the components on separate substrates followed by hybrid assembly of a MEMS device. The approach presented allows increasing substantially the number of materials that can be employed and provides the possibility to enhance the structural and mechanical properties of the starting materials through surface and volumetric treatment operations. Components are transferred to the substrate for assembly using the thermo-mechanical Selective Laser Assisted Die Transfer (*tm*SLADT) laser propulsion mechanism, already validated by our team. The unprecedented placement precision and accuracy of *tm*SLADT has already been demonstrated for microchip assembly in a process called Laser Enhanced Advanced Packaging (LEAP). Therefore, the mechanical and electronic part of the MEMS can be fabricated using the same equipment/method.

The viability of the Laser-Assisted Advanced Assembly technique for MEMS is demonstrated by fabrication and assembly of magnetically actuated switches for embedding in a conductive carbon-fiber metamaterial for use in an Electromagnetic-Responsive Mobile Cyber-Physical System (E-RMCPS), an application that is expected to improve the wireless communication system efficiency within a battery-powered device.

1.1. Overview

This dissertation includes seven chapters including this introduction.

Chapter 2 is a literature review that starts with the current state of metamaterial research, MEMS devices and systems overview, and MEMS applications in metamaterials. The current techniques for MEMS fabrication and assembly are examined in detail next, followed by a summary of laser-assisted MEMS fabrication, manipulation, and assembly methods. Relevant existing work on the use of lasers for MEMS fabrication and assembly performed by other research groups is also reviewed and discussed in this chapter. This section includes also a review of the general requirements for precision and accuracy in micro assembly. A process called Laser Induced Forward Transfer (LIFT) which is the foundation on which all laser-assisted assembly techniques are based is discussed in the last part of Chapter 2.

A summary of published detailed studies by our group on laser-assisted transfers of dummy and functional IC components and reliability testing are shown in Chapter 3.

Chapter 4 presents the proposed Laser-Assisted Advanced Assembly (LA^3) method that extends laser-assisted assembly of electronic components to include assembly of micro components for MEMS device fabrication.

The experimental work performed and results obtained based on the proposed idea are described in Chapter 5 along with a technology demonstration of a magnetically actuated MEMS switch for embedding in a metamaterial that is intended to improve wireless communication system efficiency within a battery powered device.

A summary of the most important outcomes of the work performed and results obtained is presented in Chapter 6.

Finally, opportunities for future research and exploration are discussed in Chapter 7.

CHAPTER 2. LITERATURE REVIEW

2.1. Metamaterials

The term metamaterial was coined by DARPA more than 10 years ago, but there is still no solid definition of what a metamaterial is. The prefix “meta” (from Greek), meaning “after” or “beyond” in English, would suggest something that possesses different and even extraordinary properties compared to its building blocks. Most generally, a substance that exhibits macroscopic properties different than what would be expected from its microscopic constituents can be described by the term. However, such a definition is quite broad and may include all kinds of man-made substances, composites for instance. The most easily obtainable description from the free online encyclopedia Wikipedia reads:

> Metamaterials are artificial materials engineered to have properties that may not be found in nature. They are assemblies of multiple individual elements fashioned from conventional microscopic materials such as metals or plastics … arranged in periodic patterns. Metamaterials gain their properties not from their composition, but from their exactingly-designed structures. [1]

Many research organizations characterize metamaterials in the scope of the programs and projects constituting the core of their research. The U.S. Department of Defense (DoD) Defense Advanced Research Projects Agency (DARPA) Technology Trust program defines metamaterials as:

> A new class of ordered nanocomposites that exhibit exceptional properties not readily observed in nature. These properties arise from qualitatively new response functions that are: (1) not observed in the constituent materials and (2) result from the inclusion of artificially fabricated, extrinsic, low dimensional inhomogeneities. [2]

The European Union Metamorphose Network of Excellence describes metamaterials as:

> Artificial electromagnetic (multi-) functional materials engineered to satisfy the prescribed requirements ... Superior properties as compared to what can be found in nature are often underlying in the spelling of metamaterial. These new properties emerge due to specific interactions with electromagnetic fields or due to external electrical control. [3]

Some authors like V. M. Shalaev [4] and J. Valentine [5], try to sum up the meaning of metamaterial using fewer words such as "Metamaterials are typically man-made and have properties that are not found in nature" and "Metamaterials are artificially engineered structures that have properties not attainable with naturally occurring materials", respectively.

Based on all of the above definitions it can be summarized that metamaterials need to share the following traits:

- engineered materials
- properties that are more than the sum of their constituent components
- not observed in nature

For the purposes of this document the features of a metamaterial will be summed up yet one more time as follow: *a man-made composite material whose macroscopic response to an external excitation is not readily encountered in nature and not suggested by its microstructure and/or constituent materials.* This general definition is valid at least from the perspective of the several areas of science and engineering that concern this paper: mechanical, electrical, manufacturing, composite and material science [5].

2.2. What are MEMS and Where Do They Stand Today?

MEMS or Micro Electro-Mechanical Systems are most generally defined as miniature mechanical and electro-mechanical structures and devices that are made using various microfabrication technologies. The dimension range for MEMS is quite broad and varies from a few micrometers to several millimeters depending on the complexity and functionality of the device. Equally, the assortment of devices range from simple non-moving structures to complex electro-mechanical systems with many moving elements and integrated electronic components. Complexity aside, the main condition for a structure or a device to be considered MEMS is to

have some degree of mechanical functionality. A very large number of structures, sensors, actuators, and microelectronic devices have been demonstrated over the years and they all fall within one of four MEMS categories [6]. It should be noted here that many of these micro machined devices have shown performance characteristics exceeding those of their macro machined counterparts (Figure 1).

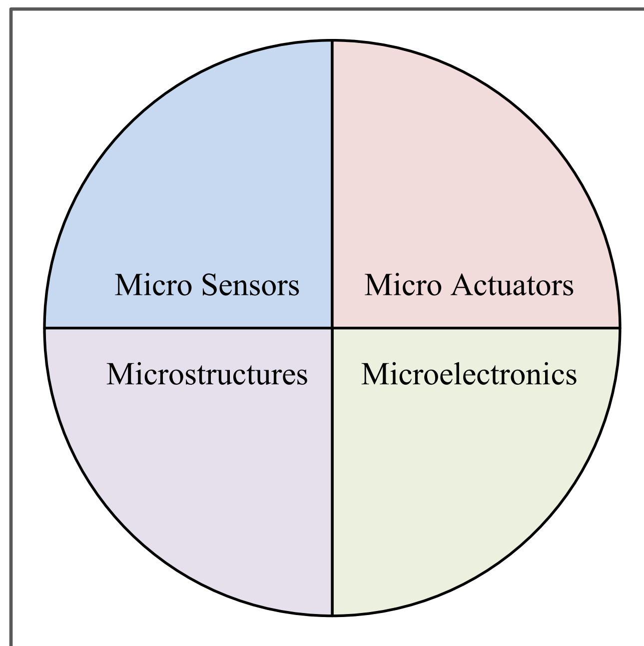

Figure 1. Constituents of MEMS field (adapted from [6]).

Of all the components comprising the field of MEMS the ones that have received the most attention are probably the micro sensors and micro actuators, which are used to convert energy from one form to another. Such transducers have been demonstrated for almost all possible sensing modes including, but not limited to, temperature, pressure, inertial force, chemical sensing, light modulation, magnetic fields, and radiation. Micro actuators have also demonstrated the capability to cause effects at the macro scale level by performing mechanical

deeds far bigger than their miniscule size would suggest. In one notable example, micro actuators placed on the leading edge of aircraft airfoils were used to steer an aircraft using only these miniaturized devices [6].

Historically, MEMS technology has been developing a few years behind, but parallel to, semiconductor based electronics. The foundation of MEMS development was the 1954 discovery of the piezoelectric effect in silicon, which made it possible to measure the strain in silicon based micromechanical structures. That was succeeded by progress in high-gain, low noise amplification, leading to the development of capacitance based sensors and actuators. Today there is an abundance of MEMS devices based on these two effects including pressure and flow sensors, radio frequency (RF) switches, digital light projectors (DLP), microphones, accelerometers, gyroscopes, oscillators, and more. Many new devices are still in the lab and research stage of development and are expected to contribute to the significant growth and penetration of MEMS [6, 7].

Currently, MEMS are in use in virtually every aspect of life, from consumer products and healthcare, through construction, oil and other industrial activities, to military and space applications. Unlike the semiconductor market, which has reportedly grown to around $300 billion by 2011, the market penetration of MEMS has been estimated only at roughly $11 billion in the same year [8]. However, even the most pessimistic growth projections predict the MEMS market to double by 2016 and to eventually surpass the semiconductor $300 billion mark. There are several models and proposals that forecast market growth for MEMS to be much faster and to result in $1 trillion in the foreseeable future, as early as 2023. Based on these best prognoses, a predicted byproduct of such accelerated growth will be about two million direct jobs and roughly four million indirect jobs added in the US alone [8]. For that to happen, however, substantial

work needs to be dedicated to how MEMS are designed, assembled, and packaged, and this work will require new levels of cooperation between tool makers and software developers (for reducing R&D cost and cycles) as well as between competing companies (cooptation) since the funding required for such an endeavor far exceeds the capabilities of any single company [6, 8, 9].

Presently, the development of a typical MEMS product consists of multiple and unique "ones", one product, one process, one package, one application specific integrated circuit (ASIC), one test system. Materials base is often updated solely on experimental results for a particular application. This creates an unpredictable sequence which in some instances leads to several years lead time from idea to production cycle. In order to reduce cycle time and cost and to increase profit margins standardization of all aspects in MEMS manufacturing, design, fabrication, assembly, and packaging, will have to be achieved. Several manufacturers (e.g. ST Thelma) have already demonstrated in-house MEMS process standards for a narrow class of devices. A few standard MEMS processes (Sandia's Summit V) have also been presented and validated for a vast number of designs, but are considered incapable of supporting commercial scale business as they were developed without cooperation with MEMS manufacturers. However, these first steps prove that cohesive standards for MEMS are possible [10, 11].

2.3. Devices, Systems, and Application Areas of MEMS

For decades MEMS development and research have been driven by the advances in lithography and etching processes. Over the last 40 years, semiconductor manufacturing has shown its capability of producing smaller and smaller structures which currently fall in the sub-micron range. This success, however, cannot be credited just to miniaturization. The capacity of batch fabrication of micromechanical systems of remarkable complexity that are preassembled

on a single substrate is an impressive capability of the core manufacturing techniques used in MEMS for years, namely bulk and surface micromachining. Integration of electronics and mechanical devices on one substrate has improved performance and reliability, while batch manufacturing methods have reduced device production cost[10, 12].

Technology push still dominates market pull in the field of MEMS. There are, nonetheless, success stories of commercialized products in cases where a single manufacturing technique fits a suitable application, most prominent examples being ink-jet printer heads, silicon pressure sensors, noise-cancelling microphones, silicon clocks, micro gyroscopes, and more (Figure 2).

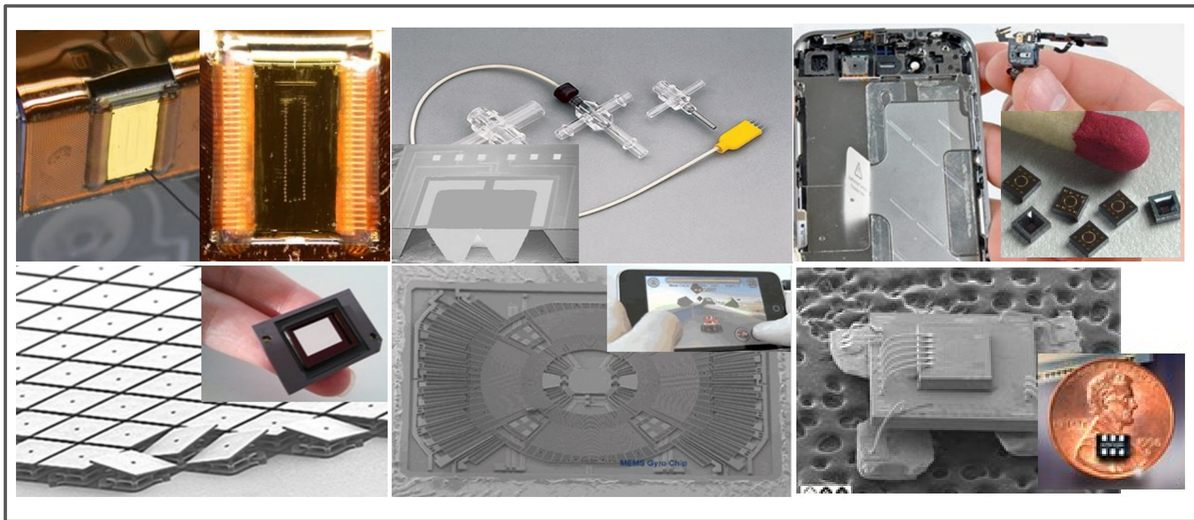

Figure 2. A sample of commercially important MEMS devices; clockwise from top left, ink jet printer head, medical pressure sensor, noise-cancelling microphone, silicon clock, gyroscope, and Digital Light Processor (DLP) (adapted from [7]).

It is expected that the list of successful commercial products will grow rapidly in the coming years as more non-silicon based MEMS production techniques and especially assembly methods leave the research laboratories and reach the manufacturing floor. The list of devices

and systems that are expected to benefit from such developments consists of, but is not limited to [12]:

- pressure and flow sensors and actuators
- linear actuators
- accelerometers and gyroscopes
- chemical and biological sensors, and micro-chemical analysis systems (µTAS)
- micro relays and switches
- micro motors and turbines
- fluid pumps and valves, micro nozzles, and fluid handling systems
- scanning and probing devices
- micro-optics devices and photonics systems

This broad but not complete list of devices and systems encompasses a number of market areas that are no less impressive, including the following: automotive, aerospace, and defense industries; information technology and telecommunications; biotechnology, pharmaceutical, and healthcare industries; measurement and microscopy; the oil industry; automation and process technology; environmental technology; and more [11]. Some of the most important by market share MEMS devices and the advantages they bring to their application areas are listed in Table 1 on next page.

Table 1. Successfully integrated MEMS devices and their current market [7]

Product	MEMS Device	How it works?	Advantages	Market
Ink Jet Printers	Printer head	Uses heat or force to dispense tiny ink droplets	Increased speed and resolution, low cost	Over $2 Billion
Digital Light Processor	Micrometers sized mirrors	Millions of electrostatically tilted mirrors deflect light to form projection image	Arrays of small mirrors are batch produced and offer rapid movement	$1 Billion
Smart Phones, Tablets, etc.	Gyroscope	Uses vibrating structures	Small size, low power, cost	Over $1 Billion
Crash Airbags	Accelerometer	Inertial force acting on mechanical elements	High reliability, fast response, low cost	$1 Billion
Portable Lab on Chip	Microfluidic chip	Detects biochemical products using an automated chip	Low amount of fluid, fast real-time DNA diagnosis for environment monitoring	$1 billion
Automotive Pressure Sensors	Pressure sensor	Pressure causes membrane deformation	High sensitivity, low cost, repeatable performance	$1 billion
Cell Phones and more	Noise cancelling microphone	Acoustic pressure waves deform a micro-machined membrane	Small size, reliability	$1 billion
Cell Phones and more	Silicon clock resonator	A vibrating beam of silicon determines vibration frequency	Low cost	$1 billion
Radar, Cell Phones	Tunable capacitors, low loss inductors	MEMS components used as filters, tunable capacitors and inductors, switches , and antennas	High tenability, improved quality factor, low cost$1 billion	$1 billion
Medical Pressure Sensors	Pressure sensor	Micro-machined diaphragm deforms under applied pressure	Same as automotive plus integrated functionality and disposable	$1 billion

2.4. MEMS-Based Metamaterials

Engineered electromagnetic materials (EMM) that display electromagnetic responses not found in nature such as negative index of refraction, superlensing, dynamic filtering, and cloaking, recently have received considerable attention in the scientific and engineering societies [13, 14]. In such metamaterial composites, often referred to as left-handed materials (LHM), the permittivity (ε) and the permeability (μ) simultaneously have negative values and the electromagnetic response arises from the oscillation of electrons in highly conductive metals like copper and gold [14].

The notion of a left-handed material was first proposed by the Russian physicist Victor Veselago in 1967 whose work was translated in English in 1968 [26]. Veselago theorized that a negative refraction index material can exist if both the permittivity and the permeability of said material are negative and predicted that it will possess unique electromagnetic properties such as reversal of Snell's Law and the Doppler Effect [25, 26]. Veselago was able to prove that in a negative refractive index material the electric and magnetic field together with the wave vector describing the electromagnetic wave form a "left-hand rule" triangle, hence in LHMs the electromagnetic waves group and phase velocity are not matching. As a result, energy still travels away from the source, but the wavefront travels in the opposite direction toward the source (Figure 3).

The experimental verification of Veselago's theory came decades later, first shown by a research group at the University of California, San Diego (UCSD) and later repeated and confirmed by a group at Massachusetts Institute of Technology (MIT). Both groups used split-ring resonators to provide negative permeability and permittivity [15, 16]. That work was followed by characteristic studies and applications research by other groups, but due to the high

loss and narrow bandwidth of split-ring resonators, implementation was limited until it was realized that a transmission line approach to studying LHM is possible.

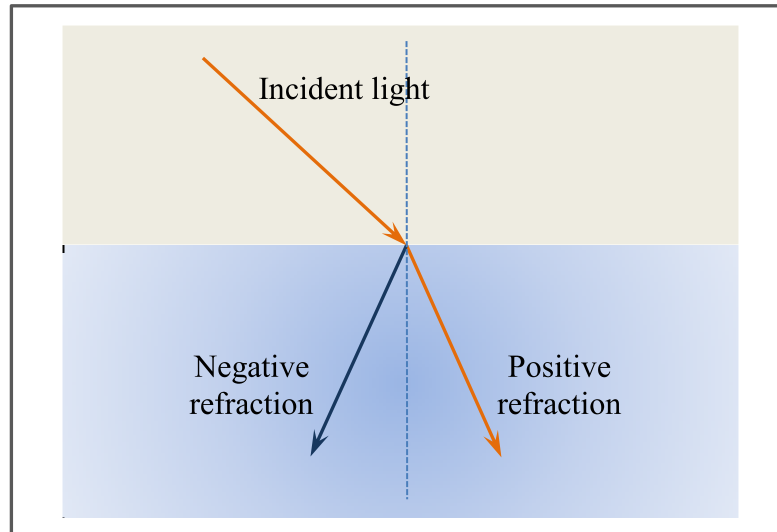

Figure 3. Refraction in conventional material vs. left-handed material.

Still, despite the exciting prospects that LH metamaterials offer, practical applications are limited due to significant loss and small bandwidth, problematic integration, and large size [13]. One possible solution to the above disadvantages is the use of MEMS in metamaterials, because they offer small size and established integration in IC fabrication. Some of the applications of MEMS based LHM that have been shown to date include integrated metamaterials based on split ring resonators (SRR) with variable resonance at RF frequency range, reconfigurable antennas, reconfigurable RF filters, materials with tunable electric and magnetic responses at terahertz frequencies (Figure 4), antenna size reduction and performance optimization, and more [14, 17-19].

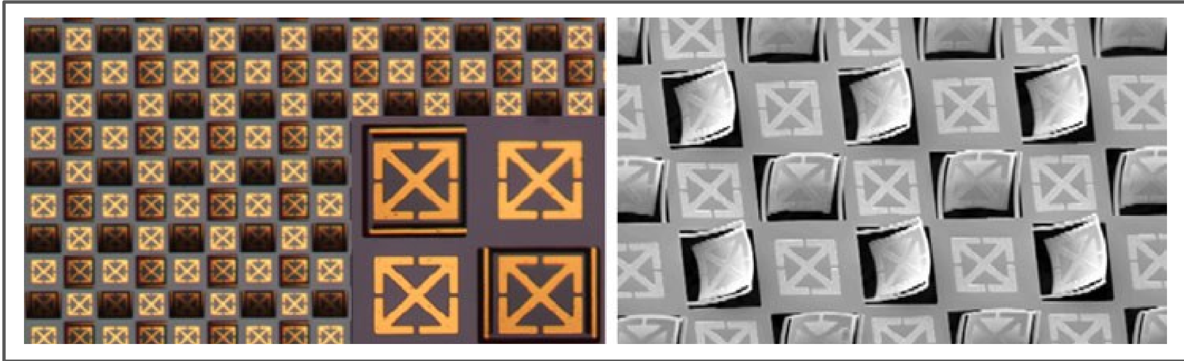

Figure 4. SRR based metamaterial structure (left) and SEM photograph of the same metamaterial after rotating different elements out of the plane by rapid thermal annealing [15].

2.5. Non-Laser Based Methods for MEMS Fabrication and Assembly

Today MEMS are produced mostly by the same batch production methods used for fabricating integrated circuits (IC) which helps to lower per-device production costs. Using these established processes also brings other benefits such as respectable reliability. The electronics part uses the “conventional” process sequences for IC fabrication, e.g. Bipolar, CMOS, and BICMOS, while the micromechanical parts are produced by comparable micro machining techniques that etch away selectively, and add new structural layers comprised of silicon, silicon oxide, silicon nitride, different metals and in some cases polyimides. In addition to microelectronics, more recently MEMS fabrication techniques have been combined with other technologies such as nanotechnology and photonics in order to expand the MEMS scope in the consumer market prospects [6]. All these efforts for integration, however, have been aimed at adding and modifying existing fabrication and manufacturing techniques to serve new purposes in MEMS production. Very little effort, if any, has been put into developing dedicated MEMS assembly processes. Consequently, today’s state-of-the-art MEMS technology has remained modest, usually involving “a single discrete microsensor, a single discrete microactuator, a single

microsensor integrated with electronics, a multiplicity of essentially identical microsensors integrated with electronics, a single microactuator integrated with electronics, or a multiplicity of essentially identical microactuators integrated with electronics [6].” Therefore, even as MEMS design and fabrication approaches have advanced, the promise of a vast design freedom where many types of micro sensors and micro actuators can be combined with microelectronics, photonics, and nanotechnology onto a single substrate, has eluded scientists and developers.

2.5.1. Traditional fabrication technologies

As mentioned earlier, MEMS are manufactured by techniques used in the IC industry, such as oxidation, diffusion, sputtering, CVD, PVD, ion implantation, etc., in addition to more specialized micromachining processes. All these combine to create an exhilarating struggle of tailored design and processing technologies and diverse capabilities for producing one device or one system at a time.

Generally creating a functional MEMS device on a substrate requires etching of thin films deposited beforehand and/or the substrate itself by employing one of two common techniques, wet or dry etching. The first one uses a liquid chemical solution that dissolves the required film or substrate, while the second takes advantage of film/substrate bombardment with reactive ions or vapor phase etchants [6]. Both applications will be presented in more detail in the sections that follow.

2.5.1.1. Bulk micromachining. Bulk micromachining is the oldest technology used in MEMS fabrication and it involves the selective removal of the Si substrate material by chemical or physical means, the former being far more commonly used.

Chemical etching, also known as wet etching, uses a solution of reactive chemical to remove exposed regions of a Si substrate. Chemical etching delivers high etch rates and allows

etching of materials selectively by altering the chemical composition and/or temperature of the solution, adjusting the dopants concentration in different substrate regions, and exposing certain crystallographic planes to the solution [6, 20].

Wet etching can be divided into two distinct types; isotropic and anisotropic (Figure 5). In both cases a mask is used to protect the regions that are not to be affected by the process.

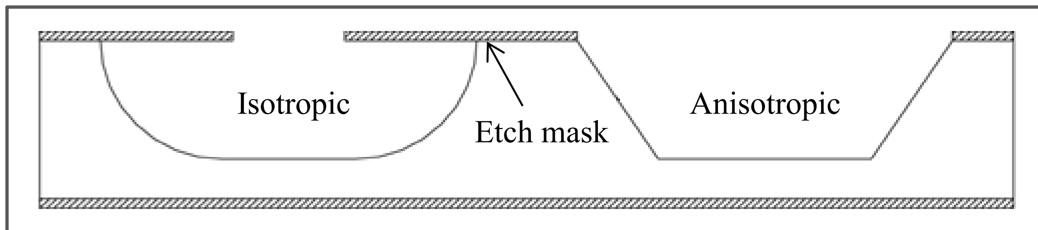

Figure 5. Isotropic (left) vs. anisotropis chemical wet etch (adapted from [20]).

In the former kind, the etch rate is independent of the crystallographic planes orientation of the substrate and the etch rate is in theory the same in all directions, which leads to what is referred to as undercut in the regions covered by the mask material. Undercut can be reduced by stirring of the chemical bath (Figure 6) and consequently wet etching is almost always executed under strong stirring. The most commonly used mask material in isotropic etching is silicon nitride due to its slower etch rate in wet etch solutions than silicon oxide [6].

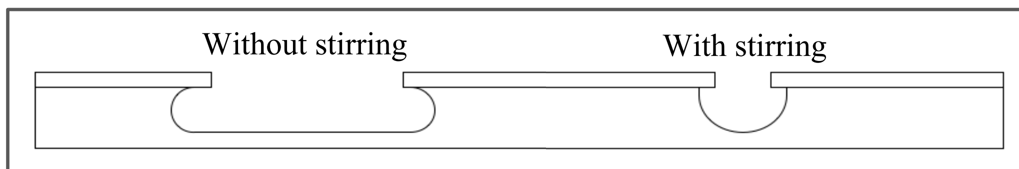

Figure 6. Isotropic chemical etching undercut profiles without (*left*) and with (*right*) stirring of the solution (adapted from [6]).

Anisotropic wet etching processing is similar to isotropic, but the etch rate in this case depends on the crystallographic orientation of the substrate. Generally, Si etches slower in the <111> plane than in any other plane and the etch rate ratio can be as high as 1000:1 [20]. As a result, anisotropic wet etch can provide very high resolution capability and dimensional control, as well as variety of shapes, making it much more extensively used in bulk micromachining for MEMS [6].

The type of mask used in anisotropic etching depends on the chemical solution used. In general, silicon nitride (Si_3N_4) and thick silicon oxide (SiO_2) films are used with potassium hydroxide (KOH), and metal masks are used with ethylene diamine pyrocatechol (EDP) and tetramethylammonium hydroxide (TMAH). Etch selectivity and rates are strongly dependent upon processing conditions such as temperature, chemical composition, stirring, etc. Etch stops such as heavily boron-doped silicon are often used when thickness uniformity and etch depth need to be controlled precisely as in the case of thin membrane fabrication (Figure 7) [6, 20].

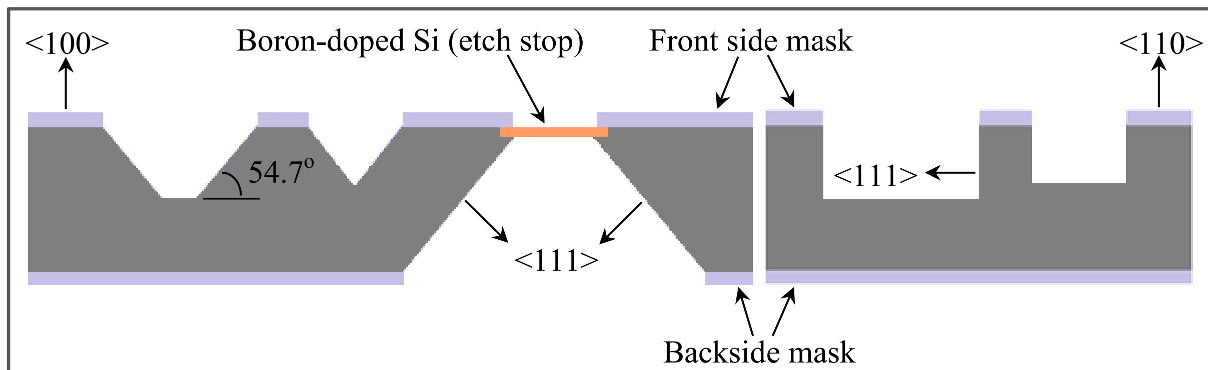

Figure 7. Anisotropic wet etching on a <100> Si wafer (*left*) and <110> Si wafer (*right*) (adapted from [6]).

2.5.1.2. Surface micromachining. Surface micromachining is another traditional and widely used technology in MEMS fabrication. Surface micromachining can use a wider

combination of structural, sacrificial, and etchant material combinations, hence providing a large number of processing variations. Generally, this process relies on the deposition, masking, and removal of numerous layers of material to create the MEMS device. In the most basic form (Figure 8), a sacrificial layer (SiO_2) is first deposited onto the substrate wafer (step not shown), patterned with photoresist (step not shown) , and etched using hydrofluoric acid (HF) to create the anchors openings for the structural layer, which is in turn deposited, patterned, and etched or lifted-off. In the last step of the sequence, the sacrificial layer is removed to create the desired structure and to allow its movement [6, 20].

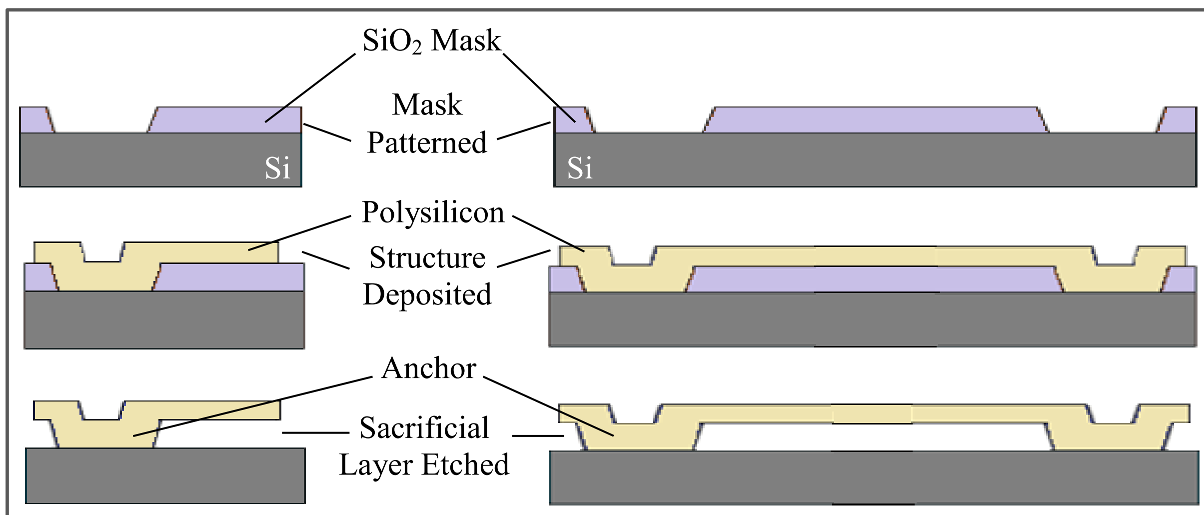

Figure 8. Surface micromachining of a cantilever (*left*) and beam structure (*right*).

Surface micromachining provides several advantages over bulk micromachining which makes it very popular in MEMS production. First, very tight control of the thickness of the subsequent layers is possible. Established techniques such as chemical vapor deposition (CVD), physical vapor deposition (PVD), and atomic layer deposition (ADL) allow fine tuning of the layer thickness to the number of atomic layers placed, therefore providing very precise

dimensions in the vertical direction. Next, horizontal precision and accuracy depends on a photolithographic process which at present allows resolution in the submicron range. Third, the variety of material and etchant chemistry combinations makes surface micromachining compatible with microelectronic fabrication, thus enabling integrated MEMS devices. Finally, surface micromachining is done on one side of the wafer allowing higher device density and subsequently lower per device cost than bulk micromachining [6, 20].

On the most basic level, the key difference between bulk and surface micromachining is in the sacrificial layer employed; in the former case, the silicon wafer is used both as a sacrificial and structural layer, while in the latter, the sacrificial layer is deposited or thermally grown (as in the case of silicon oxide) and the silicon wafer acts only as a structural layer. Generally, for the same device structure, surface micromachining requires less processing steps than bulk micromachining. As shown in Figure 9, for the same simple cantilever structure the process can start with a silicon wafer covered with silicon oxide on one side. In the case of bulk micromachining, the first step involves the deposition of the device layer. The device layer and oxide layer (which is used as a backside mask in this case) are etched in steps two and three, respectively, using different chemistries. In the last step, a portion of the silicon wafer is etched away in yet another chemical to release the cantilever beam. In contrast, the first step in surface micromachining is to pattern the sacrificial oxide layer. The device layer is deposited and patterned by a lift-off process in step two and finally the oxide is etched away to release the structure. All the subtle variances discussed so far make surface micromachining a more flexible process from a design and manufacturing standpoint and results in lower per-device final cost [21].

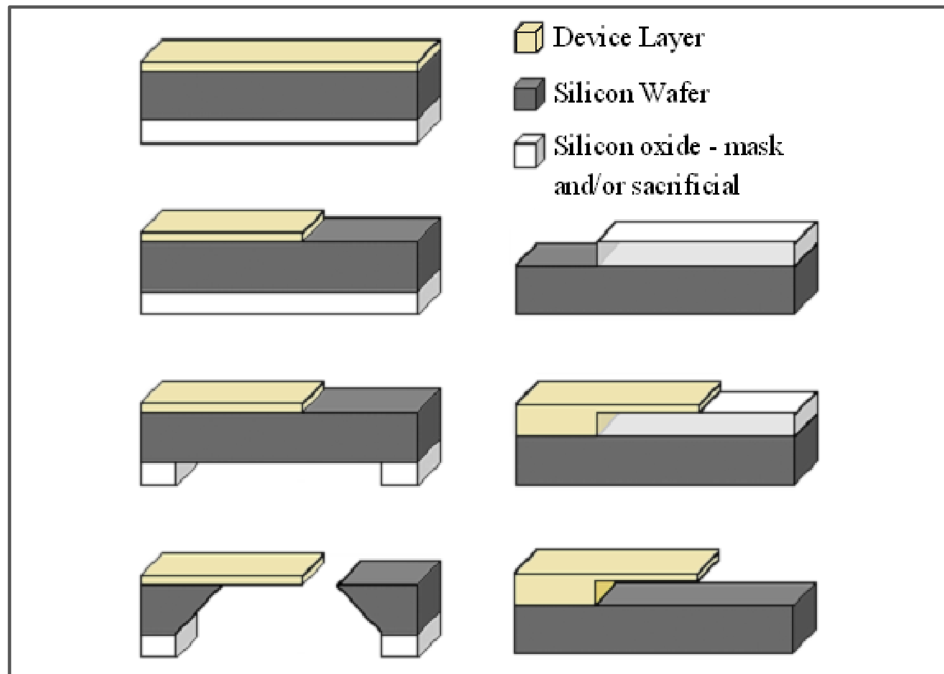

Figure 9. Processing difference between (*left*) bulk and (*right*) surface micromachining used to fabricate a simple cantilever structure (adapted from [21]).

Surface micromachining has several disadvantages as well. Since the structural layers in this technique are deposited rather than created from bulk material, their mechanical properties are usually unknown and vary between depositions even in subsequent runs. Hence these properties need to be measured and sometimes are hard to control and reproduce. In addition, deposited films tend to have high residual stresses, which necessitate annealing at high temperatures to be lessened and make the process incompatible with many microelectronic structures that are typically affected by high temperature treatments. Lastly, the release of the structural layers is difficult due to stiction effects caused by capillary forces, which may cause the structures to collapse (Figure 10). Stiction may also happen during the service life of the device in which case the use of anti-stiction coatings is needed [6, 20].

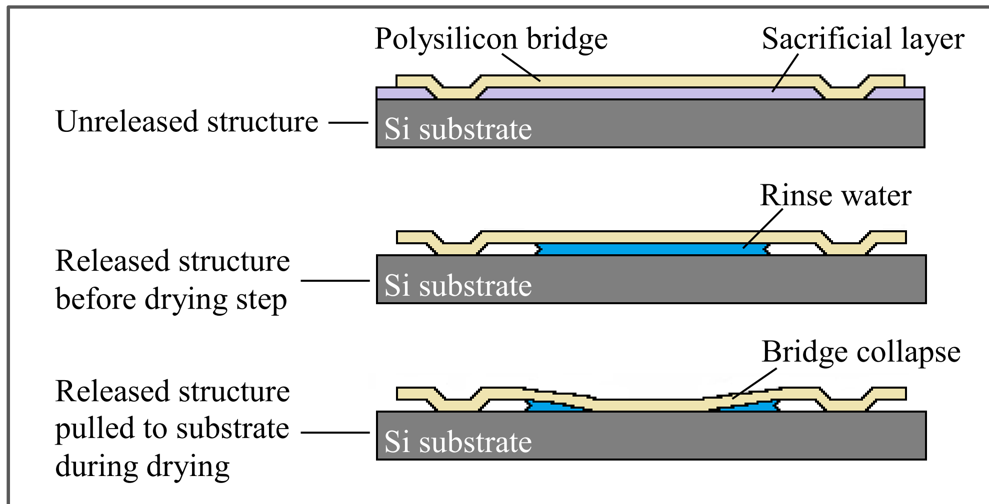

Figure 10. Stiction effects resulting in bridge structure collapse.

A popular surface micromachining process and material system is a phosphosilicate glass (PSG) sacrificial layer with a doped polysilicon structural layer. Hydrofluoric acid is used as an etchant of the PSG sacrificial layer in order to release the device. This is a commonly used type of surface micromachining for fabrication of Analog Devices' integrated MEMS accelerometer used to activate crash airbag systems [6].

A more recent variation of surface micromachining that uses polyimide as a sacrificial layer and oxygen plasma as an etchant avoids some of the disadvantages present. In this case the deposition temperatures of the sacrificial and structural layers are low enough to allow integration of the MEMS device with microelectronic devices fabricated previously in the underlying silicon wafer. The use of a dry release process, i.e. reactive ion etching (RIE) also alleviates stiction problems. An analogous method is used to make the device used in Texas Instruments Digital Light Processor (DLP) projection systems. One disadvantage of this process is the limited area under a structure that the plasma can penetrate and release, which puts design and size constraints on the device [6].

2.5.1.3. Wafer bonding. Wafer bonding in micromachining is the assembly of two or more wafers to produce a permanent multilayer stack. This procedure is analogous to welding in the macro scale processes. Wafer bonding is extensively used in MEMS packaging and is very valuable in applications that require devices with considerable mass or when the mechanical properties of single-crystal silicon are beneficial over deposited silicon. An extremely important application of this process is in making silicon on insulator (SOI) wafers (Figure 11) that are becoming increasingly popular and are used in various applications from today's quad, six, and eight core processors to silicon photonics for fabricating optical waveguides and other passive optical devices for integrated optics [22, 23].

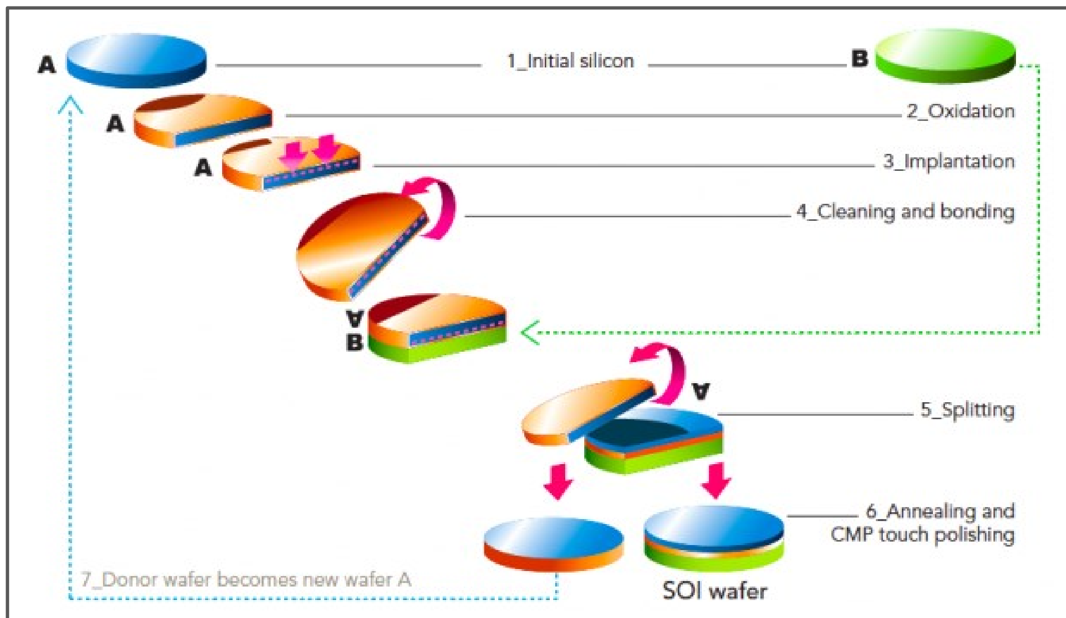

Figure 11. Principal steps in silicon on insulator (SOI) wafer stack fabrication [22].

There are three variations of wafer bonding: direct bonding, also referred to as fusion bonding; anodic or field-assisted bonding; and bonding with an intermediate layer. Fusion

bonding is usually used to attach two silicon wafers together, one of which may have a layer of silicon oxide or silicon nitride on it. That is the method used in SOI fabrication, but it requires temperatures in the order of 1000°C [6].

Anodic bonding uses elevated temperature (around 450°C) and voltage in the order of 1000V to bond silicon or metals (Al, Cu, Ni, and more) and alloys (Kovar, Invar) to a glass wafer (Pyrex 7740) [6]. Pyrex 7740 has a coefficient of thermal expansion (CTE) almost equal to that of silicon so there are almost no residual stresses in the layered structure. Anodic bonding relies on the high concentration of Na+ ions in Pyrex 7740, which at high temperature easily migrate away from the glass surface creating a negative charge at the interface. The positive voltage applied to the silicon in addition to the high temperature fuses the wafers together. It is imperative that anodic bonding is performed in extremely clean environments, and, just as in direct bonding, requires extremely flat, smooth, and clean contact surfaces [6].

Bonding of wafers with an intermediate layer may use a number of different materials for the intermediary layer. One variation is called eutectic bonding and uses gold deposited on one of the wafers as a bonding layer. The process requires the lowest temperature of all wafer bonding techniques, around 363°C, but even at such low temperatures the diffusion of gold into silicon is exceptionally rapid, hence it is the preferred joining method for temperature sensitive MEMS devices. Other intermediate layers that can be used include different polymers (e.g. epoxy resins, polyimides, silicones, and photoresists) that are typically used to attach very thin, thus fragile, device wafers to temporary handle wafers used to ease processing [6].

2.5.1.4. Limitations of Si and traditional photolithography based fabrication. As mentioned earlier, for years and even decades, MEMS research and development has been dominated by silicon. Silicon is an attractive material for MEMS mainly due to its abundance

and relatively low cost for the high quality it provides, the well understood and established manufacturing methods, and the possibility for monolithic integration of structures and electronics [12]. While silicon and silicon micromachining processes have demonstrated their ability to create an enormous number of practical MEMS devices, they do have a number of limitations. First is the obvious limited range of materials employed, i.e. silicon, silicon oxide and nitride, and a few metals. Expanding the MEMS material base is seen as one of the main drivers behind the LIGA process development [12]. Next is the limitation of the number of 3D structures that can be obtained by traditional methods such as bulk micromachining, where the geometries achievable are limited by the crystal structure orientation of the substrate. These limitations drove the development of deep reactive ion etching (DRIE) and silicon on insulator technologies that can produce vertical walls of several hundred micrometers and significantly improve the design and fabrication complexity. Nevertheless, arbitrary 3D structures are still not possible even with those methods.

Although silicon dominance in MEMS is not likely to lessen much in the near future, there are many indications that new fabrication and assembly techniques are needed in order to expand the range of materials and material treatments that can be used and consequently increase the complexity, functionality, reliability, and performance of the device and systems that can be built. Some of the more recent MEMS fabrication techniques that have broadened the range of possible materials and increased the structures that can be obtained are discussed next.

2.5.2. High-aspect ratio fabrication technologies

The previous sections have covered wet etching techniques for structure fabrication and their limitations. Although generally considered cheaper than dry etching, wet etching fails when

high resolution or nearly vertical wall features with no or minimal substrate undercut are required.

2.5.2.1. Deep reactive ion etching. Reactive ion etching, or simply RIE, involves both a chemical and a physical process. For the chemical part it uses reactive gasses and a RF power source to break the gas molecules into plasma ions. These ions are accelerated toward the specimen being machined where they react with the surface of the substrate and create different gaseous products. The physical part of the process is similar to sputtering deposition where high energy ions bombard the substrate, but instead of using a material target for depositing new layers, the ions remove atoms from the sample and etch it away. The chemical part of the process is isotropic, while the physical part is highly anisotropic, and by balancing the two parts rounded or nearly vertical features can be micro-machined. Designing an RIE process is a difficult task because it involves many physical and chemical parameters that can be adjusted in order to obtain the results required [6, 20].

Reactive ion etching has several variations, each of which finds application in MEMS fabrication. If the reactive ions are eliminated from the equation, a purely physical etching process referred to as sputter etching remains. Eliminating the high energy ions, but still using chemicals in gaseous form gives vapor phase etching, which will be covered in a little more detail later. The third subclass of RIE called deep reactive ion etching or DRIE is a relatively new fabrication technique that has surged in popularity as it is capable of producing hundreds of microns deep, nearly vertical structural features in Si with very high aspect ratios; aspect ratios of up to 100:1 have been reported in the literature [24, 25].

DRIE is also known as the “Bosch process” after the name of the German company Bosch that owns the original patent. DRIE of silicon is illustrated schematically in Figure 12. In

this process two different gasses are exchanged in the reactor in very short time intervals. The first gas, SF_6, is used to etch the silicon substrate while the second one, C_4F_8, creates passivation on the surface by depositing polymer on the walls and bottom of the feature already etched. In the next step, SF_6 is again introduced in the chamber and the polymer deposited on the bottom of the feature is etched almost instantaneously by the anisotropic, physical part of the process, the ion bombardment. The polymer deposited on the wall, in contrast, is etched away very slowly by the isotropic chemical part of the process. The steps are repeated until the desired depth is achieved with etch rates that can be as high as 4 µm/minute for some commercial systems. As seen in Figures 12 and 13, there is a characteristic wavy profile left by DRIE, but it can be controlled and minimized by more frequent switching between the gas chemistries, and this process can etch through a whole silicon wafer thickness three to four times faster than wet etching while still keeping the vertical side wall profile [6, 24, 25].

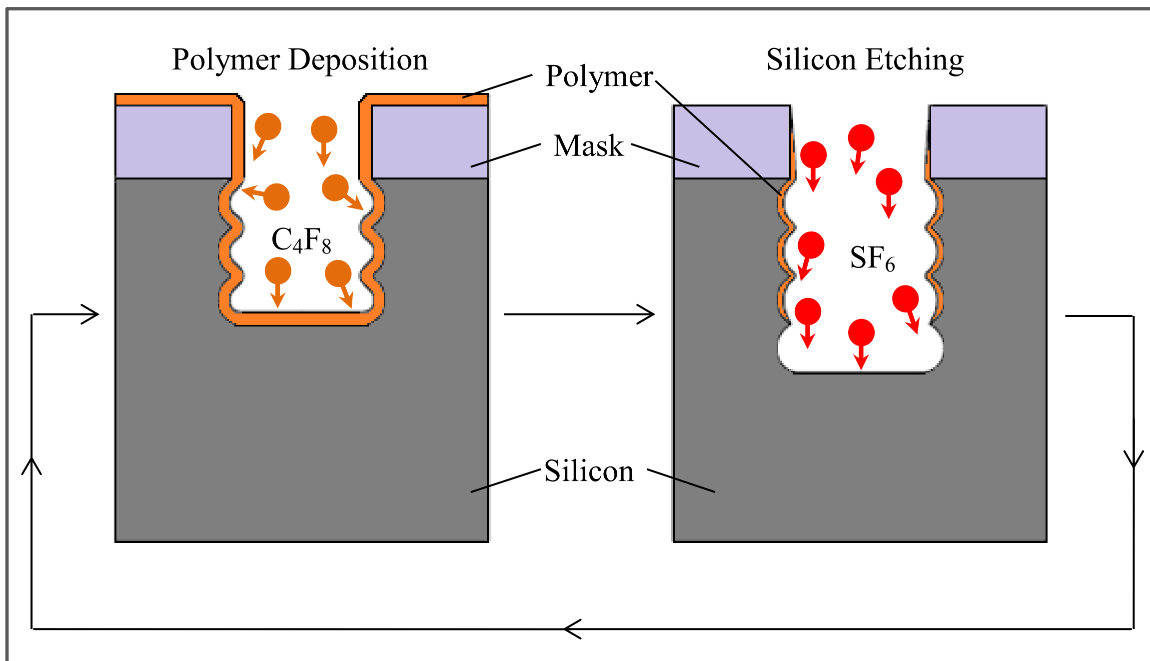

Figure 12. Principles of deep reactive ion etching or “Bosch process” (Adapted from [25]).

Recently, in 2012, Plasma-Therm announced a variation of their RIE process that uses a unique three-step procedure that allows optimization of the passivation removal in the isotropic etch step. Their system also utilizes ultrafast gas switching (sub-second range) which reduces the scalloped edge effects and loading effects (Figure 13), eliminates undercutting at etch stops, and further increases the etch rate [9].

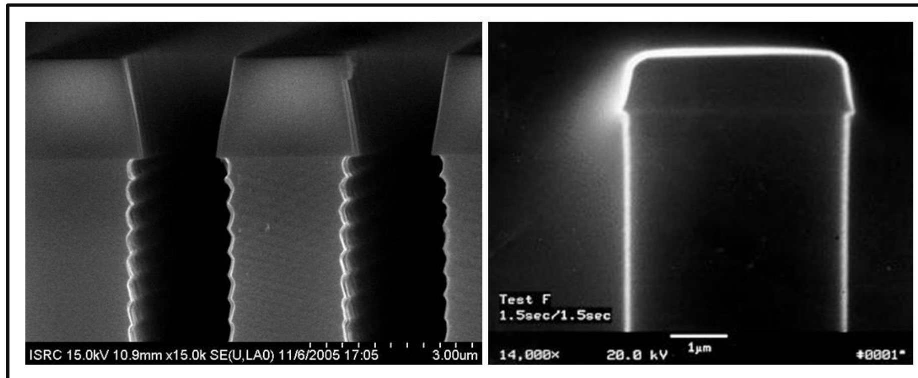

Figure 13. SEM of "conventional" two-step DRIE (*left*) and Plasma-Therm (*right*) patented three-step deep silicon etch (DSE^{TM}) [9].

In addition to silicon and its oxides and nitrides, reactive ion etching can be used to micro-machine metals such as aluminum, gold, and refractory metals and non-metallic materials such as gallium arsenide, quartz, polyimides, and other materials by using fluorine and chlorine based chemistries, oxygen, helium, and mixtures of these gasses. Like wet etching, reactive ion etching needs to use a mask to protect the parts of the substrate that need to remain intact. Depending on the gas chemistries used in the process, the mask can be a photoresist, an oxide, or a metal one, but in any case the process needs to be designed with high mask to substrate selectivity in mind so the feature may be created before the mask is "depleted". Yet another challenge in RIE is the fact that the etch rate is dependent on the amount of material exposed to

etching agents, so loading effects need to be taken into consideration when designing the process and the etch must be monitored frequently as the process progresses in order to obtain the results desired [9, 24, 25].

2.5.2.2. LIGA. LIGA is the first predominantly non-silicon technology for making very high aspect ratio components that is now popular in MEMS fabrication. LIGA, which was introduced in the early 1990s, was originally developed in Germany for the production of nozzles for uranium enrichment and the name is an abbreviation for "Lithographie, Galvanoformung, Abformung" or Lithography, Electroplating, Molding. The concept of LIGA is to produce a polymer structure using lithography that can be used as is or as a casting to obtain a mirror image component by electroplating in order to make a tool for embossing or injection molding. The idea behind this concept is that economical mass reproduction of the original structure will be possible with a range of materials including plastics, metals, and even ceramics [12].

The original LIGA uses a synchrotron light source with an extremely short wavelength, in the range of 0.1 to 0.01 nm. The process starts with the exposure of x-ray sensitive PMMA through a special mask, followed by development, to first make the mold for the component that will be made (Figure 14). Due to the high sensitivity and penetration depth of x-ray radiation in PMMA, the mold has extremely smooth and vertical sidewalls and allows production of patterns with depths exceeding one millimeter. If the substrate is not electrically conductive sputtering or evaporation are used to deposit a seed layer in the next step. Next, the component is produced by immersing the mold in an electroplating bath of nickel, and finally the mold is pressed out to release the part. Due to the necessity for x-ray radiation there is a requirement to use special masks. The masks for the original LIGA process can cost as much as $20,000 and may take up to

3 months to produce, making the process slow and quite expensive. However, LIGA can achieve aspect ratios of 100:1, nearly vertical side walls with an angle as high as 89.95°, smooth sidewalls with surface roughness R_a as low as 10 nm, which is suitable for mirror fabrication, structure thicknesses from as low as a few micrometers to several millimeters, and micrometer size details over an area of several centimeters [6, 12, 26].

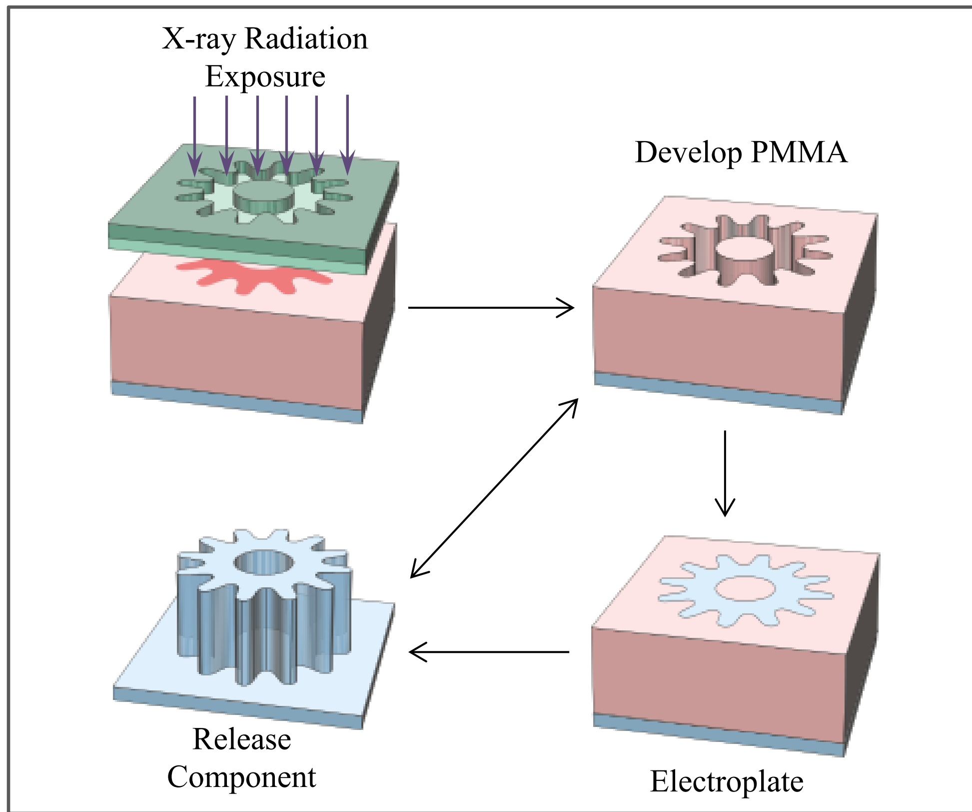

Figure 14. Schematic of LIGA for high aspect ratio MEMS component (adapted from [6]).

Several variations of the process have been developed during the years to reduce cost. One option uses the first component produced by LIGA as a tool to imprint the shape into a polymer cast for making subsequent molds, followed by either electroplating, or using a process called hot embossing (detailed in the next section) to make succeeding components. There is also

UV-LIGA that, as the name implies, exchanges the synchrotron radiation source for an UV mercury lamp and a cheaper chromium mask. The process is much cheaper, but cannot produce precision high aspect ratio molds [6, 26].

2.5.2.3. Hot embossing. Hot embossing is another high aspect ratio, non-silicon based fabrication technique. As mentioned earlier, it uses a tool produced by LIGA or another comparable method to replicate a pattern in a polymer substrate. The tool needs to have the inverse shape of the component to be produced and the process takes place in a specialized system under vacuum (Figure 15) since any air trapped between the tool and substrate will result in feature defects. The tool, substrate, and component material are heated to over the glass transition temperature, T_g, of the polymer and pressed together. After cooling, the mold and part are separated to release the part. Hot embossing can make parts that are hundreds of microns tall, with high-aspect ratios, and excellent dimensional precision at a price much lower than any other technique with the same capability, which makes it very popular in microfluidic component fabrication for the medical industry [6].

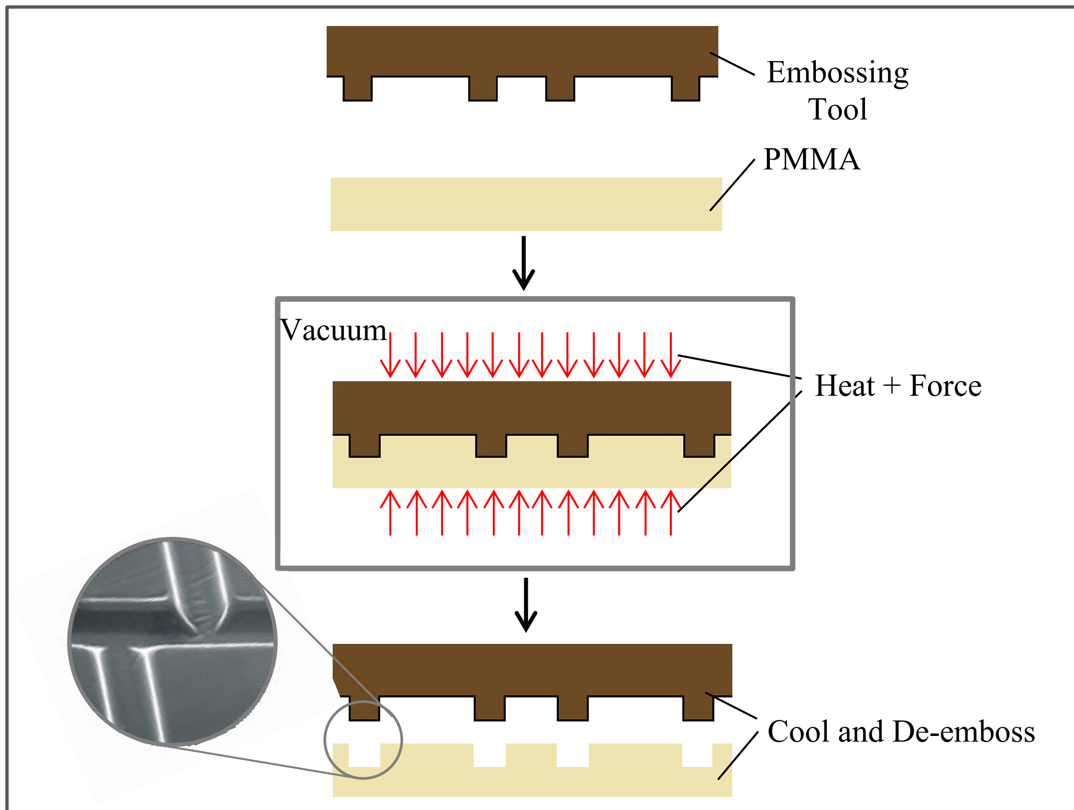

Figure 15. Hot embossing for microfluidic components fabrication (adapted from [6]).

2.5.3. Other fabrication techniques

In addition to the already presented traditional and high aspect ratio techniques that are established as MEMS fabricating methods, there are other emerging techniques that provide unique advantages and applications.

2.5.3.1. XeF2 dry phase etching. As mentioned earlier, xenon diflouride (XeF_2) vapor phase etching is a derivative of RIE where the high kinetic energy ions have been removed from the process; hence it is highly isotropic, allowing the undercut of very large structures [27]. The process is done with equipment that is less elaborate and cheaper than RIE. The substrate is placed in a chamber where the reactive gas or gasses are introduced, and the surface is dissolved by the reaction with vapor molecules (Figure 16).

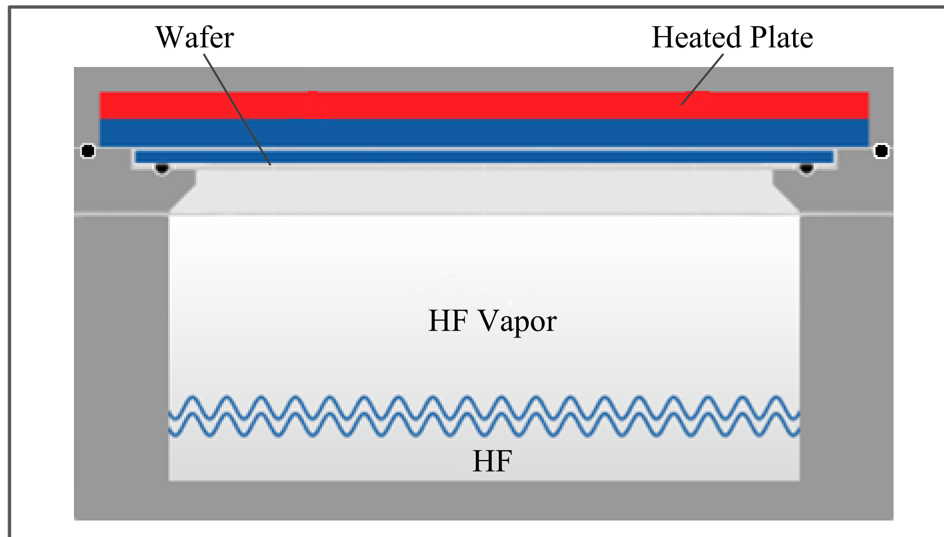

Figure 16. Vapor (dry) phase etching using HF [27].

XeF_2 dry phase etching is used for silicon etching; being a dry etch method, xenon diflouride processing does not exhibit stiction problems. What is unique for this chemistry is its very high selectivity toward pretty much any other material used in microelectronics and MEMS fabrication, including silicon nitride, thermally grown silicon oxide, and metals such as aluminum and titanium, photoresist, and more. The excellent etchant selectivity (1000:1 have been reported) and no loading effect, makes this the preferred method for micromachining exposed silicon in the passivation layers of already pre-processed CMOS wafers. Its main disadvantage is the low etch rate (about 16 μm per hour or 0.27 μm per minute), which is considerably slower than DRIE and even wet etching methods [6, 27].

2.5.3.2. Electro-discharge micromachining. Micro electro-discharge machining, or micro-EDM as its macro machining equivalent, is a process that can be used to micro-machine conductive metals by means of electrical breakdown discharge. Micro-EDM uses a small conductive electrode to apply high-voltage pulses that are used to remove the material when the electrode is brought into close proximity to the work part in the presence of a dielectric fluid

(Figure 17). Resolution depends on the size of the electrode, but features as small as a few tens of micrometers have been demonstrated. EDM is a sequential process and that makes it slower than most of the technologies discussed so far [6, 28].

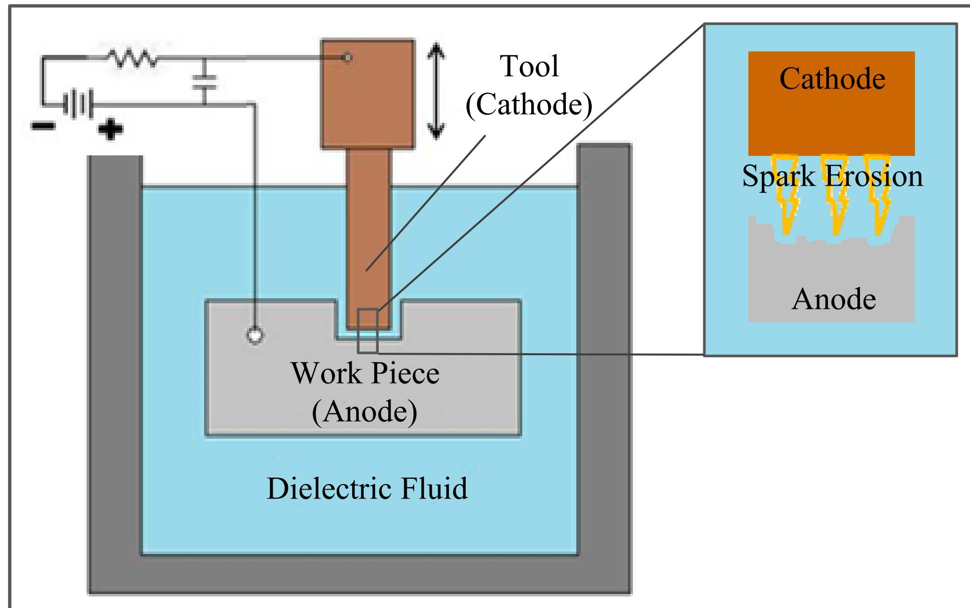

Figure 17. Schematic of electro-discharge micromachining (adapted from [28]).

2.5.3.3. Focused ion beam micromachining. Focused ion beam (FIB) microscopy and micromachining have been known in the semiconductor industry since the 1980s and used primarily for offline mask and circuit repair, but commercial FIB systems became available in the middle of last decade. Ion beam systems are very similar to scanning electron microscopes (SEM), but as the name implies they use a beam of focused ions rather than electrons (Figure 18). In fact, many of the commercial systems today are dual beam platforms utilizing FIB and SEM in one apparatus [29].

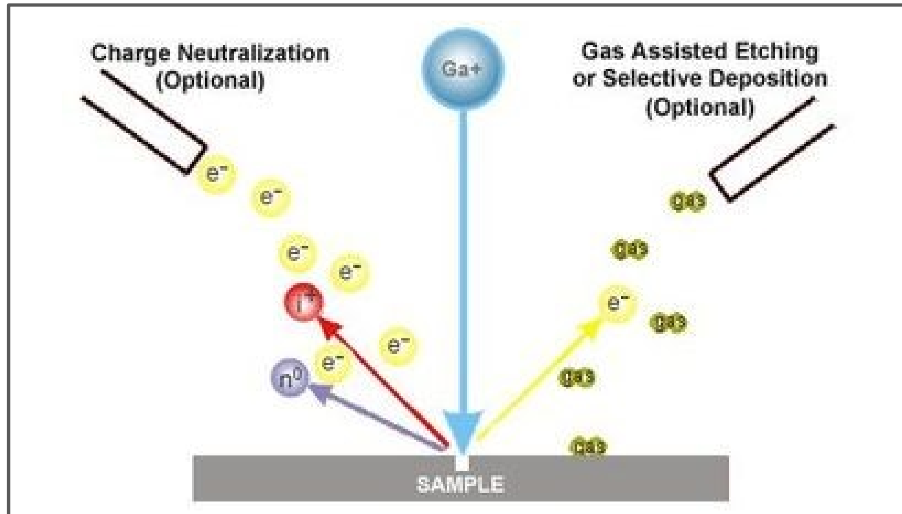

Figure 18. Focused ion beam micromachining material interaction [29].

FIB is becoming more popular as it offers high resolution imaging (through secondary electron ejection) and micromachining (ion beam machining) combined with sputtering and deposition capabilities, implantation doping, lithography, mask and device repair, and device diagnostics in a single tool [6, 29]. Most commercially available systems use gallium (Ga) ions, because gallium has a low melting point (30°C), low volatility and vapor pressure, and is inert toward tungsten (W), the usual choice of material used to fabricate the tool injection needles [29, 30]. The beam spot size in FIB can be focused down to about 5 nm, which allows micromachining features in the nanometer range with a resolution of about 10 nm, which benefits applications like fabrication of nanostructures on waveguides for integrated photonic devices [29, 31].

2.5.3.4. Laser micromachining. Lasers work by the action of concentrated amounts of energy contained within very short pulses of light in the optical beam that is focused onto the material being micro machined. The mechanism of material removal can be by optical absorption leading to melting and vaporizing (silicon, metals), or by photo ablation by UV radiation

(organics) depending on the type of laser used and the material machined. Laser processing is noncontact, but it has high three-dimensional confinement.

There is a plethora of different kinds of lasers used in MEMS fabrication today, among them Nd:YAG, Nd:YVO_4, excimer, and more. What type of laser will be used in a particular application depends on a large number of factors, namely material properties such as absorption and thermal conductivity, feature size and tolerances desired, processing speed, cost, etc., as well as laser wavelength, energy and power requirements. Although lasers can provide extremely high processing speeds the process is essentially serial (Figure 19), just like EDM, and therefore slow when thousands of features or MEMS components need to be created [6].

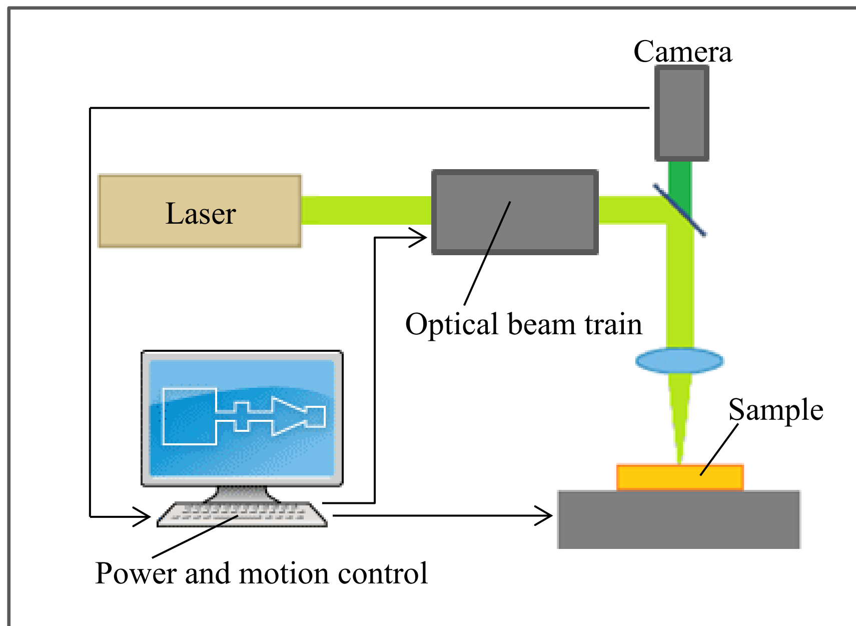

Figure 19. Schematic of a typical laser micromachining setup.

Conventional laser micromachining with continuous or longer wavelength lasers (such as CO_2 and non-harmonically coupled or tripled Nd:YAG) cannot create micron-sized structures because at their native wavelength the linear optical absorption of materials leads to heat

deposition with a large heat affected zone (HAZ), micro-cracking, and unavoidable damage to the surrounding areas. A new class of the so called ultrafast pulse lasers, which operate with pulses in the picosecond (10^{-12} second) to femtosecond (10^{-15} second) range, is rapidly advancing in the field of laser micromachining. These new high-power lasers are capable of processing a wide variety of materials, including glass and quartz, and can produce three-dimensional structures with micron and even sub-micron tolerances and will be discussed in more detail in the beginning of Chapter 4.

2.6. MEMS Assembly

As shown already, micromechanical systems of remarkable complexity can be obtained without any assembly using the micro machining techniques presented so far. Nonetheless, there is growing interest and need for the development of MEMS assembly technologies where devices are built in separate processes and are later integrated in a complex system using assembly. Some of the obvious motivations include the restrictions imposed by using a limited number of materials, yield losses due to the high number of masks needed for complex devices, the compromise that monolithic integration brings to both the electronic and mechanical parts of a system, and the incompatibility between materials and methods when a single process is used for different devices [10, 12].

Micro assembly can be divided into two broad categories, serial and parallel. The first category is best described as extension of the conventional “pick-and-place” and flip chip assembly into a micro territory. These processes suffer from scaling effects where surface forces of attraction become dominant at dimensions typical for MEMS and require complex robotic systems that are restricted by speed and cost. The throughput in this case depends solely on the number of robotic manipulators in the system. The second group includes the simultaneous

assembly of thousands and even millions of components by either wafer-to-wafer transfer (also known as deterministic parallel assembly) or self-assembly (also known as stochastic parallel assembly) [10].

2.6.1. Serial micro assembly

Although it is possible to improve the precision of conventional automated robotic systems for repeatability and resolution in the micron to sub-micron range, assembly of micron sized components cannot simply be scaled down from the macro world. It is already recognized that the smaller the parts to be assembled get, the bigger and more complicated the machines that can handle them need to be [32].

Although there have been a large number of publications and many clever approaches to serial micro assembly, not one has been applied to a commercial scale to the best of the author's knowledge. The main reason is the scaling of forces since insignificant at the macro domain forces become prevalent in the micro scale. For macro parts the dominant force is gravity, but as parts that need to be handled get below 1 mm in size, the gravity force decreases until surface interaction forces such as van der Waals and electrostatic attractions become predominant. Hence, although it has been shown that it is possible to fabricate tiny forms of conventional robotic grippers, an interesting challenge becomes the hierarchy of adhesive forces. For example, in order to pick and place a tiny part from point A on a carrier substrate to point B for assembly, the adhesion of the component to the substrate should be higher than the adhesion to the micro gripper before any force is applied in order to allow accurate location of the part in the gripper. When releasing the part in its final location, however, the adhesive force holding the part to the opened gripper needs to be less than the one between the part and the final substrate so the

component can be released in the precise position. Remember that gravity has negligible effects at this scale [32].

2.6.2. Parallel micro assembly

Deterministic parallel assembly is a direct wafer to wafer transfer of microstructures. The placement of the structures in this case is prearranged by their location on the donor wafer and the assembly process consists of simply guiding the devices to their final position and establishing a bond with the target substrate. The main challenge in this sequence is the bonding step since this is the place where most of the failures occur. Yield can be increased with optimization of the electroplating and bonding steps [10].

Stochastic parallel assembly or self-assembly promised more than 15 years ago to address the gap between batch fabrication methods, capable of producing millions of components, and assembly techniques, that can handle a few thousand components per hour. The basic idea behind self-assembly is that matching sites on the substrate and micro components with complimentary shape will self-align spontaneously due to free energy minimization.

Some unique stochastic parallel assembly methods such as fluidic self-assembly (FSA) [33, 34] and even single bead-manipulating apparatus using micro vacuum tweezers [35] and others [36, 37] have been suggested as alternatives to pick-and-place assembly with various degrees of success. FSA was heavily promoted by the Alien Technology Corp., as a technique for parallel assembly of large numbers of electronic components that is still considered by some authors as one of the most promising solutions to the packaging dilemma [38, 39]. In this process the bare dies (pieces of silicon wafer with the IC device fabricated on them) with a typical size of several hundred micrometers and a flattop pyramidal shape are suspended in liquid and flowed over the receiving substrate that has correspondingly shaped receptor holes into which the dies

settle and self-align. Alien has successfully demonstrated FSA for assembly of tens of thousands of RFID chips. Some of the problems with FSA are related to the shape and orientation control of the dies. Since the substrate is submerged in the processing liquid and receptors need to be precisely shaped in it, FSA is limited in the number and type of substrate materials. But maybe the biggest issue with FSA is that it places the die on the substrate face up. Subsequent post assembly processing steps such as coverlay bonding, via hole drilling and plugging, and interconnect metallization need to be employed, which has an adverse effect on the production cost [40].

Dry stochastic parallel assembly methods have also been suggested and demonstrated, but they rely on vibration to move components to the receptor site, which can use electrostatic attraction forces, for example, to fit the part in place. However, as the size and mass of the elements used is reduced, vibration becomes less efficient and consequently higher amplitudes and frequencies need to be employed [10].

2.7. Laser-Based MEMS Fabrication

Laser based micromachining and laser assisted components transfer and assembly will be presented in more detail next because lasers are becoming more and more popular in MEMS manufacturing. Modern laser systems can process virtually any solid material and offer the unique capability for direct or indirect 3D structure micromachining for micron sized structures with tolerances that now fall below the sub-micron range. These are significant advantages over some more established micromachining techniques that were discussed in Chapter 2. Some of the most frequently used lasers for commercial micro machining are shown in Table 2, but this list is far from complete.

Table 2. Types of lasers used in MEMS micromachining [12]

Laser Type	Wavelength	Pulse Duration	Pulse Energy	Repetition Rate
Excimer (ArF, KrF, XeCl)	193, 248, 308 nm	~ 20 ns	100 – 500 mJ	up to 500 Hz
nω Nd:YAG, nω Nd:YVO_4, (n = 2, 3, 4)	532, 355, 266 nm	~ 10 ns	a few mJ	up to kHz
Ti:sapphire	775 nm	~ 150 fs	~ 1 mJ	up to kHz
Nd:YAG, Nd:YVO_4	1.064 μm	~ 10 ns	~ 10 mJ	up to kHz

2.7.1. Direct laser micromachining for MEMS

The process of laser micromachining can be fundamentally described as the direct etching of solid material by light irradiation through a process of matter ablation [12, 41]. The interaction between high intensity light and solids during ablation is a fairly complex process that depends both on material characteristics and numerous laser parameters, mainly light wavelength, pulse duration, and pulse intensity [41]. In all cases the absorbed light energy leads to an ejection of material from the material surface, but the mechanisms that govern it are different. Ablation of metals by continuous wavelength (CW) and long pulsed, micro- and nanosecond lasers (pulse duration from 10^{-6} to 10^{-9} seconds) is due to linear absorption (excitation of atoms). Micro machining of organic material such as polymers with UV lasers work by photo ablation. In ultrafast pulse lasers the mechanism is non-linear absorption. These different material removal processes lead to variances in HAZ size and from there to different surface and edge quality, thermal damage, precision and resolution [41]. The CW laser material removal is due mostly by melting, which creates a large HAZ (Figure 20, *left*). The melt layer is ejected from the interaction zone, resulting in geometric changes to the features and material re-deposition and solidification. Due to this reason CW laser precision and resolution are not

sufficient for micromachining of MEMS, but CW lasers find ample applications is macro machining [42].

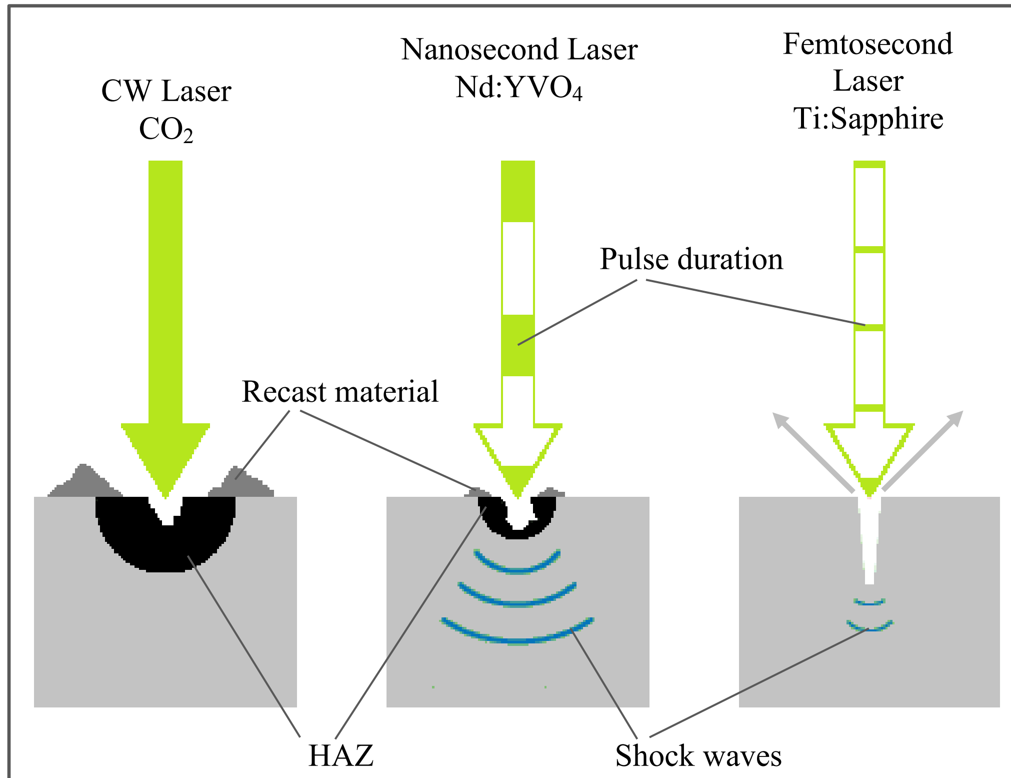

Figure 20. Schematic of light-solid interaction for different types of lasers (adapted from [42]).

The nanosecond laser pulses (Figure 20, *center*), typical for excimer lasers, create a smaller HAZ and material is removed by melt expulsion driven by the vapor pressure created during light absorption [42]. Excimer lasers are very popular in MEMS micromachining today because they provide high resolution due to their short wavelength. In addition, since most materials readily absorb UV light, material removal rate is small, typically between 0.1 μm and 1 μm per pulse, which provides precise depth control simply by pulse counting. Excimer lasers compensate for their slow repetition rate by taking advantage of their high pulse energy (see

Table 1). Areas of several square millimeters are processed in parallel by using a projection mode where a mask is used over the work piece to transfer the image [12, 43]. In contrast to excimer lasers, frequency tripled and quadrupled Nd:YAG and Nd:YVO4 lasers that also operate in the UV range, 355 and 266 nm respectively, offer small pulse energies, but high repetition rates. They also provide much better beam quality and smaller spot size and are operated in scanning mode, which makes them particularly suitable for prototyping and re-work. Nanosecond UV lasers can ablate a relatively wide range of materials, but they are very well suited for micromachining of polymers which strongly absorb UV light. That, in addition to low thermal conductivity, minimizes HAZ and collateral damage to the material and provides good surface finish and dimensional control [12]. Direct excimer laser micromachining has been shown for numerous applications such as microfluidic devices [44] and patterning of silicon and magnetic materials for actuators [45, 46], and has been established as the preferred technique for at least one commercial MEMS product, most notably the fabrication of ink-jet printer heads [12, 47, 48].

In ultrafast lasers pulse duration is in the range from 10^{-12} to 10^{-15} seconds. This is a much shorter time than it takes for energy to transfer between the free electrons and the material lattice which means the material vaporizes without going through the melted state (Figure 20, *right*). Although extremely high temperatures and pressures are reached, vaporization occurs without heat generation and material is removed away from the surface without formation of a recast layer. Femtosecond lasers ablate the material by a mechanism of non-linear absorption (excitation of electronic energy level) and deliver negligible HAZ and very fine, sharp features. This is also what makes it possible to micro machine solids that are transparent at the wavelength of these lasers [42].

Femtosecond lasers can also machine wide band gap materials (band gaps greater than 5 eV) because at the high intensities (typically above 10^{13} W/cm^2) at which they operate multi-photon ionization becomes significant. Because of the very high photon flux during multi-photon ionization several photons strike a bound electron all together at the same time. The electron is freed from its valence band when the total energy of the absorbed photons surpasses the ionization potential leading to avalanche ionization [41, 42].

Femtosecond lasers are rapidly advancing in MEMS micromachining because the process is not dependent on the linear absorption of the material at the laser wavelength, therefore virtually any dielectric, metals, or mechanically hard material can be removed by the same laser beam without incurring any thermal damage to the material.

2.7.2. Laser-LIGA

The traditional LIGA process, discussed in detail previously, is expensive and requires mass production to be economically viable. In addition, very few facilities have access to an x-ray light source. Another limitation of the LIGA process comes from the lithographic nature of the process; although it is easy to produce fine features with vertical sidewalls, producing a continuous 2D or 3D relief is virtually impossible (Figure 21), which limits the variety of shapes that can be produced, hence its applications.

Laser-LIGA was developed to address the shortcomings of the original LIGA technique and was first reported by Arnold and his team in 1995 using a 193 nm excimer laser and photoresist to create single level molds in PMMA, and a year later a modification by Lawes and coworkers who used the projection mode of a 248 nm excimer for direct ablation of PMMA [49, 50].

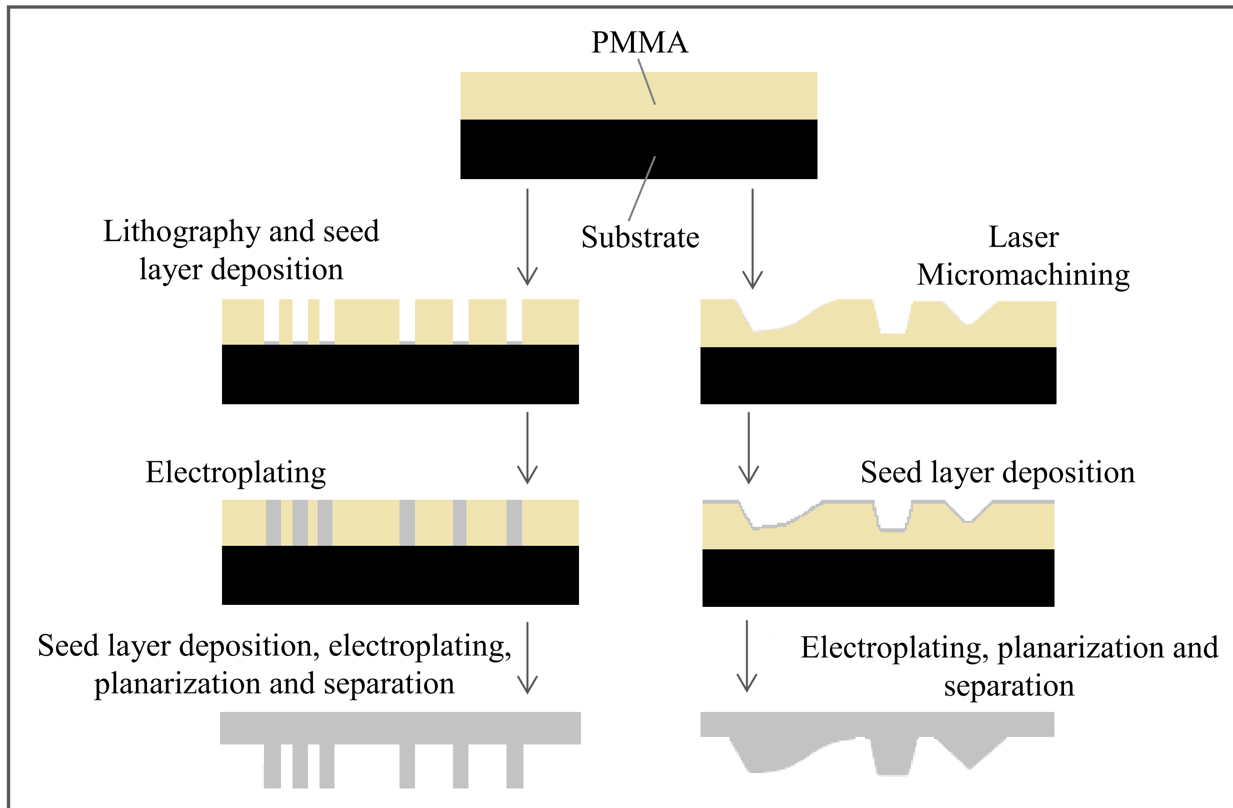

Figure 21. Traditional LIGA showing vertical structures (*left*) vs. laser-LIGA (*right*) continuous relief (adapted from [12]).

Laser-LIGA is much cheaper than traditional LIGA and suitable for making complex 3D molds in order to produce quality parts from materials that are not appropriate for direct laser ablation. Although laser-LIGA has not been established as a common fabrication technique, various mechanisms such as micro motors and turbines, as well as optical components and microfluidic devices have been demonstrated by several research groups [47, 51-54].

2.7.3. Laser-assisted chemical etching and deposition

Laser-assisted etching and deposition are modifications of well-known subtractive and additive processes that use the energy provided by the laser beam to improve a local reaction.

In laser-assisted chemical etching (LACE) the removal of material is enhanced by laser light by mechanisms of thermal stimulation by the heat provided to the substrate and/or by

pyrolythic or photo-generation of active agents in the etchant chemistry [55]. LACE was first demonstrated in the 1980s and in the 1990s was applied in chlorine etching of silicon [56, 57] and fabricating various MEMS components and devices by potassium hydroxide (KOH) enhanced etching of shafts for rotating bearing structures [54, 58]. As a fabrication technique LACE has been surpassed by DRIE, but it remains capable and today is primarily used for prototyping and re-work [12].

Currently the two most widely used laser-assisted deposition methods are laser chemical vapor deposition (LCVD) and pulsed laser deposition (PLD). The latter is a technique that ablates a solid target and re-deposits the material onto the substrate. The equipment and basic principle of pulsed laser deposition is very similar to magnetron sputtering and just like magnetron sputtering PLD takes place in a partial vacuum and coats unselectively the whole substrate [12]. PLD uses high power pulsed excimer lasers that produce energy intensive short pulses that vaporize the target material upon irradiation and create a plume of plasma (Figure 22). The plasma, that is essentially a jet consisting of ablated particles, expands as it moves away from the target and condenses onto the substrate. The size of the plasma plume at the work piece can be controlled by adjusting the distance between the target and substrate or for very large areas the substrate can be rotated in order to cover the whole area. Alternatively, the laser beam spot can be scanned across the target surface to increase the coated area [59].

The technique is popular because it enables the application of high-melting point materials as well as multi-element materials in MEMS. PLD has been used to deposit thin films for piezoelectric actuators, shape memory alloys, and more recently diamond-like carbon film that are used as protective coatings and have been shown to reduce friction in sliding MEMS structures [60-62].

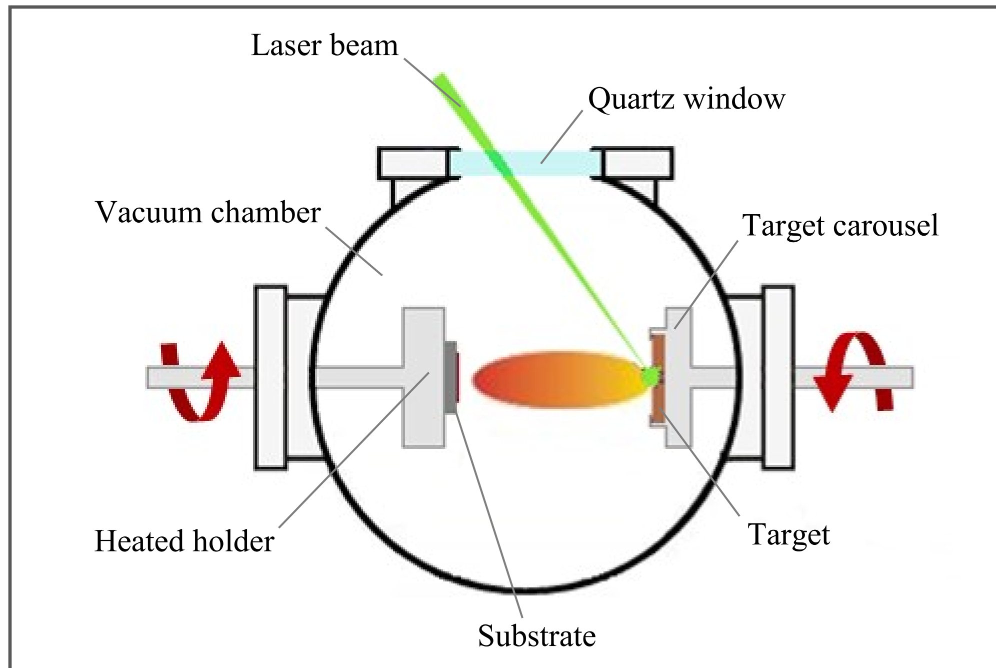

Figure 22. Pulsed laser deposition of thin films (adapted from [59]).

Laser-assisted chemical vapor deposition (LCVD) is a modification of the traditional CVD method that, similar to PLD, also takes advantage of the high energy contained in excimer laser pulses. This technique uses laser radiation to enable localized gas reactions and material deposition at substrate temperatures much lower than the ones needed to achieve thermal equilibrium and chemical reaction in the original CVD process, allowing thin-film deposition on temperature sensitive substrates. The inherent directionality of the laser beam allows for very precise dimensional control and more importantly enables one to selectively deposit material over non-planar surfaces [63]. LCVD is mainly used to selectively deposit metal thin films on various substrates, but free-standing 3D structures have also been demonstrated [12, 64]. Other laser-assisted deposition techniques, based on spin coated precursors, aerosol deposition, and material transfer from a carrier ribbon for direct write applications, have also been reported in the

literature, but due to their limited applicability and flexibility will not be discussed in more detail [12, 65, 66].

2.7.4. Stereolithography

Although as a technology stereolithography was first introduced in the 1980s, its first use as a MEMS fabrication method was reported in 1993 [67]. Stereolithography is an additive manufacturing technique that uses a UV laser to cure a liquid photopolymer one layer at a time allowing the creation of complex stationary and moving 3D structures with resolution down to a few micrometers (Figure 23). The process requires a support table or structure and the CAD file of the part to be created is dissected into thin layers, typically 0.05 to 0.15 mm thick. The UV laser traces the cross section profile of the first "slices" to solidify the photopolymer at which point the support table moves down and a blade is run over the part to introduce a fresh layer of liquid material. The process is repeated until the whole structure is created. Next, the part is removed from the tub, chemically cleaned, and further cured if needed. The parts created are strong enough to be used as standalone structures or as molds for other subsequent processing.

Although relatively slow for mass production and limited from a materials point of view, the exceptional 3D capabilities make stereolithography a very useful prototyping tool [12]. Integrated structures with fixed and moving parts as well as actuators and microfluidic devices have been demonstrated by Ikuta *et al* between 1994 and 1998 [68-70]. About the same time, intricate micro-turbines, gears, and axles made by a modification of stereolithography that uses UV lithography and a pattern generator to overcome speed constraints, were presented by A. Bertsch and his team [71].

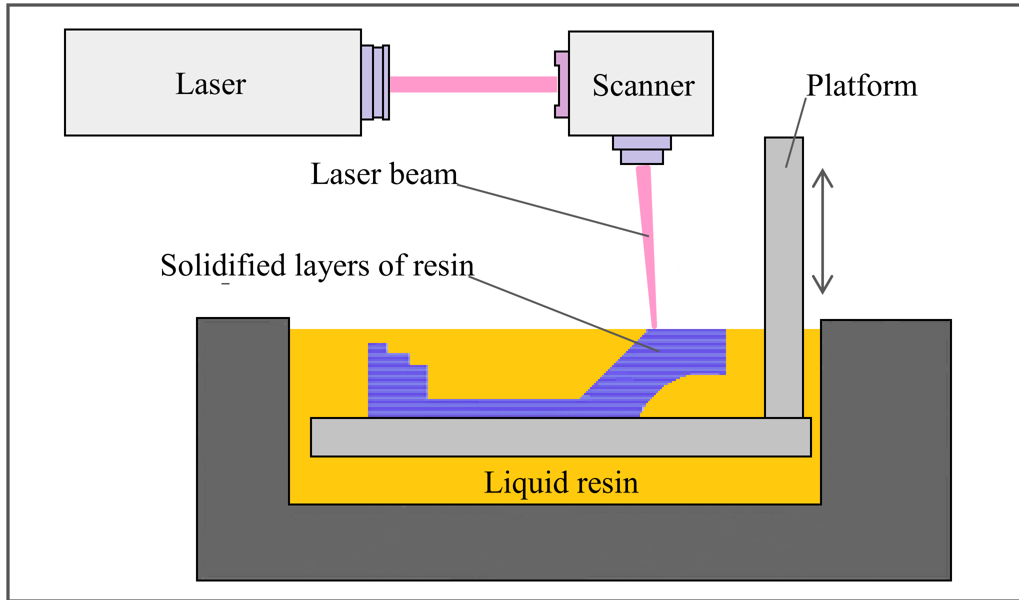

Figure 23. Schematic of UV laser stereolithography.

2.7.5. Multi-level hybrid processes

The original LIGA process as well as its alternative laser- and UV-LIGA equivalents can be described as single-level replication processes which restrict the design of devices that can be produced. Additionally, neither of the two is economically viable for different reasons. The traditional LIGA is a parallel, projection process that is fast, but uses expensive and specialized equipment that is not always readily available. Laser LIGA uses cheaper and more common equipment, but it is a serial, direct-write, micromachining process, which makes it slow, hence expensive to run. Finally, UV-LIGA, although a fast projection method, has limitations on the resolution and precision that it can achieve.

A hybrid, multi-level replication process was demonstrated by Holmes [47] and his team, at Imperial College in London, in an attempt to address the shortcoming of all the processes just summarized. The method developed uses a combination of conventional UV lithography and laser micromachining in order to alleviate the shortcomings of both. Laser micromachining was

used for layers with significant thickness, more than 50 μm, while UV lithography was reserved for thinner layers in order to decrease processing time by taking advantage of projection micromachining. The idea behind this multi-level process is to allow the fabrication of more complex components such as turbines with shafts and overhang features by using middle level seed layers. Figure 24 compares and contrasts the single-level and hybrid multi-level fabrication techniques.

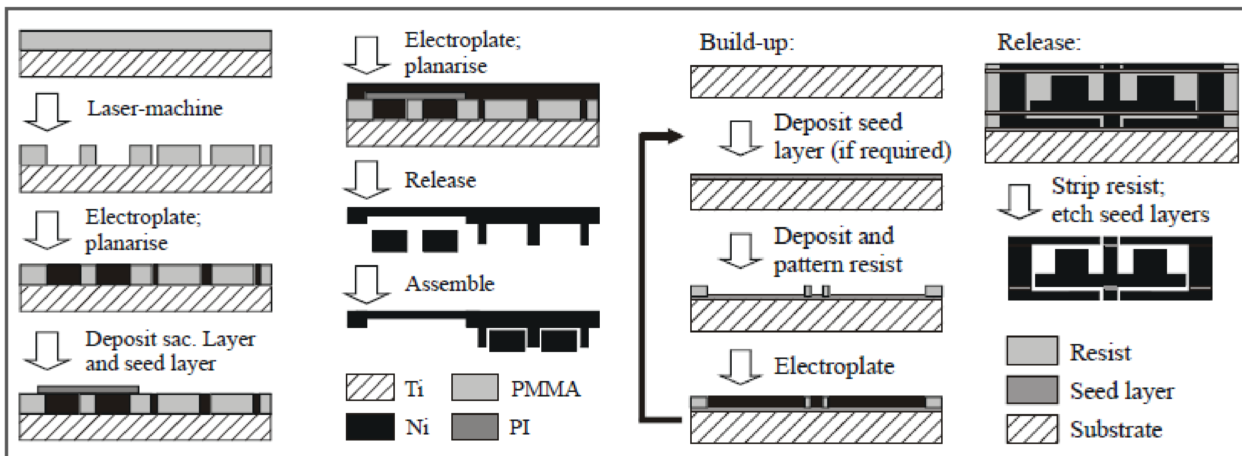

Figure 24. Single-level process (*left*) vs. multi-level hybrid fabrication approach (*right*) [47].

As seen in Figure 24 right, the multi-level process is comprised of three basic steps that are repeated as necessary:

1) Seed layer deposition and patterning if needed.
2) Photoresist application and patterning.
3) Metallization.

The seed layers were sputtered copper as copper etchant provides very good selectivity toward the electroplated nickel used for structure fabrication. The PMMA, usually used in LIGA processes, was substituted for liquid and dry photoresist layers as they are easier to apply,

process, and remove while providing better uniformity. In addition, PMMA shows poor adhesion to seed layer metals such as copper [47]. Three different types of resist were used as needed based on the thickness desired, two kinds of liquid, spin-coated photoresist (for layer thicknesses of up to 2 μm and from 5 to 20 μm, respectively), and a dry photoresist film for casting layer thicknesses over 20 μm [47]. The mechanisms demonstrated included air driven micro turbines with up to six levels of processing repetition.

Despite the complex structures and functional devices that were presented by this research group, they also acknowledge in their publications the fact that micro assembly for MEMS is falling substantially behind MEMS design and fabrication [12, 47, 72]. Many devices and systems that are currently of interest cannot be built simply because they are too complex for the repetitive sequence of deposition and etching steps which encompass monolithic fabrication and assembly (on one substrate). Hybrid fabrication and assembly techniques where structures are built on separate substrates and consequently assembled in functional mechanisms are an important next step needed in order to further increase device complexity and design flexibility while increasing throughput and minimizing cost, consequently affecting future MEMS development and market expansion. One possible approach that will be investigated in more detail next includes laser transfer, manipulation, and assembly of components for MEMS.

2.8. Laser-Assisted Assembly for MEMS

In the context of MEMS laser aided manipulation and assembly can be divided into three distinct groups, monolithic assembly, hybrid assembly, and operations for laser joining.

2.8.1. Monolithic manipulation

The term monolithic assembly refers to fabrication and manipulation of structures on a single substrate where some movement and reconfiguration of the fabricated components is

possible in order to produce the device, but the components generally stay on the original substrate. In that aspect monolithic assembly should be more properly referred to as monolithic manipulation or guidance as no actual component assembly is performed. Nonetheless, more than a few techniques for monolithic manipulation have been demonstrated to date, some of them using very clever methods to move parts out of plane (Figure 25). Some interesting optical MEMS components have been demonstrated and produced by folding etched silicon structures [73-76].

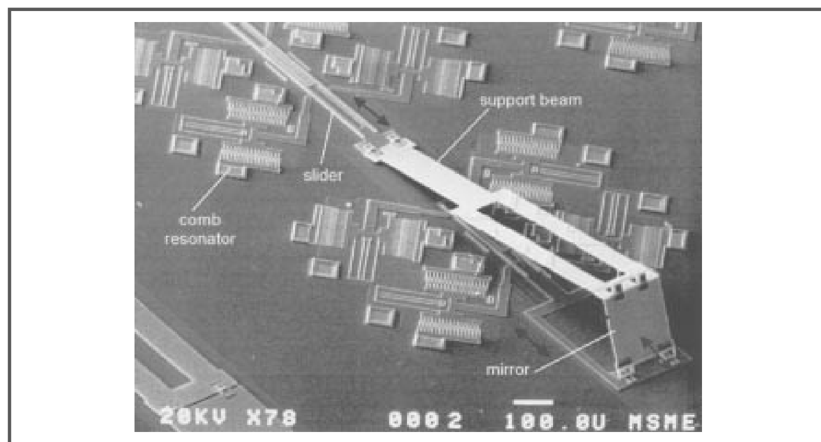

Figure 25. Self-actuated micro mirror; vibromotors, using comb drives move the front and rear sliders for out of plane rotation of the mirror [73].

Folding and rotation of structures has been accomplished by a number of different driving forces such as electrostatic force, surface tension forces, and resistive heating which was used to deform, separate, and weld microstructures [73, 74, 76]. Lasers have also found application in monolithic manipulation. The ability of lasers to concentrate a substantial amount of heat in a small area was used to generate thermal stresses by asymmetric heating, leading to plastic deformations which in turn move the component [75]. As ingenious as some of these techniques are, they are still limited to the original substrate and unable to move a part from one

substrate to another or to transfer complete devices between a temporary handle wafer and the final substrate and will not be discussed in more detail here.

2.8.2. Hybrid laser-assisted assembly

Hybrid assembly is the next step up from monolithic assembly and is expected to provide the means of increasing MEMS device complexity by allowing multiple components fabricated on different substrates by diverse manufacturing techniques to be assembled into a functional device. As mentioned earlier hybrid micro assembly involves the transfer of parts from one substrate to another and involves three specific steps:

1) Release of components and parts from the substrate or wafer where they were built.
2) Transfer to a specific location on the target substrate.
3) Fixing or joining the parts in place.

This method of manipulation allows transferring one part at a time or multiple components simultaneously. Hybrid assembly was first introduced in 1998 by Andrew Holmes and his team at the Imperial College in London and was extensively investigated by the group in the following years. Basically the process involves the release and transfer of components fabricated on a transparent carrier to a target substrate placed in close proximity by means of ablation of a sacrificial bonding layer with an excimer laser through the transparent carrier [12, 47]. Their assembly process, shown schematically in Figure 26 involves five distinct steps:

1) Carrier preparation.
2) Component fabrication.
3) Alignment of carrier and receiving substrates.
4) Laser transfer.
5) Cleaning of the sacrificial layer.

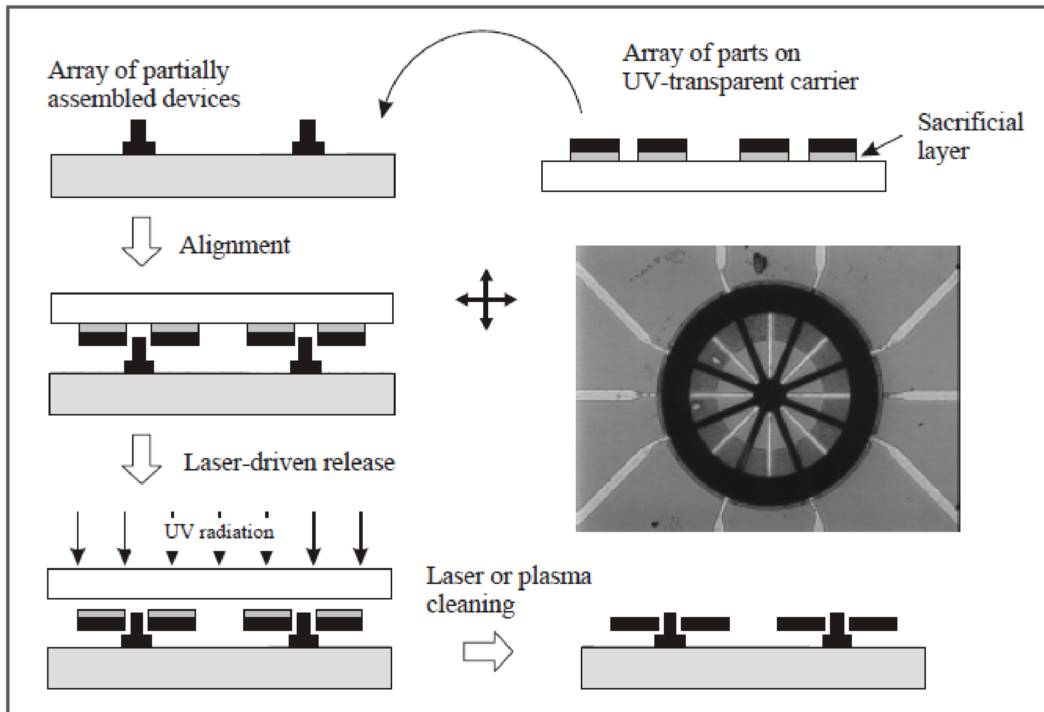

Figure 26. Hybrid laser-assisted micro assembly of parts for MEMS [12].

The process, as shown in Figure 26, can be parallel or serial. In the first case, the components on the carrier and receiving substrates need to have the same step size in both x and y directions; the two wafers are aligned once and the parts are released from the sacrificial carrier. This batch assembly method is faster than the sequential one where alignment is needed before each release and only a small area of the sacrificial layer is exposed using a mask. However, sequential assembly provides more flexibility and allows utilizing completely the fabrication wafer area. The decision on which method to use can be one based on economics.

Although functional devices such as electrostatic wobble motors were assembled and demonstrated by using both the sequential and batch assembly methods, the research group also acknowledged some shortcomings of the method. Repeatable, precise, and accurate transfers were obtained only in cases where the transfer gap between the carrier and receiving substrates was smaller than the height of the element to be transferred, which in the case of the wobble

motor was 15 μm or less. As the gap increased beyond the element's height, the lateral displacement of the part during transfer made accurate assembly impossible. The same findings were reported in a previous study of the ablative laser release mechanism involving nickel pads and frames [77]. In the same preceding study the release velocity of the components was also investigated and found to be as high as 5 ms^{-1}, which are potentially damaging values especially for electronic and already assembled devices. All these weaknesses were attributed to the ablative nature of the laser release mechanism used, which will be discussed in more detail in Chapter 6.

2.8.3. Joining operations

Moving a component to its intended location is only one of two steps required to produce an assembly. The second essential step is joining or fixing the component in place or securing its location in the case of a moving part. The ability of a laser to apply heat locally and with high precision has been recognized and adopted years ago by the industry for joining operations ranging from heavy welding to soldering of electronic components [12]. Micro- and nanosecond pulse lasers such as Nd:YAG, have been applied in MEMS for micro welding of polymers where one polymer is transparent to the laser wavelength while the second one is absorbing (Figure 27). The laser beam, coming through the transparent side and incident on the interface and absorbed by the non-transparent material, applies heat to the structure internally joining the two materials. This technique was applied to a MEMS micro pump membrane [78].

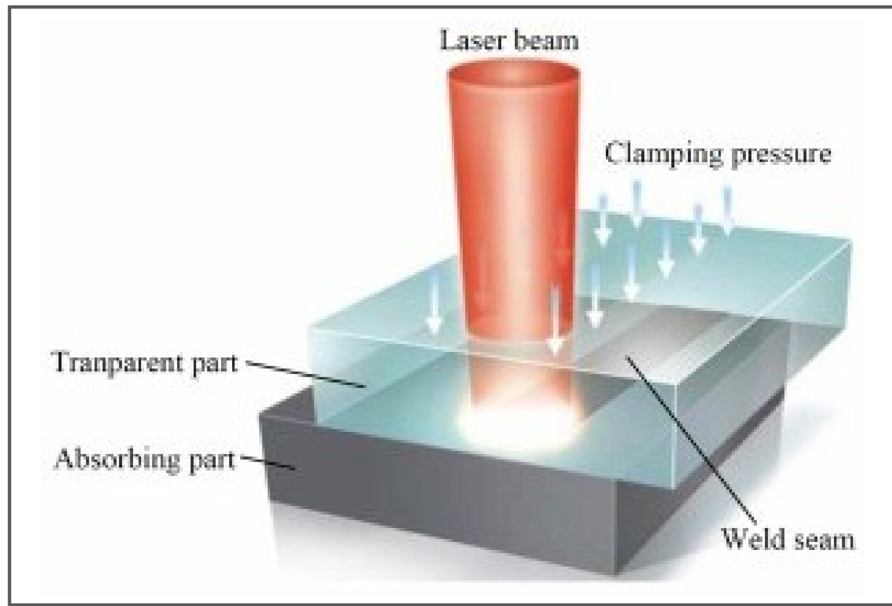

Figure 27. Welding of transparent with absorbing material using nanosecond-pulse laser [80].

More recently, femtosecond lasers were applied to fusion and welding of transparent materials such as different kinds of glass [79, 80]. As discussed earlier, the high peak intensity of the laser pulse in these lasers induces nonlinear absorption mechanisms in transparent materials such as clear polymers and quartz. The absorption occurs at the focal point inside the transparent material, and, although a single femtosecond pulse applies minimal heat at the spot, the repetitive, rapidly overlapping pulses deposit enough heat to melt and modify the material creating a joint (Figure 28). Accurate control of the thermal load can be achieved using scanning and/or translation velocity and pulse repetition rate.

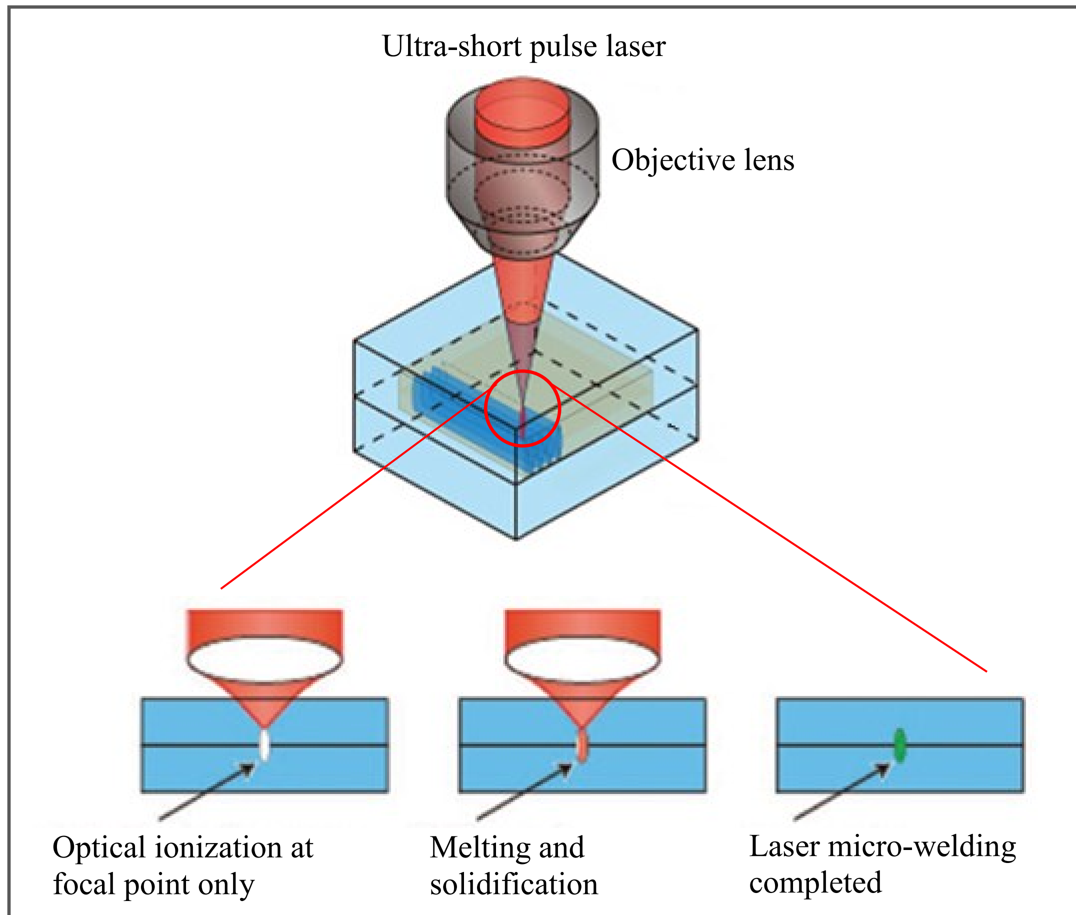

Figure 28. Femtosecond lasers joining of transparent materials (adapted from [80]).

An interesting, hybrid approach to parts joining for MEMS applications, was demonstrated by Holmes [47]. The method called bond-and-release is a variation of the laser assembly technique previously described. In this iteration, the part to be transferred is brought into contact with a component on the receiving substrate and bonded prior to laser release (Figure 29).

The ends of the two corresponding parts in Figure 29 are coated with a thin layer (3 µm) of electroplated gold and joining is achieved by thermosonic bonding using an ultrasonic head. In this case the laser is used not to transfer the component over an air gap but rather to simply release it from the carrier substrate. The electroplated gold can be substituted for solder material

attachment and this method was demonstrated for MEMS parts as well as bumping of integrated circuit dies for flip chip assembly [81].

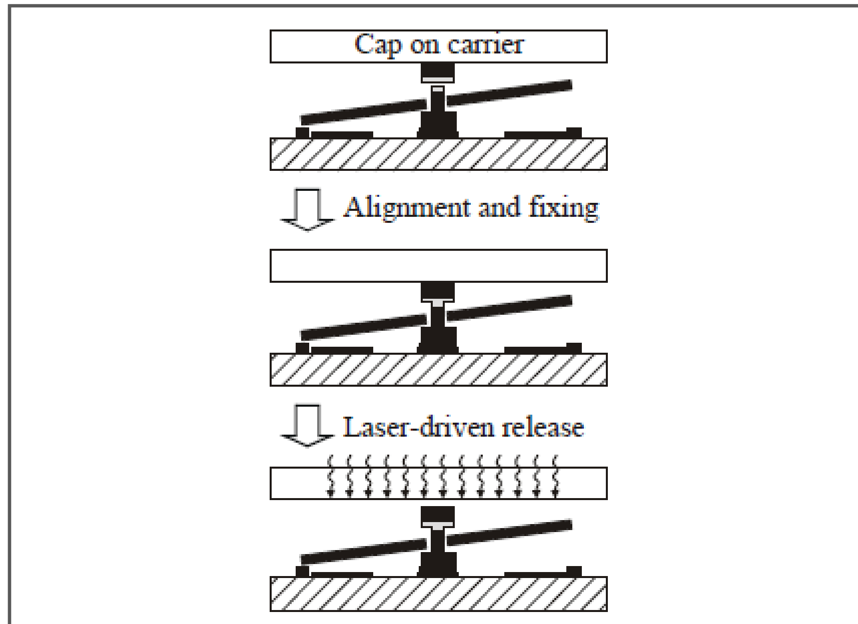

Figure 29. Bond-and-release component joining method [47].

2.8.4. Requirements for micro assembly precision and accuracy

Since it was already debated that the main limitation for the hybrid laser-assisted assembly process shown by Holmes is the low accuracy and precision rather than the assembly rate, this is a good place to discuss the requirements for placement accuracy in micro assembly. When it comes to robotic assembly, such as pick-and-place, the three identifiable parameters that describe the performance of the equipment are accuracy, precision or repeatability, and resolution. These parameters do not play a role in self-assembly processes such as fluidic self-assembly where the main performance characteristic is percent of receptor sites filled, but they are important for laser-assisted assembly techniques even though there is no direct mechanical manipulation of components.

Accuracy and precision, or repeatability, of micro assembly is schematically defined in Figure 30. In pick-and-place micro-assembly accuracy is defined as the ability of the mechanical manipulator to move to a determined location in 3D space from any other position within the range of movement. Precision is the ability to move to the same location repetitively over and over again. The best pick-and-place manipulators that are used today to assemble semiconductor chips achieve 30,000 components per hour with an accuracy of 60 to 100 µm, based on the four-sigma rule of normal distribution, meaning that 99.3% of all attempts fall within the $\pm 2\sigma$ range.

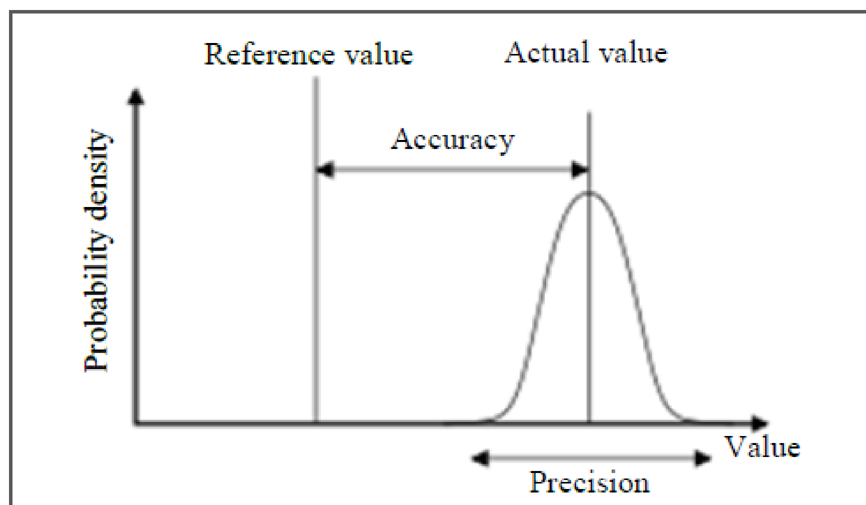

Figure 30. Accuracy and precision in micro-manipulation.

The four possible outcomes of an assembly process based on accuracy and precision are shown in Figure 31; the process can be inaccurate and with poor repeatability, accurate but not repeatable, precise but not accurate, and both accurate and precise.

From the three performance parameters, resolution, repeatability, and accuracy, the latter is the most challenging to achieve. Generally, mechanical robotic manipulators need to sacrifice

speed, hence throughput, in order to increase accuracy or increase speed and throughput at the expense of accuracy.

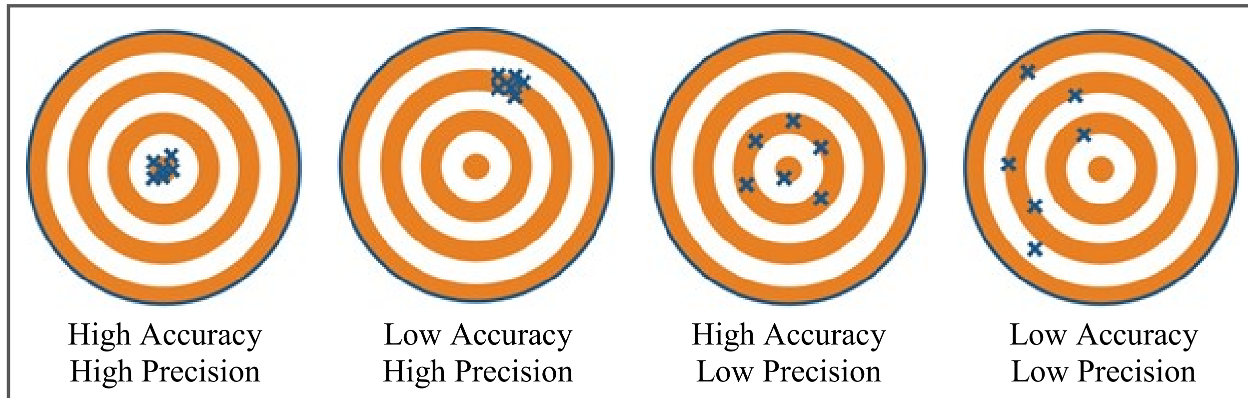

Figure 31. Possible outcomes of a micro assembly process.

For mechanical robotic operations resolution is defined as the smallest incremental step that the apparatus is capable of producing. In laser assisted assembly resolution can be divided into two independent factors. The first one is the resolution of the x-y stages that hold the carrier and/or receiving substrate. They are the mechanical systems involved in these placement techniques, hence their smallest incremental step size will define part of the process resolution. The second factor is the individual component placement accuracy. In laser transfer of components the accuracy is the deviation between the position where the component lands and the intended position of landing on the receiving substrate. So, a perfect transfer will land the part exactly below its original position with no linear or rotational deviation. Impeccably accurate laser transfer systems can increase the process resolution by helping to reduce the pitch between assembled components (Figure 32). In this example a 300 µm square die with pad size and pitch of 50 µm in diameter and 250 µm, respectively, is transferred to conductive pads with a 250 µm pitch and 120 µm width, leaving a spacing between receiving pads of 130 µm. That

means that the die may land +/- 35μm from its nominal position with the die and receiving pads still fully overlapping. By increasing the placement accuracy and reducing the landing track width it is possible to decrease spacing between components, therefore increase resolution. Such a system with perfect precision will be able to reproduce this result indefinitely.

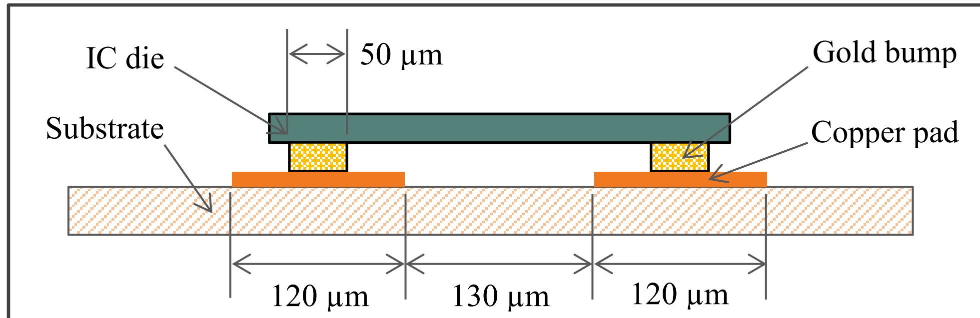

Figure 32. Component placement accuracy; increasing precision and accuracy will allow to increase resolution and to use smaller components (adapted from [82]).

The current standard for placement accuracy requires deviations of +/- 35 μm from a nominal position for a 300 μm square die [82].

2.9. Laser-Induced Forward Transfer (LIFT)

The idea of using laser propulsion dates back to 1971 when Arthur Kantrowitz of the Aveo Everett Research Laboratory described it in “Propulsion to Orbit by Ground-based Lasers”. At the time lasers were considered appealing alternative to chemical propulsion systems [83]. Consequently, the United States Air Force and NASA started building high power lasers and using them to propel projectiles [84]. Fast forward to the late 1990s and early 2000s and the idea of using laser propulsion to move very small components and structures through small air gaps was resurrected by the short and ultra-short pulse lasers.

The concept of laser propulsion is the basis for a technique known as "Laser Induced Forward Transfer" (LIFT) which uses a polymeric sacrificial layer to attach the components to be transferred to a laser-transparent carrier. The sacrificial material coated on the opposite side of the target substrate is heated or ablated by a laser pulse that generates gases to propel the component towards a receiving substrate placed in close proximity, 0.5 mm away at the most. The use of a laser for the transfer and placement of discrete components onto a receiving substrate was first reported by Holmes and Saidam [47, 77]. Later, LIFT was applied to the transfer of semiconductor bare dies. Karlitskaya and coworkers have developed a simple model that predicts the fluence threshold for the release of 200 × 200 µm by 150 µm thick Si squares adhesively attached to a sacrificial PVC tape [84]. In a subsequent study [83], the authors described similar experiments for laser transfer of 300 × 300 µm by 130 µm thick Si squares by two distinct mechanisms – ablative and thermal release, using relatively long pulse infrared and green lasers. In a number of publications, Piqué and coworkers have reported LIFT of individual InGaN LED bare dies (250 × 350 µm) using a series of very low fluence UV laser pulses [85] as well as a single-pulse transfer of various electronic components (bare dies and surface-mount electronic components) with sizes ranging from 0.1 to over 6 mm^2 in area [85-87]. Sheats [88] has described a process in which, in order to release the die, the sacrificial layer is heated up to a temperature of 100 – 150°C by optically irradiating it with a dose similar to that used in optical lithography. Although this process does not use a laser, it is very similar in nature to the thermal releasing process described by Karlitskaya *et al* [83].

All these techniques fall in the scope of Laser Induced Forward Transfer, and they were developed with the promise to be a disruptive technology for high-volume assembly of ultra-small and ultra-thin bare dies and components. These bare dies are very fragile and are easily

broken in conventional mechanical manipulation by pick-and-place equipment in high throughput manufacturing [89, 90]. In addition, when the bare dies fall in size below 300 µm per side, stiction effects become a problem because the effect of surface forces such as Van der Waals and electrostatic forces becomes bigger than the gravitational forces exerted on the component at which point pick-and-place operations start to fail [32, 91, 92]. In addition to LIFT, many other approaches have been proposed in order to overcome this problem, most of them still in the R&D stage of progress [89, 93-96].

As mentioned above, Karlitskaya *et al* [83] have proposed and studied two mechanisms of die release–ablative and thermal. Ablative release is a component transfer process using a high-fluence single laser pulse, which evaporates the release material thus creating high pressure and releasing the component at high speed. Thermal release is a less intensive process in which the release material is heated gradually until the material starts to decompose. As a result, adhesion of the component to the release substrate is reduced to zero and it literally drops onto the receiving substrate. Both mechanisms are discussed in detail in the following sections.

2.9.1. Ablative release

Ablative release is achieved by using a single intense laser pulse (approx. 6×10^7 W/cm^2) of either a Q-switched Nd:YAG laser operating at 1064 nm or KrF laser operating at 248 nm. For a wavelength of 1064 nm, the carrier material, a standard white PVC tape, is transparent to the laser light and the silicon is absorbing the laser irradiation under nanosecond pulses. The temperature of the silicon dies increases, which in turn evaporates the adhesive layer and the PVC tape. The gas generated in the confined space between the die and tape does not expand freely. The vapors created are trapped between the carrier and the component and as the gases rapidly expand they propel the component toward the receiving substrate at very high speed.

This mechanism of release has been proven to be highly unstable and unpredictable in placement of the transferred component [97-99]. There are several reasons for that, but the most basic one is the nature of gas dynamics when low-density gases are used to transfer higher density components through a small, confined gap. The process is highly sensitive to initial conditions such as variations in the laser beam profile, irregularities in the sacrificial layer thickness, homogeneity, and presence of contaminants which in turn lead to variations in heat absorption [47, 77]. An additional concern is that the transfer velocities of the components have been shown to reach 10.5 ms^{-1} and can cause damage to the dies upon contact with the receiving substrate [77, 84].

Depending on the type of component being transferred, the sacrificial layer in the ablative releasing method may be configured so that it absorbs or transmits the laser irradiation at the wavelength of the transferring laser. This distinction determines whether absorption on the surface of the component heats the sacrificial layer to the point of vaporization or if the absorption of the laser energy by the sacrificial layer serves as the heating mechanism. When a semiconductor component is transferred with a sacrificial layer that is not absorbing at the laser wavelength, small configuration variations will lead to drastically different heating conditions between subsequent transfers as a result of the nonlinear absorption of semiconductor materials at many wavelengths [83, 84]. However, this effect can be tempered by carefully selecting the laser wavelength used [83].

2.9.2. Thermal release

Thermal release was developed with the intent to address the randomness and instability of ablative release transfer [83]. Under a thermal releasing configuration, the component to be transferred is prepared in the same way as the sample for ablative release. However, the

sacrificial layer behaves in a different manner. In this case, the sacrificial layer is heated slowly with laser fluences significantly lower than those used in an ablative release.

Thermal release has been demonstrated by using special thermal tapes as a carrier material and with low intensity pulses (5×10^4 W/cm^2) of an Nd:YAG laser, operating at 1064 nm wavelength. The PET carrier tape is covered with a special thermal-sensitive adhesive layer, which reacts to temperature increase generated by the laser-heated silicon die. The increase in temperature leads to gas bubble generation that propels the component with relatively low velocities. Like the ablative approach, in most cases, the thermal release still relies upon the laser energy being absorbed by the semiconductor component to be transferred. The resulting process, however, includes a more gradual heating of the sacrificial layer and provides for a less volatile and more predictable transfer process. Transfer velocities were shown to be in the 0.5 ms^{-1} range which ensures not only more precise transfers, but the survivability of functional components after transfer.

In order to decrease the negative effects of the nonlinear absorption that complicates the management of the temperature distribution on the silicon die, and therefore the whole release process, the 1064 nm laser was replaced in a subsequent experiment with a frequency-doubled Nd:YAG laser operating at 532 nm wavelength with lower intensity of 3×10^4 W/cm^2, 0.2 ms pulse duration, and a flat-top beam profile. Karlitskaya reported successful transfers of 300 × 300-μm by 130-μm-thick Si tiles utilizing the thermal releasing process. Allegedly, 95% of these transfers occurred within a release angle of 9°, which corresponds to a placement accuracy of ±35 μm assuming a 195 μm transfer gap is used. Note that these release angles were measured during the free fall of the transferred component, without the presence of a close proximity receiving substrate.

Despite the very good precision results reported by Karlitskaya, no transfers of functional bare dies were demonstrated, at least to my knowledge, and the process still relies upon the laser energy being absorbed by the semiconductor component that is being transferred, which may lead to thermal damage especially for thin dies. In addition, transfer of ultra-thin components (< 50 µm thick) by means of thermal release may prove very challenging as overcoming surface tension forces by gravity alone, on which this process relies upon, may not be possible [83].

2.9.3. Transfer conditions and dynamics

2.9.3.1. Threshold fluence. The experimental results reported in the literature for the threshold fluence E_T (defined as the minimum fluence required for die release) vary substantially and have values between 100 mJ/cm^2 (KrF laser) and several thousand mJ/cm^2 (Nd:YAG laser for example) [72, 77, 83, 84]. The reason behind this is that the threshold value of the fluence depends strongly on the laser wavelength and absorption mechanism. The substantial difference between the KrF and Nd:YAG lasers should be expected since the absorption at the deep UV range is much higher than in the infrared and visible light ranges.

2.9.3.2. Release velocity. Holmes and Saidam discovered that a reliable transfer in ablative release occurred only when the proximity gap was less than the device height, with large and apparently random lateral displacements [47, 77]. They conducted experiments to establish the typical values for the initial velocities of microstructures released from polymer sacrificial layers in ablation release experiments. They concluded that further work is required to determine the effects of fluence, beam homogeneity, and ambient pressure on the placement accuracy of the process. Figure 33 shows the measured variation of initial velocity with laser fluence for structures with 100 µm thickness. They offered the following simple equation to predict the initial velocity:

$$V_r = (2\eta \frac{E-E_T}{m})^{\frac{1}{2}} \qquad \text{(Equation 6.1.)}$$

where Vr is the release velocity, ms^{-1}, η is the energy conversion efficiency, %, m is the mass per unit area of the released component, g/cm^2, and E is the laser fluence, mJ/cm^2. In Equation 6.1., the assumption is that only the excess fluence above the ablation threshold E_T can contribute to impulse coupling. As the authors pointed out, this is consistent with thermal coupling measurements reported by Dyer and Sidhu [100], which indicated that the thermal load on a polyimide target remains roughly constant above the ablation threshold.

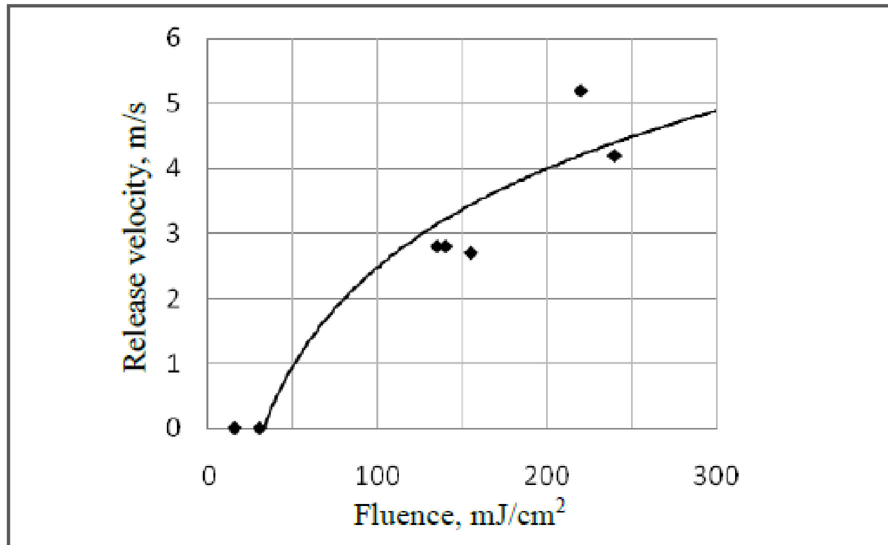

Figure 33. Measured variation in release velocity vs. laser fluence for 100 μm thick Ni structures by ablative release using a single pulse from a 248 nm KrF laser; solid line is the predicted from equation 1 [77].

Holmes and Saidam further speculated that the results can be extrapolated to thinner components by assuming that the conversion efficiency depends only on fluence, thus concluding that the initial velocity should be inversely proportional to the square root of the

component thickness δ. For example, at E = 100 mJ/cm^2 they expected the initial velocity to vary from around 2 ms^{-1} at δ = 100 µm to 20 ms^{-1} at δ = 1 µm.

The release speeds in ablation releasing reported by Karlitskaya *et al* [84] was in the same order of magnitude but the fluence was much higher. They reported 12.2 ms^{-1} release speed for a 200×200 µm by 150-µm thick silicon square, released by a single pulse with fluence of 4500 mJ/cm^2 from an 1064 nm Nd:YAG laser. In another experiment [83], the same authors reported release velocities from 1.3 to 10.5 ms^{-1} for a 300×300 µm by 130-µm thick silicon square, released by a single pulse from a Q-switched 1064 nm Nd:YAG laser with fluences varying from about 3000 to 9000 mJ/cm^2. It is seen in Figure 34 that Equation 1 holds for these experiments too.

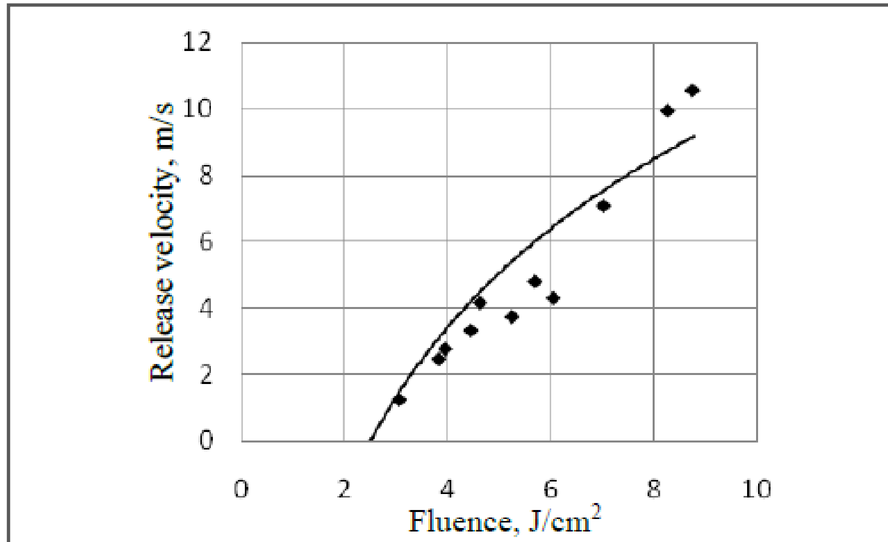

Figure 34. Measured variation in release velocity vs. laser fluence for 130 µm thick Si structures by ablative release using a single pulse from a Q-switched 1064 nm Nd:YAG laser; solid line is the predicted from equation 1 [83].

The release speeds measure by Karlitsakya and reported for 300×300 μm by 130-μm thick silicon squares in the thermal release experiments are one or two orders of magnitude smaller, varying from 0.1 to 0.9 ms^{-1}, without showing a significant dependence on the incident fluence [83].

2.9.3.3. Component survivability. One very important question Holmes and Saidam [77] studied is whether the kinetic energy generated on laser release can be dissipated without damage to the released component when it impacts the receiving substrate. They offered an estimate for the strain in the component upon impact that suggested that in developing the process one should look for ways to reduce the initial velocities from their current values to avoid the mechanical damage of the component. Their conclusion was that the LIFT process can be relatively violent. For example, they found that for small nickel pads (2×2 mm, 100 μm thick) released from fused silica carriers with polyimide sacrificial layers, the minimum practical release velocity with a KrF excimer laser pulse was of the order of 1 ms^{-1} [47]. Interestingly, other researchers have succeeded in transferring much more delicate and fragile components. For example, Piqué and coworkers [101] have successfully transferred intact (no cracks or fractures) ultrathin 1 mm × 0.75 mm by 10 μm thick Si components, using an excimer laser in ablative releasing mode.

2.9.3.4. Placement precision and accuracy. Karlitskaya *et al* [83] pointed out that for the LIFT process to be capable of replacing the conventional pick-and-place method, the component placement accuracy should be very high, within ±35 μm deviation from the "ideal" position. They pointed out that the problems associated with the position precision are inherent to this process in which a relatively low density gas pushes a higher density object. They suggested that the drive instability can be mitigated by controlling the release velocity. The

lower release velocities are more likely to result in a better position precision and the risk of mechanical damage is lower. For example, in the ablation releasing experiments with a high-intensity pulse and release speeds of up to 10.5 ms^{-1}, the die was tumbling and rotating during the releasing process. The direction was random with a large initial angle. This angle was responsible for the lack of accuracy in the component placement on the receiving surface. These conclusions agree well with similar results reported by Holmes and Saidam [47, 77]. By contrast, in the thermal releasing experiments with a green laser (532 nm) where the release speed was more than ten times smaller tumbling was minimal and the release angle was about $\pm 4^{o}$ that allowed placement of the components within ±35 μm accuracy over a gap of 0.5 mm [83].

The component size in these release mechanisms also matters. Piqué *et al* [101] have observed rotating or tumbling of the transferred devices with the degree of rotation increasing between the smaller footprint devices to that of the larger one. Karlitskaya *et al* [83] stressed also the importance of achieving a uniform energy distribution in the laser beam profile without large peaks. They found a strong correlation between the spatial energy profile of the light spot and the releasing behavior of the component, and from there, the precision of placement.

It is obvious from the discussion so far that the two major problems that plague the existing LIFT techniques are precision and accuracy and component survivability. Both of these problems are dependent on the mode of release used. The ablative release process is inherently unstable and directs the components randomly and at the same time quite violently leading to component damage. The thermal releasing process is gentler, more homogeneous and characterized with a higher positioning precision, but it is generally slower than the ablative process and not suitable for very small and thin components as it relies heavily on gravity effects for transfer.

In order to increase the precision and accuracy of LIFT and to reduce component damage the process parameters such as wavelength, pulse duration, fluence, beam homogeneity, and transferred material properties need to be carefully selected and controlled. In addition, the uniformity of the adhesive releasing layer thickness and material composition are essential for the overall placement control. Finally, the gap between the releasing and receiving substrates must be kept as small as possible. The arguments here are based on the simple geometry – the deviation ϵ_{xy} from the "ideal" placement position is a function of the gap δ and the releasing angle θ and is equal to:

$$\epsilon_{xy} = \delta \tan\theta \quad \text{(Equation 6.2.)}$$

CHAPTER 3. THERMO-MECHANICAL RELEASE (*tm*SLADT)

The Thermo-Mechanical Selective Laser Assisted or *tm*SLADT (pronounced 'T' – 'M' – 'SLAD') process was developed by our team at the Center for Nanoscale Science and Engineering at North Dakota State University with the idea to address the major problem that existing LIFT techniques faced at the time, accuracy and precision of placement with no damage sustained by the active component during transfer. Considering these, the ultimate LIFT technique needs to address the following five points:

1) Ability to place smaller and thinner components than what is possible with the best pick-and-place machines.
2) Transfer components at predetermined, exact locations with a desired orientation.
3) Transfer conditions should not exceed the components thermal damage threshold.
4) Acceleration and deceleration energies need to be well below what would cause functional damage.
5) Throughput required for high volume manufacturing.

From everything reported in the literature on Laser Induced Forward Transfer one can certainly draw the conclusion that the success of a LIFT technique depends greatly on the sacrificial layer that bonds what needs to be transferred to the carrier substrate. This sacrificial layer for the purposes of *tm*SLADT is referred to as the Dynamic Release Layer (DRL). In all LIFT techniques reported earlier, the process causes a complete or at least partial evaporation of the DRL with all gas-dynamics problems discussed earlier. The problems described can be lessened if the transferred component can be insulated from the rapidly expanding plume of gases. That separation will create a blister in the DRL material which in turn can act as a "mechanical" actuator in the transfer process. This approach, first reported by V. Marinov and

coworkers in 2012 [102] and known as *tm*SLADT, used an in-house developed sacrificial material to create blisters in a single-layer DRL. The energy of the laser pulses is absorbed by a shallow region of the DRL known as the absorption depth creating a constrained volume of rapidly expanding gasses, but leaving the rest of the DRL intact. The increase of the volume of the evaporated material creates stress in the surrounding DRL layer leading to plastic deformation and the creation of a blister in the sacrificial layer, which acts as a mechanical actuator and pushes the die toward the receiving substrate. Since the gasses formed are fully enclosed by the blister, the uncertain environment experienced during ablative release is avoided while removing the non-linear absorption effects presented by semiconductor materials.

Using a single layer DRL creates challenges by itself. A single-layer DRL proves very sensitive to three properties that need to be tightly controlled. These properties are laser light absorption, elastic properties at elevated temperatures, and static and dynamic adhesive properties [102]. In order to reduce the number of requirements placed on one layer of material in a single-layer DRL, the team adopted the two-layer DRL in which the material adjacent to the glass carrier provides the laser absorption, leading to blistering mechanical actuation by gas confinement, while the second layer, adjacent to the structures to be transferred provides the adhesive properties. A similar approach has also been used by a research group at the University of Princeton lead by Kattamis that applied the process for the purposes of ink printing [103]. In our application such a configuration allows varying the adhesive properties independently of the absorbing and elastic ones. More information about blister formation and challenges can be found in [102]. The two-layer DRL configuration and action are shown in Figure 35.

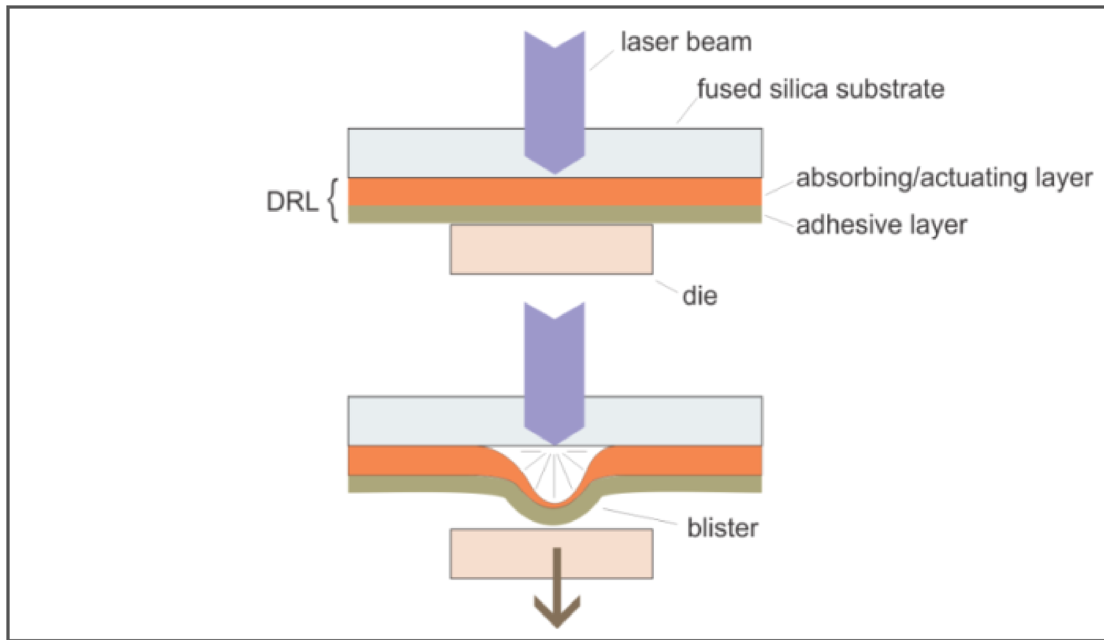

Figure 35. *tm*SLADT with a two layer configuration blister formation and component release [104].

The DRL comprises both a blistering layer and an adhesive layer. During the process of laser transfer, the DRL is irradiated by a laser pulse through the laser-transparent carrier. In contrast to the other laser-induced forward transfer mechanisms, *tm*SLADT does not rely on the kinetic energy of a plume of vaporized material (ablative laser propulsion) from the DRL or solely on the gravitational force (thermal laser transfer) to place the dies. Instead, the laser pulse creates a blister in the DRL, thus confining the vaporized material within the blister (Figure 35). The DRL, with a blistering layer that is thicker than the laser absorption depth of the material, is subjected to only a limited non-penetrating ablation and forms a blister that does not rupture during the process. The force exerted by the blister, in addition to the gravitational force on the die, initiates the transfer over the gap [40, 102, 104].

The original LIFT concept uses a jet of gas to complete a component transfer. By the nature of gas dynamics, the use of a relatively low density gas to push a higher density

component, such as a semiconductor die or metal part, results in a highly sensitive to initial conditions process. Any variations in the heat absorption mechanism, irregularities in the sacrificial layer thickness and/or homogeneity, presence of contaminants, and deviations in the intensity profile of the laser beam make previous LIFT based processes reported very unstable and highly unpredictable. In contrast, the blisters created by the confined ablation in *tm*SLADT act as mechanical actuators, providing much better control of die placement and more repeatable and precise die transfers. This capability, unmatched by the other LIFT-based techniques, facilitated the demonstration in 2011 of the world's first successful application of lasers for the fabrication of a functional device (an RFID tag) based on a COTS 65-µm thick, 670-µm square bare die [105]. The same method also was used for the successful laser manipulation of silicon bare dies with sizes as small as 250 µm square and 18-µm thick (Figure 36).

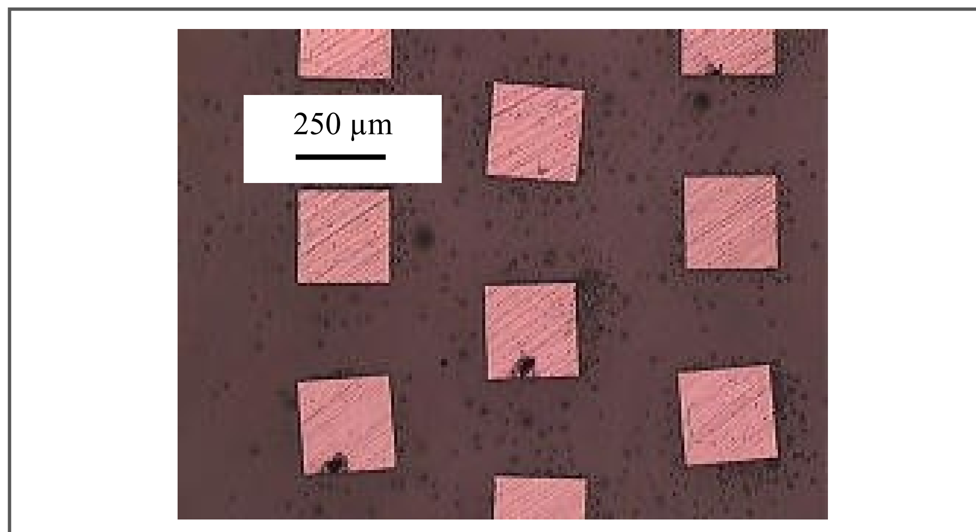

Figure 36. Laser-transferred 18 to 20µm thick, 250µm square silicon dies transferred using *tm*SLADT and shown on the receiving substrate.

3.1. Laser Enabled Advanced Packaging (LEAP) for Ultrathin Dies in Flexible Substrates

The principles of *tm*SLADT were employed in the development of a comprehensive silicon wafer to finished electronic product process known as Laser Enabled Advanced Packaging (LEAP). LEAP was conceived from the very beginning as a low-cost, high-throughput, contactless assembly of ultrathin bare dies (< 50 μm) onto flexible and rigid substrates. These capabilities would allow using LEAP for applications varying from ultra-low cost disposable electronic devices such as RFID tags, through new application areas such as RFID-enabled paper for financial and document security, to the assembly of electronic components of MEMS.

Achieving these goals required addressing not only the immediate need for high-throughput packaging technology, but also the problems associated with processing silicon wafers and individual dies with thicknesses less than or equal to 50 μm. The difficulties of handling and processing the very fragile ultrathin silicon can be minimized if some of the operations are consolidated thus reducing the times the ultrathin wafer is transferred from one carrier to another before the component placement step. This minimalistic approach to the major operations in the beginning of the back-end processing sequence illustrated in Figure 37 includes challenges associated with:

1) Thinning of silicon wafers (as received) to thicknesses below the capability of current mechanical back-grinding operations.
2) Dicing of wafers into individual dies when their thickness falls below the limits of conventional dicing saws, at which point they start to introduce excessive mechanical

damage to the electronic components leading to yield loss and in some cases complete wafer loss.

3) Attaching thinned wafers to carrier substrates with sacrificial layers suitable for laser induced forward transfer assembly operations such as *tm*SLADT.

4) Precise and accurate placement of the ultrathin and ultra-small dies at exact predetermined locations.

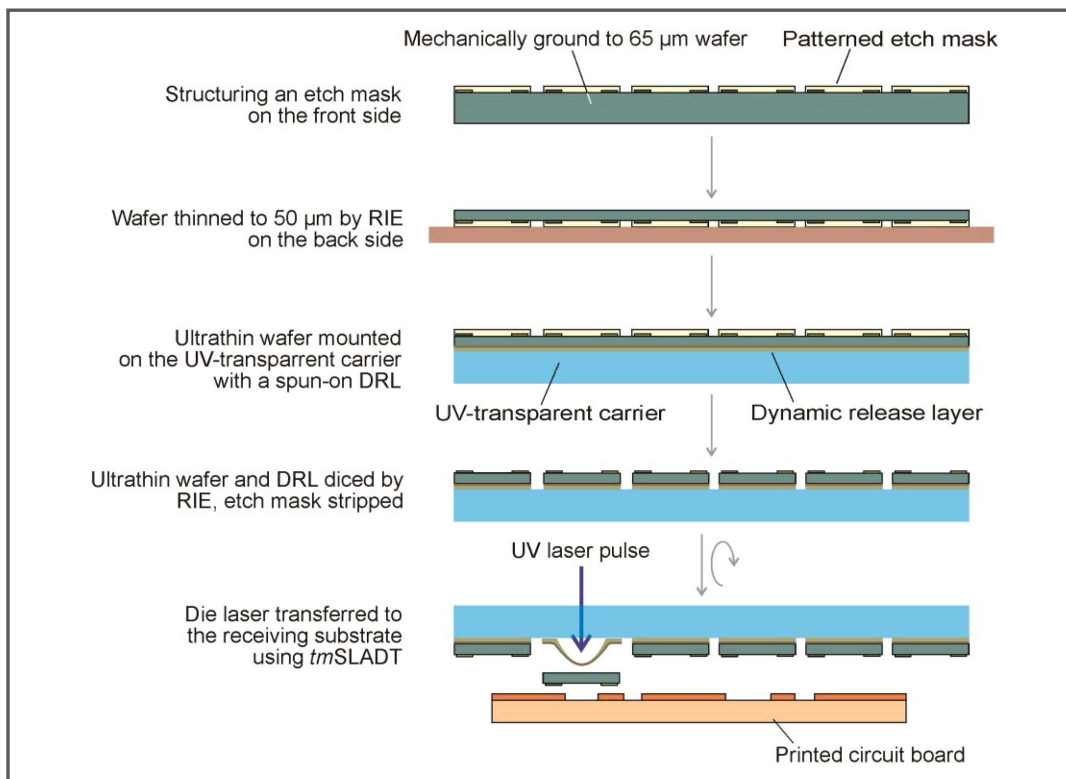

Figure 37. Process sequence in the Laser Enabled Advanced Packaging [105].

The following sections explain in detail the steps in this process, which has been successfully applied to fabricate a prototype passive RFID tag in paper substrate with an embedded ultrathin RFID [40].

3.1.1. Wafer thinning

Developing LEAP as a comprehensive starting wafer to finished product technology meant that all steps included in the process needed to be addressed, not only the laser propulsion technology. Currently, there are technologies that can produce very thin chips, such as silicon on insulator, but they are expensive and somewhat specific. When the process starts with regular Si wafers, the issues of wafer thinning and dicing also need to be addressed.

Regular silicon wafers are fabricated by slicing a silicon ingot into wafers with thicknesses ranging from 0.3 to 1 mm, depending on the final wafer diameter. This is followed by coarse-grit and fine-grit mechanical grinding. Forming high-density integrated circuits is not possible without having a substrate surface layer free of damaging crystalline defects (also called the denuded zone). Mechanical grinding damage in the Si wafers has been investigated by many researchers (see, for example, Ref. [90, 106-110]). There are studies that offer evidence for an intricate arrangement of 1 to 2 μm deep surface cracks oriented parallel to the <111> plane in silicon wafers after mechanical grinding [108] as well as indication of warpage in the wafers due to stress induced by backgrinding. It has been shown that the stress can be mitigated by dry etching [106]. Other techniques that remove the structurally damaged layers and residual stresses and can provide surfaces with exceptional flatness and mirror-like finish include wet chemical etching and chemical mechanical polishing (CMP). After these finishing steps wafer thicknesses range between 275 μm for 50 mm (2 inch) diameter wafers and 775 μm for a typical high-volume 200 mm (8 inch) wafer.

Obtaining ultrathin dies after the circuitry has already been formed requires additional wafer thinning at the back end. Currently mechanical grinding can achieve thickness in the vicinity of 50 μm, albeit with low precision and thickness uniformity across the wafer; typical

values for a 200 mm (8 inch) wafer are thickness of 50 µm with tolerance and uniformity of ± 12 µm. Going below the 50 µm mark requires the use of the finishing methods mentioned above. Reactive Ion Etching (RIE) has been demonstrated as a method to reduce wafer thickness to 10 µm [111]. Other methods for obtaining ultrathin wafers are discussed in detail in Refs. ([93, 112]).

3.1.2. Wafer dicing

Wafer dicing using a diamond-coated circular saw is not appropriate when wafer thickness falls below about 65 µm because of problems with damage such as chipping and cracking. Dicing of these ultrathin wafers requires alternative approaches such as laser dicing or plasma etching. The advantage of laser dicing is that it introduces minimal stress and structural damage in an ultrathin wafer due to the small heat affected zone. In addition, street width in wafers prepared for conventional dicing methods is usually bigger than the laser kerf. However, laser dicing has a problem with debris produced during cutting that may be deposited onto the die bumps, affecting the reliability (Figure 38 a, b).

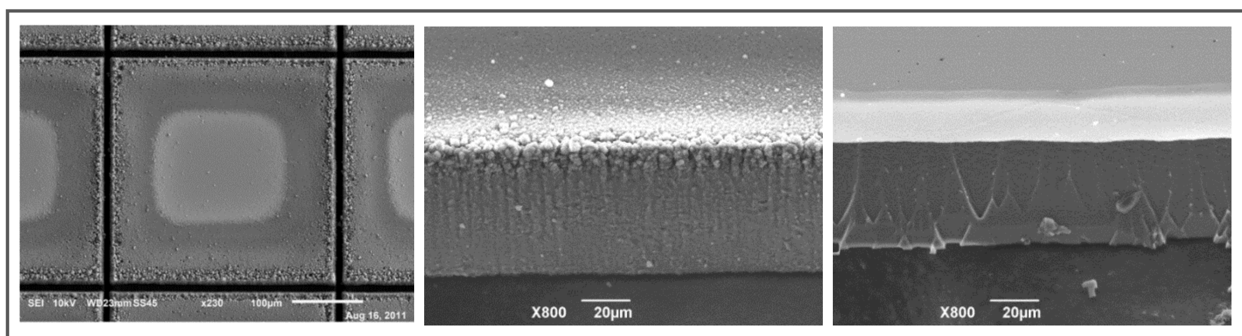

Figure 38. An SEM picture of a part of silicon wafer after laser dicing, showing the accumulation of debris around the 20-µm wide streets (*left*); a close-up view of a street ablated using a Nd:YVO4 HIPPO laser (*center*); a close-up view of an RIE-etched street (*right*) [104].

Plasma etching, on the other hand, eliminates most of the problems with the traditional and laser dicing. Figure 30c shows an SEM of a sidewall RIE-etched die with no evidence of mechanical damage or debris re-deposition. The edge of the die is much cleaner and well-defined. Disadvantages of RIE dicing include a relatively low material removal rate, difficulty in controlling thickness uniformity and flatness, and possible increased surface roughness. However, there is evidence that RIE thinning and dicing remove microcracks from previous mechanical grinding operations and reduce the stress concentrations in the material, resulting in increased fracture strength [113].

Another issue with manipulating ultrathin Si substrates is wafer handling during back-end processing. Methods for thick wafer handling where wafers are transferred, bonded, and deboned on various rigid and flexible carrier substrates cannot be directly applied to ultrathin wafers. The latter are very fragile and tend to warp and sag due to gravity effects, making the use of automated robot handling difficult if possible at all [114]. Ultrathin wafer processing requires solutions to reduce the number of transfers between handle carriers in order to increase reliability and throughput and to provide lower production cost. One such unorthodox solution is a process called "Dicing-Before-Grinding" or "Dicing-By-Thinning" in which a partial cut is carried out on the front side of the wafer before bonding to a temporary carrier [89, 112, 115-117]. After bonding the partially diced wafer is thinned on the opposite side until streets are opened and the dies separated.

3.1.3. Dynamic release layer (DRL) preparation

Sample preparation for *tm*SLADT starts with a laser transparent carrier. The one used in all of our experiments is a 3"×1/16" fused silica disk from Chemglass Life Sciences (CGQ-0600-10). The two-layer DRL consists of a blister forming layer which is a spin-on polyimide from

HD Microsystems (PI-2525), followed by an adhesive layer of low molecular weight polyester, formulated in house and designated as PE7. The structure of this material, which is based on fatty dimer diacid and biodiesel, is shown in Figure 39.

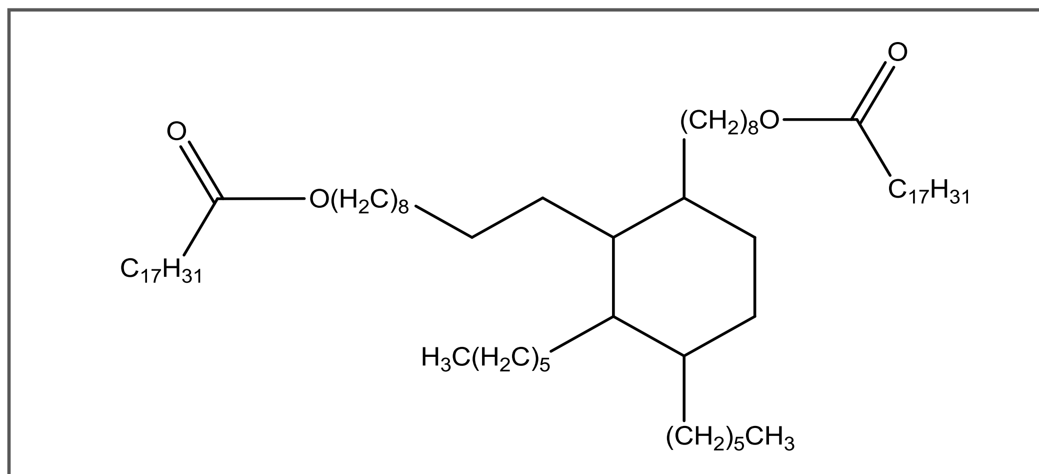

Figure 39. Chemical structure diagram of the PE7 polymer adhesive material [104].

PE7 was synthesized by charging dimer fatty acid (Croda Polymer & Coatings) (0.01 mol, 5.70 g), soy biodiesel (Cargill Inc.) (0.02 mol, 5.54 g), dibutyltin dilaurate (Sigma-Aldrich) (0.05 g), and xylene (20 ml) into a three-necked, round-bottomed flask equipped with a magnetic stirrer, a Dean-Stark trap with a condenser, and a gas inlet and outlet. The mixture was heated to 160 °C for 3 hours under nitrogen atmosphere. Xylene and water were removed from the system by distillation. The mixture was then heated to 230 °C for 5 hours to obtain a yellow, viscous liquid of PE7, with a yield of about 97%. For use in the DRL, PE7 was further diluted in tetrahydrofuran (THF) to concentrations of 5%, 10%, and 25% by weight.

The sample carrier is prepared by spin coating the DRL materials on the fused silica disc using a SUSS RC-8 spin coater. The fused silica disks are first cleaned using THF and dried by spinning. The spin coating of the PI-2525 polyimide layer is carried out as follows:

1) Static dispense on at substrate center and relaxation of the material for 60 seconds before spinning.
2) Initial spin at 500 rpm for 10 s at acceleration of 500 rpm/min.
3) Final spin at 5000 rpm for 40 s at acceleration of 1000 rpm/min.

In the next step the PI-2525 layer is cured in a polyimide curing oven under a nitrogen atmosphere in the following sequence:

1) Ramp up to 120°C and hold at that temperature for 30 minutes.
2) Ramp to 350°C and hold for 30 minutes.
3) Cool down gradually to 50° C or less before exposing to room temperature.

This cycle results in an incomplete crosslinking of the PI-2525 polyimide, which proved to work best in the laser transfer experiments. The thickness of the polyimide film obtained with these spin-coating and curing parameters was 4 μm, which agrees well with the spin curves provided by the material manufacturer. The PE7 material was also dispensed on a static substrate, but unlike the polyimide, the whole fused-silica disc was coated with the starting material prior to spinning. Parameters used for spin coating were:

1) Initial spin for 5 seconds at 500 rpm and acceleration of 500 rpm/min.
2) Final spin for 40 seconds at 4500 rpm and acceleration 1000 rpm/min.

The THF solvent evaporates during spin coating leaving varying amounts of PE7 deposited depending on the PE7/THF concentration used. For 5% PE7 concentration in THF the polyester layer thickness is around 1 μm.

3.2. Wafer and Sample Preparation Steps for LEAP Experiments

The following sections outline in more detail the sample preparation and laser transfer steps in the primary LEAP experiments.

3.2.1. Sample thinning

P-type Si <100> wafers were procured and used in the initial experiments. First they were mechanically ground to a 65 µm thickness. Next, the front side of the wafer was sputtered with a 0.8 µm thick Cu layer, preceded by a 30 nm thick layer of Ti for improved adhesion. The metal deposited was patterned using standard lithographic techniques into squares with 350, 670, and 1000 µm sides to define dies with corresponding dimensions. The Cu and Ti layers in the streets were then etched away to expose the Si wafer in the streets. Since the objective of this work was to study the laser transfer process parameters, blank silicon tiles without circuitry were used instead of functional dies. One would not expect the transfer dynamics of a functional silicon-based IC to differ significantly from a silicon tile with the same or nearly the same dimensions. When the method described here is used for assembly of functional devices, sputtering and patterning metal films onto the front side of the wafer will not be permissible. In this case, the street pattern can be defined by structuring a photoresist layer with a photolithographic process and then using the photoresist as an etch mask.

After etching of the metal layers, the wafers were rinsed and dried and then placed Cu-side down in a Trion Phantom II RIE Plasma Etcher to be thinned down to 50 µm. As discussed above, RIE thinning removes any structural damage caused by mechanical grinding. The parameters used for both wafer thinning and opening the streets in the next step are shown in Table 3.

Table 3. RIE parameters used for thinning and dicing of Si wafers

RIE process for:	Pressure, mTorr	Power, W	Base Pressure, mTorr	SF_6, sccm	Resulting Etch	Etch Rate, µm/min
Thinning	300	100	100	26	Isotropic	0.85
Dicing	100	300	100	26	Anisotropic	1.5

The measured etch rate resulting from these parameters was 0.85 µm/min for thinning and 1.5 µm/min for street opening. The wafer thickness was measured using a contact profilometer (KLA Tencor P-11) on a separate control piece of Si wafer placed in the etcher adjacent to the processed wafer.

After the thinning the wafer was manually attached to the DRL spin-coated on a laser transparent fused silica carrier using plastic tweezers. The as-prepared stack was run through an Optec DPL-24 Laminator to ensure reproducible and evenly distributed bonding pressure between the DRL and the wafer. Lamination was carried out as follows:

1) Dwelling in vacuum for 7 minutes.
2) Pressurizing the chamber.
3) Dwelling for additional 3 minutes.

The pressure of the laminator used is set at 30 psi and is non-adjustable.

3.2.2. Sample dicing

After the wafer was bonded to the DRL, it was singulated into individual dies. This was performed utilizing two methods, RIE as discussed above, and laser ablation, thus allowing their respective results to be compared.

The RIE process involved opening the exposed streets using the RIE parameters in Table 3. Half of the sample was protected by a glass slide in order to leave a wafer area for laser singulation and comparison experiments between the RIE-etched and laser singulated dies.

A Spectra Physics HIPPO Nd:YVO_4 laser operating at 355 nm was used for dicing the other half of the wafer along the wafer streets. The laser was set to a 50 kHz repetition rate, and used at an average power of 3 W, with pulse energy of approximately 60 µJ. Utilizing a scan speed of 400 mm/s, 20 scans were required to singulate the 50 µm thick wafer.

After laser singulation was completed, the sample was inspected utilizing a backlit optical microscope to ensure complete dicing was achieved. In some cases, nearly complete dicing occurred while small tabs of Si remained intact across the diced streets, which inhibited the transfer process. The desire for full separation must be balanced with the harmful effects of over-scanning during dicing, as laser scanning much beyond that necessary to singulate the wafer affects the properties of the DRL and must be monitored.

3.2.3. Laser transfer

After dicing, the wafer with the fused silica carrier (releasing substrate) was mounted in a fixture used for laser transfer. The releasing substrate was placed on top of the receiving substrate with the DRL and singulated wafer facing down. Prior to mounting, the receiving substrate was spin coated with a pressure sensitive adhesive (PSA) in order to provide a means for catching the transferred dies. Shims of 260 µm thickness were used to space the receiving and releasing substrates from each other. Since the average thickness of the wafer used in these samples was 65 µm, the transfer gap was about 195 µm. In a typical electronics packaging application, the receiving substrates would include rigid or flexible printed circuit boards, or

other substrates, that provide a means for interconnecting the transferred dies to the rest of the circuitry.

Once the substrates were mounted, the fixture was positioned under the Scanlab HurryScan II laser scanhead of the Spectra Physics HIPPO Nd:YVO_4 laser for transfer (more details about the laser system are available in Chapter 9). The laser parameters used for activating the DRL are critical to optimize the transfer rate, and minimize the lateral or rotational displacement of the die during transfer. Operating with pulse energies just below the rupture threshold of the configured transfer setup ensures maximum blister height while still containing the hot gas generated by the vaporized blistering layer material.

The laser transfers were accomplished by scanning the DRL beneath the die to be transferred with a circular laser scanning pattern at 15 kHz repetition rate and a scan speed of 300 mm/s appropriate to create a continuous blister, which was based on the results of previous work [102]. For this study, a series of three concentric circles was used with diameters of 200, 400, and 600 μm for a 670×670 μm die size. The pattern starts with the smallest circle first, and works its way outward with a line connecting each circle. This pattern can be seen in Figure 43.

The third harmonic mode of the laser at 355 nm was used, which is absorbed within a 0.2 to 0.5 μm depth in the typically 4 μm thick polyimide layer of the DRL. The beam was focused to a spot size of less than 20 μm in diameter. Many transfer trials were needed to determine the laser settings needed to optimize the die transfer rate, precision, and accuracy. The power needed to transfer depends greatly on the DRL characteristics, namely, the thickness and elastic modulus of the polyimide layer, the adhesion strength of the adhesion layer, and the die thickness (die mass). The average power of the laser was varied from approximately 50 mW to 400 mW during the trials. The lowest power did not activate the blister sufficiently to overcome the adhesion of

the die to the DRL. The highest power caused complete rupture of the blister, which often caused extreme displacements. Average power settings of 150-250 mW provided the best results for this DRL, adhesive layer formulation, and die thickness. These parameters resulted in pulse energies ranging from 10 to 17 μJ/pulse, which were usually low enough to avoid bursting the blister material. In some cases though, rupturing of the blister did occur. However, it was not clear if the rupturing occurred because of the excessive laser energy or because the die took away small pieces of the DRL upon transfer. Figure 40 illustrates a typical result from the laser transfer process, showing a series of dies which have been transferred in a checkered pattern onto a receiving substrate.

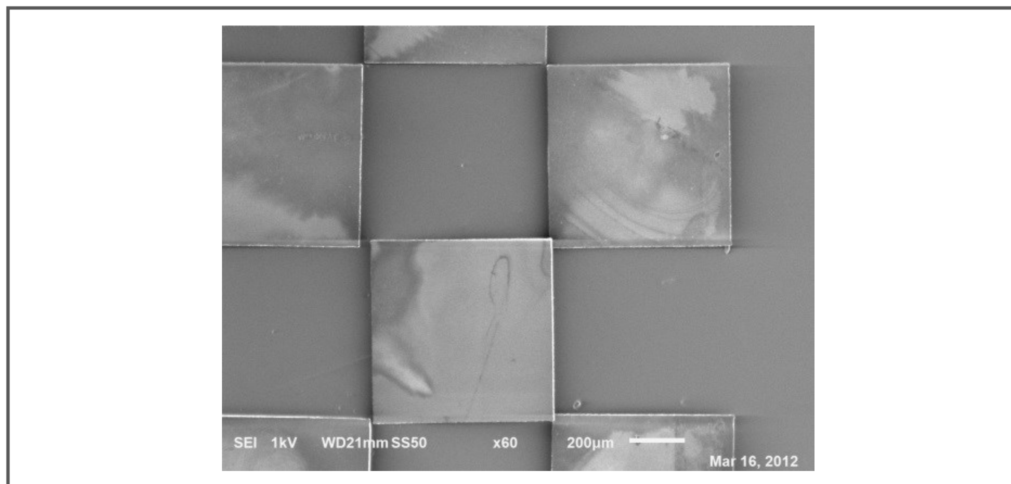

Figure 40. SEM image of 670×670 μm, 50 μm thick laser-cut Si dies on the receiving substrate after transfer. The transfer was initiated by scanning three concentric circles while focused on the DRL as seen in Figure 43. The average power of the laser was 200 mW [104].

3.3. Summary

The LEAP release process summarized here and presented in detail elsewhere [40, 102, 104, 105] is unique in its ability to support high-volume assembly of ultrathin semiconductor

bare dies, beneficial in manufacturing the next generation of mass produced high-density miniature electronic devices like the new class of ultra-low-cost disposable and green electronic products packaged on flexible, biodegradable substrates and augmented with RFID technology. The experimental results obtained demonstrate the remarkable transfer precision and accuracy of *tm*SLADT, which are compatible with the capabilities of the conventional die placement methods. Precision and accuracy depend mostly on the nature of the transfer process as shown by the changes from thermo-mechanical to ablative release mechanism that allow the blisters to rupture, resulting in significant deterioration of both the placement precision and placement accuracy.

The viability of the LEAP process for packaging of ultrathin and ultra-small semiconductor dies, including 18-20 μm thick, 250 × 250 μm dies, embedded in flexible substrates have already been demonstrated and applied in EPC Global Gen2 UHF RFID-enabled "banknotes" to exemplify the application of this technology [40, 105]. Initial reliability tests presented in [40] showed no reduction in device performance after repeated bending stresses and environmental testing. The process model presented verifies LEAP as a low-cost approach for packaging ultra-small, ultrathin dies.

The next logical step in developing LEAP and *tm*SLADT as enabling technologies for MEMS fabrication is to verify the methods for release of materials other than silicon and the assembly of simple structures that can be applied in a technology demonstrator. The final goal is to develop LEAP as an enabling technology for assembly of both the mechanical and electrical components of complete, functional MEMS. The results from this work are presented in the next chapters.

CHAPTER 4. LASER-ASSISTED ADVANCED ASSEMBLY (LA^3) FOR MEMS FABRICATION

As discussed previously, currently MEMS fabrication is based on methods originally designed and developed for manufacturing of semiconductor devices. Using these techniques the entire MEMS device is built component by component without any or, at the most, minimum usually monolithic, assembly. Using a relatively well understood and mature, established technology has some advantages like respectable reliability and reduced per-device cost. However, the inherent limitations of this approach narrow the choice of materials that can be employed, therefore reducing the complexity of MEMS design and, as a result, impose limitations on their functionality. In addition, the existing technology is expensive and complicated and more importantly does not allow using material treatment methods to enhance the properties of the constituents. Even more critical for the advancement of the MEMS technology are the limitations of the currently used methods for MEMS assembly, most of which are derived from the methods used in the macro-scale and, in general, lack the capabilities to efficiently and at a high rate handle the ultra-small MEMS components.

The proposed method solves the existing problems by using a hybrid fabrication approach in which the MEMS components are first fabricated on discrete substrates and then assembled to build the system. Components can be micro-machined on a separate substrate out of any stock material available in the form of a thin sheet by using a laser, photolithography followed by wet/dry etching, or any of the other subtractive methodologies presented earlier, as well as by many available additive deposition techniques. This would allow utilizing a wider range of materials, including biocompatible metals such as stainless steel, titanium and cobalt alloys, ceramics, polymers, composites, semiconductors, and materials with special properties

such as memory shape alloys, thermoelectric, ferromagnetic, piezoelectric, electrostrictive alloys, and more. In addition, such a hybrid process will permit the application of material treatments to the starting materials such as surface and volumetric heat treatment operations, tribological and biocompatible coatings, surface modifications, bio-functionalization, and more, prior to component fabrication, for enhancing their structural and mechanical properties, a possibility which is very limited or not available with the current methods.

To build the MEMS, the components are transferred to the substrate for assembly using the low-cost, high-production-rate thermo-mechanical Selective Laser-Assisted Die Transfer (*tm*SLADT) mechanism for microchips assembly, already successfully demonstrated by our team and explained in details in Chapter 7. Therefore, not only the mechanical but also the electronic parts of the MEMS can be fabricated using the same equipment and method. The proposed method will allow increasing the design complexity of MEMS by using components fabricated with a wide variety of materials and shapes otherwise unattainable with the current technologies. The Laser-Assisted Advanced Assembly (LA^3) technology for MEMS fabrication and assembly is schematically shown in Figure 41. The separate components of the device are fabricated on discrete substrates which are placed under the laser beam on an as needed basis, aligned, and the individual parts are transferred for assembly. Although the process as described is sequential, the actual laser transfer step is accomplished in a manner of microseconds. By using an appropriate process and device design that minimizes substrate handling, replacement, and alignment steps, the method could possibly approach parallel assembly rapidity. Another advantage of sequential assembly in this case is the option to omit the transfer of damaged components which would increase device yield, especially for systems that require a large

number of components. Additionally, re-work of components is possible outside the process sequence if needed.

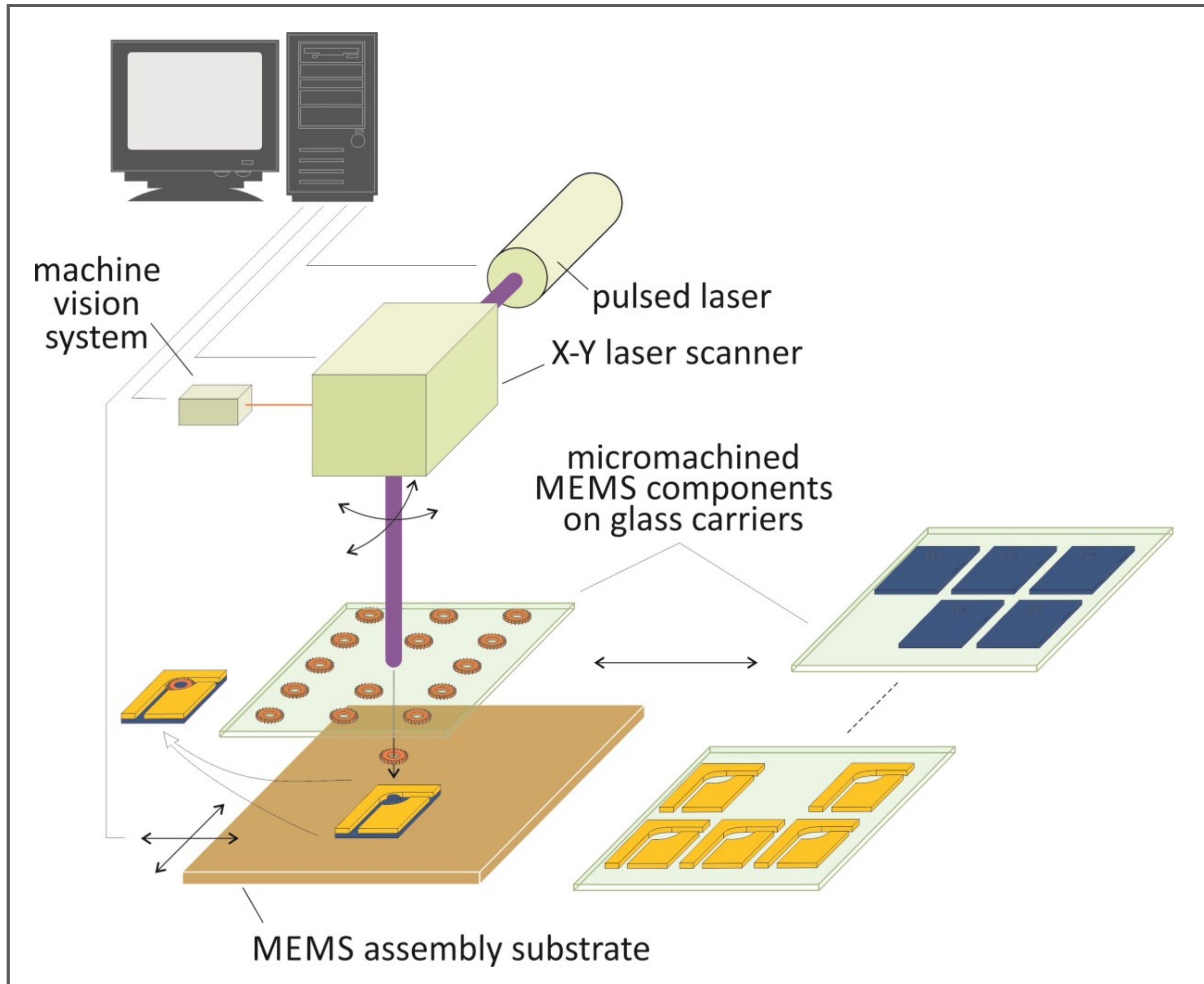

Figure 41. Schematic of Laser-Assisted Advance Assembly (LA^3) process for hybrid assembly.

The major steps of MEMS component fabrication and assembly using the LA^3 process are schematically shown in Figure 42. In brief, the processing sequence starts with a desired material available in thin sheet form in this case, which is bonded onto the already fabricated dynamic release layer (DRL) on the UV-transparent glass carrier. The DRL fabrication was

already described in detail previously. Next, components are micro machined using a laser as shown or alternatively, by using photolithography or other methods. At this point the carrier substrate holding the components is ready for transfer by the thermo-mechanical selective laser-assisted transfer method (*tm*SLADT). In preceding steps the receiving substrate is prepared in a similar manner by micromachining and/or assembly of other parts of the MEMS device. The UV-transparent carrier is flipped, positioned, and aligned between the laser beam and receiving substrate and irradiated sequentially to place the next component onto the device. The process as shown will allow putting together parts in z-direction only (stacking) so appropriate design considerations need to be observed.

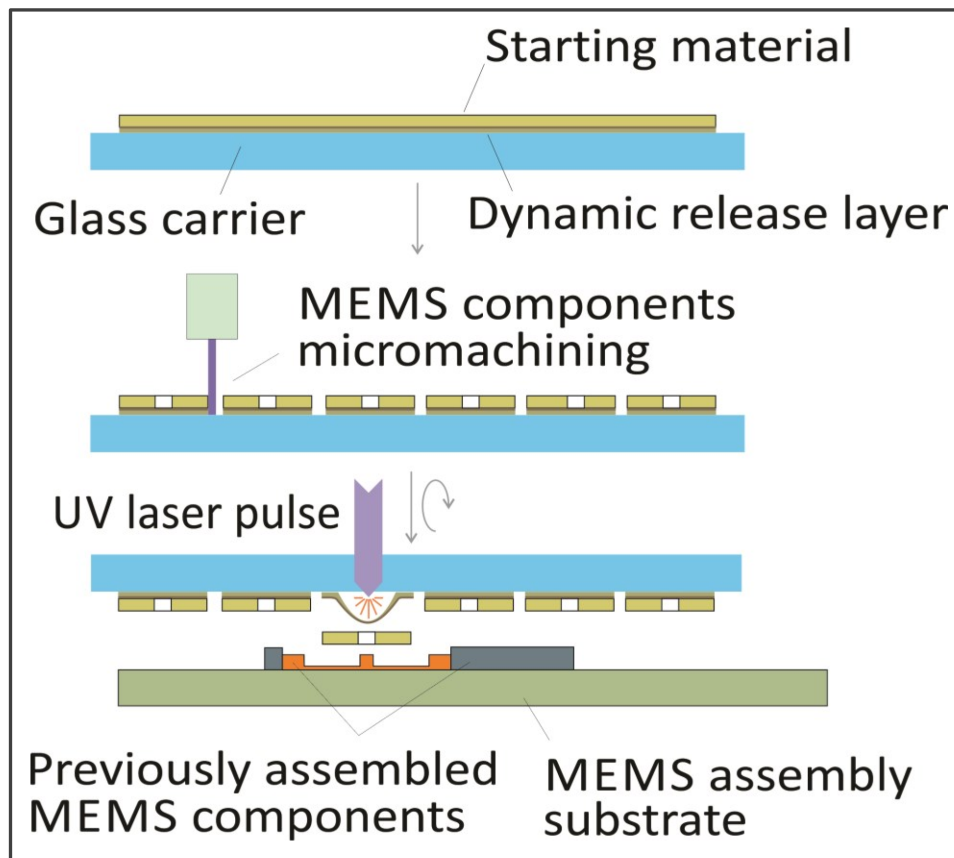

Figure 42. Main steps in LA^3 for starting material in thin sheet form.

CHAPTER 5. EXPERIMENTAL RESULTS AND DISCUSSION

The development work for *tm*SLADT, LEAP and LA^3 included validating the individual processes for the materials and components they were intended to fabricate, manipulate, and assemble. The validation included studies of transfer precision, accuracy, and placement rates for silicon tiles of various dimensions and thicknesses (65 µm and below), and metal components of different shapes and sizes. The sections in this chapter follow the sequence of the experimental work completed along the way.

5.1. Thermo-Mechanical Selective Laser-Assisted Transfer of Silicon Components

The samples for these first experiments were prepared following the procedure outlined in Section 7.2. Each processed wafer contained 350, 670, and 1000 µm square dies, which were singulated by both laser ablation and reactive ion etching. Although all three die sizes were transferred, the initial set of experiments focused on the 670 µm square dies, since they closely represented an active RFID device die used in the subsequent demonstration of functional devices presented previously [40, 102, 104, 105]. For direct comparison, 200 mW average power was used to transfer both the RIE and laser singulated dies. After setup trials, several sets of transfers were completed with RIE and laser singulated dies. Of the RIE singulated dies, a set of 33 dies were chosen for measurements. After inspection with an optical microscope, data for two dies were deleted because of poor DRL quality (contamination) in that area. Of the laser singulated dies, a set of 21 dies were chosen for measurements. Data for other dies were deleted after inspection showed that they were not completely singulated.

5.1.1. Transfer rate

The transfer rates for silicon components transferred using *tm*SLADT were studied using samples prepared with 5% PE7 in THF following the procedures described earlier. After

placement, pictures were captured of the transferred dies with an optical microscope to evaluate placement accuracy and precision. The translational precision and rotational displacement were measured from the photographs using imaging software.

SEM images of laser-singulated and RIE-singulated die sites are shown in Figure 43. As seen in the images the DRL material was completely removed in the streets during the reactive ion etching process, while the laser singulated site shows evidence of partial ablation of the DRL in the same area.

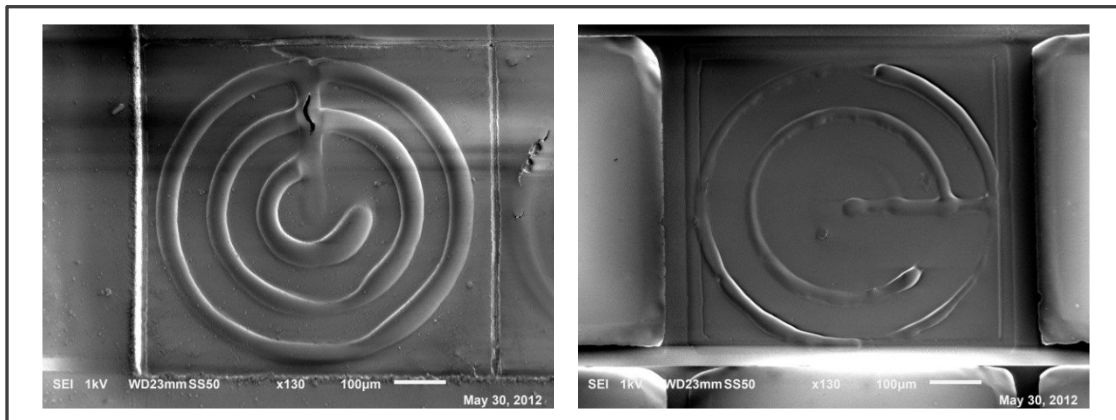

Figure 43. SEM image of laser-singulated die site after transfer (*left*), SEM image of RIE-singulated die site after transfer (*right*) [104].

The transfer rates in these experiments were 85.7% (18/21) and 93.5% (29/31) for the laser-singulated and RIE-singulated dies, respectively. With this limited data set, the RIE-singulated dies had a better transfer rate. This is consistent with other investigations with different laser power settings and adhesive formulations. Because of the nature of the RIE process, wider streets are formed between neighboring dies, while the laser-singulated dies have only the kerf-width separating each die. If the dies have been carefully laser-singulated, the DRL is left intact in the streets, but this is usually hard to accomplish due to variation in the

silicon thickness of the sample. In contrast, the RIE process always removes the blistering layer in this area without negatively affecting the neighboring area under the components. This effectively de-couples the DRL under each die from its neighbors and may allow for easier transfer. Also, debris and/or recast DRL material can build up in the streets in the laser-singulated dies, which possibly inhibits die transfer. Finally, the area of the RIE-singulated die that is in contact with the DRL is effectively reduced. This most likely reduces the adhesive force which needs to be overcome by the DRL blister, and results in a higher transfer rate.

5.1.2. Precision and accuracy

5.1.2.1. Effects of laser power. To determine the effect of different laser parameters (power and scan head speed) on DRL blister formation, a simple experiment was performed. The laser was set to 15 kHz repetition rate, and the laser power and scan speed were varied as the laser scanned across the DRL with no die attached. The DRL consisted of the polyimide layer and 5% PE7 in THF. The two laser parameters were set to three different levels, which resulted in 9 different combinations. The laser power was set to 150, 200, and 250 mW, and the scan speed was set to 200, 300, and 400 mm/s. Selected SEM images of the DRL after scanning with a circular pattern are shown in Figure 44.

The analysis of the experimental results suggested that the probability for blister rupture increased with the laser power and decreased with the scan speed. The 150 mW blisters were largely intact with a few small ruptures, mostly independent of scan speed. The 200 mW blisters scanned with a low speed were ruptured, whereas the blisters scanned with the same power but at higher speeds were less damaged. All of the 250 mW blisters were badly ruptured, and those scanned with a low scan speed were most severely damaged.

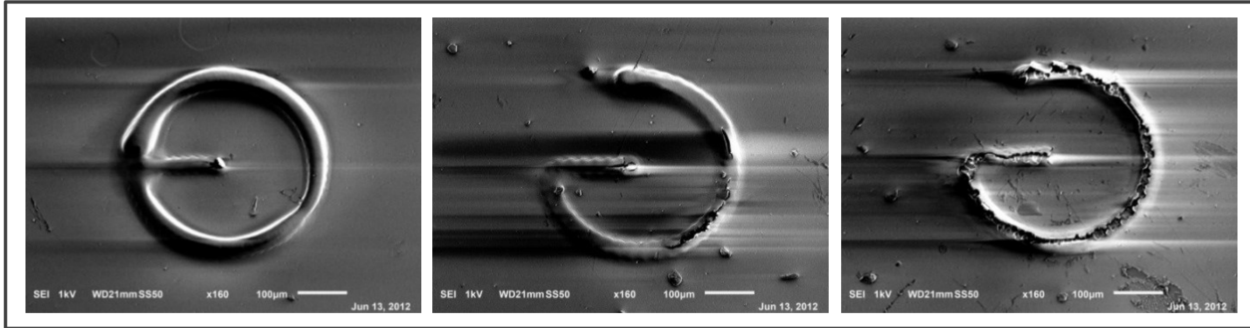

Figure 44. SEM images of DRL after scanning with various laser parameters, 150 mW power, 300 mm/s scan speed (*left*). The blister formed in the DRL is largely intact, 200 mW power, 400 mm/s scan speed (*center*). The blister is partially ruptured, 250 mW power; 300 mm/s scan speed (*right*). The blister is completely ruptured. The streaking seen in the SEM images was due to charging of the polyimide, and was not actually present in the layer [104].

The use of a multiple-pulse, high-repetition rate laser in our experiments was dictated by the limitations of the available equipment. It may be argued that a single pulse transfer mode in which an individual blister with a size smaller than the size of the transferred die and a shape corresponding to the shape of the die, generated by a single-pulse laser, would provide a better transfer rate and higher transfer precision. The presumption is that the single blister will push the die uniformly in a single-action fashion, as opposed to the current method in which the blister is formed very quickly (in about 1 μs) but progressively as the beam scans the DRL. In the latter situation, it may be speculated that the transfer is initiated at an off-center point(s) at the beginning of the scan line. If this is the case, the die would travel in an orientation that is not parallel to its initial position, which would eventually result in a deviation from the intended location on the receiving substrate. At this point, the evidence in support of this conclusion is only circumstantial; a time-resolved study using a high-speed camera, similar to that carried out by Brown and co-authors [103] would help with understanding and optimizing both the blister formation and the die transfer process for greater precision and transfer rates.

5.1.2.2. Adhesive layer strength effects. To determine the effect of the PE7 concentration on transfer rate and placement precision/accuracy, samples were prepared with 10% and 25% PE7 in THF, and the results were compared to the samples with 5% PE7 in THF. Laser transfers were performed on RIE-singulated dies. After optimizing the power setting, 30 transfers were attempted with each concentration. For 10% PE7 in THF, the transfer rate was 83.3% (25/30). The power used for transfers was 250 mW. The results for this concentration were similar to those of 5% PE7 in THF, although the displacement appeared to be slightly higher. For 25% PE7 in THF, the transfer rate was 86.7% (26/30). The power used for these transfers was 400 mW. This resulted in much larger displacements, with some of the die moving more than one die width. The reason for this was probably the blister rupturing resulting from the higher laser power (see Fig. 44c) and the subsequent change of the transfer mechanism from thermo-mechanical to ablative with all the negative consequences of such change as discussed elsewhere [102]. Also, at this power setting, the side of the dies adjacent to the DRL showed evidence of laser ablation during the transfer process. The 5% PE7 in THF clearly displayed the best transfer rate, and lowest displacement after transfer. Brown and co-authors [103] have shown that the presence of a thin layer of material on the surface of the blister layer does not have a significant effect on the size and shape of the blisters that form. Therefore, the observed differences in the transfer rates were due to only the adhesive properties of the different amounts of PE7 adhesive deposited. Hence, 5% PE7 in THF adhesive formulation was used for further characterization of the transfer process and all subsequent experiments.

5.1.2.3. Dicing method effects. Figure 45 shows evaluations of the *tm*SLADT process showing displacement distances in both X and Y directions for 670×670 μm, 50 μm thick Si dies subjected to laser singulation (Figure 45, left) and RIE singulation (Figure, 45 right).

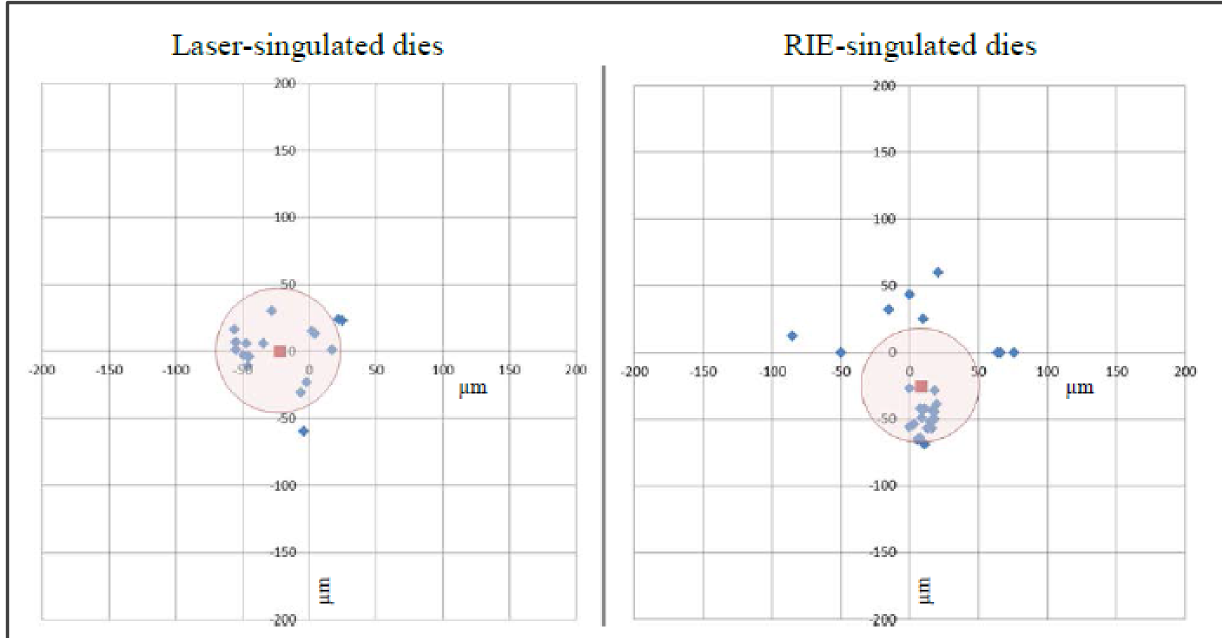

Figure 45. XY scatter plots of transferred 670×670 µm, 50 µm thick Si dice, showing lateral displacements in µm for laser-singulated (*left*) and RIE-singulated (*right*) dies from their release positions. The circle represents the 6σ region, where σ is the standard deviation; the center of the circle represents the mean radial displacement [104].

The mean radial displacement for the laser-singulated dies was 22.4 µm with a standard deviation of σ = 14.5 µm. For the RIE-singulated dies and omitting one outlier, these numbers were 26.8 and 13.6 µm, respectively. The angular displacements (rotations) of the transferred dies with respect to their original positions were negligible in both cases.

The laser-singulated dies exhibit slightly better placement precision than the RIE-singulated dies (22.4 µm vs. 26.8 µm) based on these measurements. Though, if the samples outside of the 6σ circle are removed, the precision of the RIE-singulated die becomes much better. The scattering observed in the RIE-singulated dies may not be a result of the selected wafer dicing method. Rather, it was probably due to problems in sample preparation for these

experiments. Indeed, the post-experiment inspection revealed evidence of incomplete bonding of the dies to the DRL in some areas of the wafer.

Overall, both types of dies had placement accuracy and precision results much better than those from the ablative laser-assisted transfer process and are comparable to the thermal laser-assisted transfer process results described in the literature [83, 84]. Karlitskaya *et al.* [83] argued that in order for the laser-assisted die packaging to be accepted by the industry as an alternative to the conventional pick-and-place robotic assembly, the component placement accuracy should be at least ±35 µm. It is obvious from the results presented in Figure 45 that the *tm*SLADT technique not only meets but significantly exceeds this requirement.

5.2. Thermo-Mechanical Selective Laser-Assisted Transfer of Metal Components

This experimental work consisted of two separate parts. The first part was aimed at verifying the *tm*SLADT mechanism as a viable option for transfer of materials other than silicon and shapes other than squares, which was the typical geometry transferred during previous experiments with dummy and functional silicon dies. The second part included the design and fabrication of a simple MEMS magnetic switch as a technology demonstration of the proposed LA^3 method.

Aluminum foil was chosen as a first option for the initial LA^3 work as it is readily available in thin sheet form and very pliable. The carrier samples were prepared in a manner similar to the one described previously where the UV-transparent carrier is spin coated with a Dynamic Release Layer and the aluminum foil is applied over the adhesive. In the next step, different shapes, such as squares, circles and washers with various diameter and rim thickness were cut in the foil. Finally, these various shapes were transferred over to a receiving substrate spin coated with pressure sensitive adhesive catch (Figure 46).

Figure 46. Various shapes cut from aluminum foil after transfer to a receiving substrate.

The transfer gap in these experiments was set at 261 μm using shims and the thickness of the aluminum foil used was 24 μm, which gives a ratio of air gap to component thickness of about 10 to 1, which is much higher than what has been reported possible when ablative transfer mechanism is used [77]. The objective in these initial proof-of-concept experiments was not to measure transfer rate and precision, but rather to observe and compare the parameters and results to what have been already achieved in transfer of silicon tiles and functional IC dies. One would not expect that the transfer dynamics will differ significantly when the starting material is silicon or metal since the laser beam action in *tm*SLADT is separated from the components by the blistering layer which contains the plume of expanding gasses within. Indeed, the laser power used in these experiments was in the range of 0.15W to 0.3W depending on the size of the components with 0.175W to 0.2W and 400 mm/second scan speeds typical for aluminum squares

and circles with side and diameter of 670 μm, accordingly, which is the usual size of silicon components used in prior rate and precision of transfer experimental work. The laser transfers were again accomplished at 15 kHz repetition rates by scanning the DRL beneath the components with a pattern of three concentric circles that start from the smallest one and work outward (Table 4).

Table 4. Transfer parameters used in two independent experiments

	Power used in transfer of:		
Size of components	Silicon	Aluminum	Notes
350 x 350 μm	150 mW	150 mW	Scan repetition rate = 15 kHz, Scan speed = 400 mm/s, Scan pattern – three concentric circles Flat-top beam profile
670 x 670 μm	150 mW	175 mW	
1000 x 1000 μm	250 mW	300 mW	

It should be noted here that the transfer of the aluminum components was set up as a separate experiment, but complimentary to the previous silicon transfer work. This means that the usual laser power from preceding experiments was used as a benchmark starting point only, while all other parameters were kept the same. From that point the power was varied up and down until acceptable transfer rates were obtained. As seen in Table 4 there is variation in the power used to transfer the different materials, but since these experiments were conducted at different times using separate carrier substrates, the variations can be attributed to factors such as disparities in the DRL quality and day-to-day variations in the laser station (variations affecting beam quality and the required daily power calibration of the system). Once an acceptable power setting is determined, the transfer of square components for instance is done using a checker board pattern which allows observing the position of the transferred parts relative to non-

transferred ones through both the carrier and receiving substrate. As seen in Figure 47, the actual placement position of transferred aluminum squares is very close to the intended one in the middle of the space left by the surrounding squares with insignificant translation and rotation witnessed in some cases.

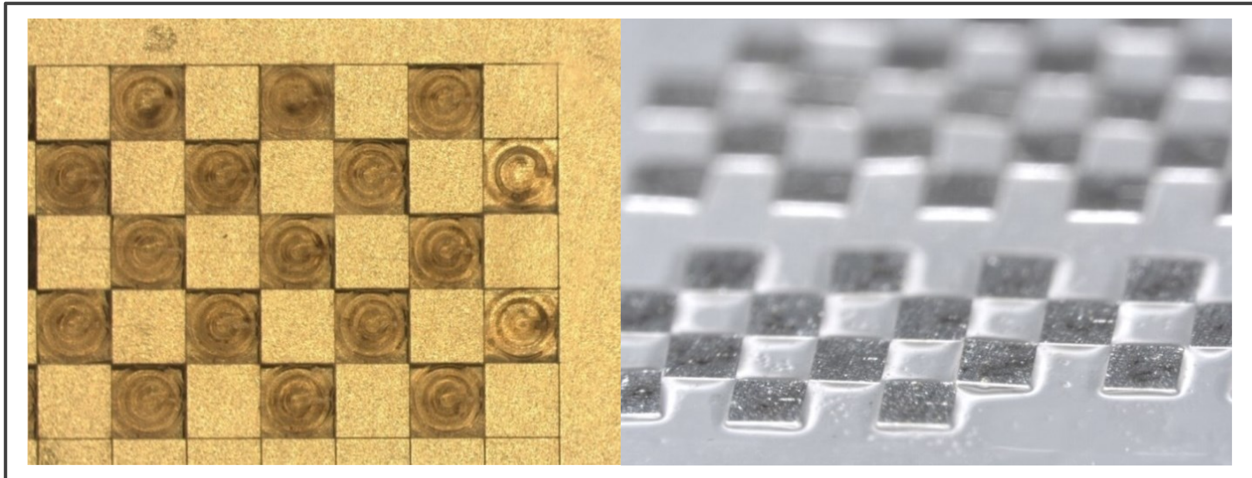

Figure 47. Transferred aluminum squares (670 x 670 μm); image through carrier substrate showing very good precision of transfer (*left*), and image of a receiving substrate with check board patterned transferred dies (*right*).

The 670 μm x 670 μm squares cut in the aluminum foil were used in order to compare transfer rates for silicon and aluminum as data for the same size silicon tiles were already available from previous work. Two checker board placement attempts with laser power set at 200 mW resulted in 18 and 22 successful out 20 and 24 attempted transfers, respectively, resulting in a transfer rate of 90% and 91.7%, correspondingly (Figure 48). These transfer rates compare well to those obtained in previous optimized experiments using the same power setting for laser singulated silicon squares with the same size and thickness of 65 μm, which were in the range of 85.7% to 93.5% [40].

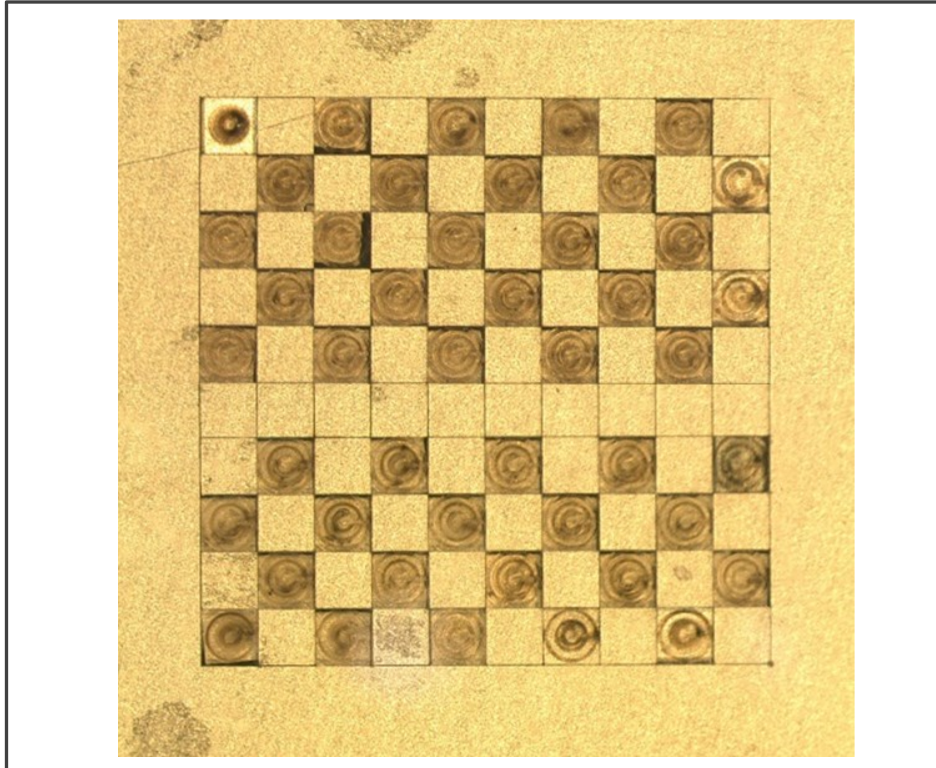

Figure 48. Transfer of aluminum square tiles (670 x 670 μm) with thermo-mechanical Selective Laser Assisted Die Transfer (*tm*SLADT) mechanism; image through carrier substrate.

An interesting effect was observed when the square size was reduced from 670 μm to 350 μm per side while keeping the laser power setting at 200 mW and all other relevant parameters the same. As seen in Figure 49, these settings resulted in very poor precision of transfer although the transfer rate was 45 successful out of 50 attempts or 90%. Upon closer inspection of the DRL under a high magnification microscope it was discovered that these setting resulted in blister rupture leading to laser propulsion that is closer in nature to an ablative release rather than a thermo-mechanical one.

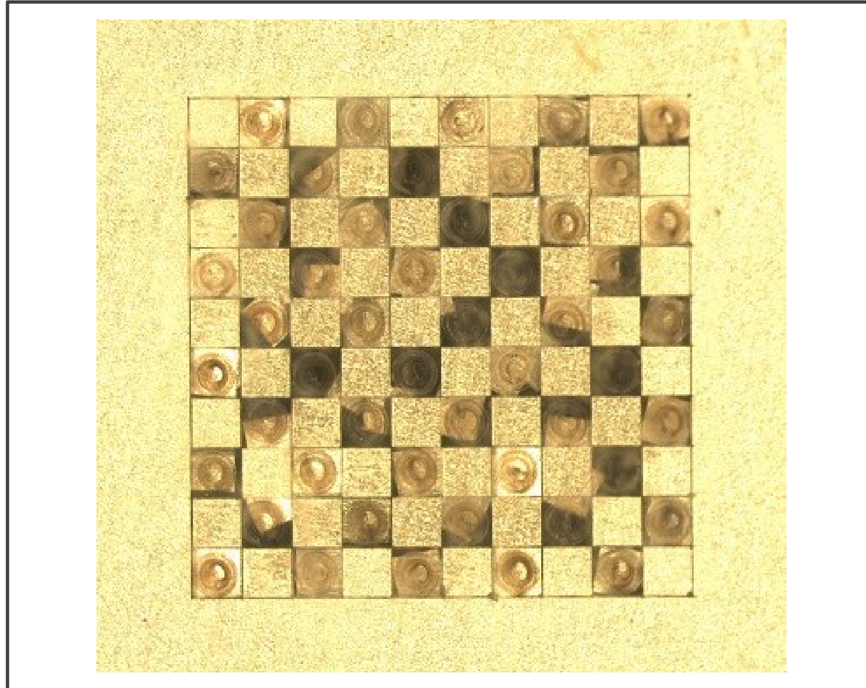

Figure 49. Poor precision of transfer of 350 by 350 μm aluminum squares by ablative release mechanism.

Precision and placement rates of other shapes micro machined in the aluminum foil were not measured and calculated, but rather the limits of sizes that can be transferred were observed. Figure 50 shows circles and washers of different diameters and rim thickness placed on a receiving substrate using the *tm*SLADT. Circular shapes with diameters as small as 500 μm (not shown) and as large as up to 1500 μm in diameter were transferred. It was observed that as the diameter of the circle approached 1500 μm it was getting harder to release the components using only three concentric circles, hence larger structures may need different scan patterns. However, the technology demonstrated here was developed with the idea to manipulate structures that cannot be easily assembled by pick-and-place methods and having an upper diameter limit of 1500 μm should be sufficient for laser-assisted assembly as sizes bigger than that can easily be handled with more conventional equipment.

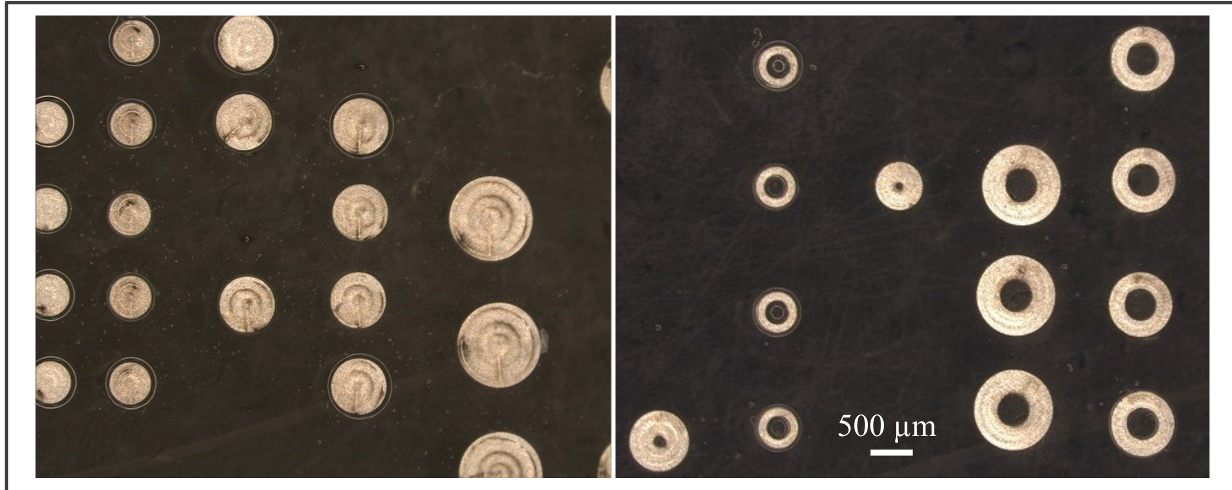

Figure 50. Circles and washers of various shapes and designs on a receiving substrate.

Table 5 on next page shows the inner and outer diameter and the resulting rim thickness of the washers that were transferred and the resulting rim thickness. The scan pattern of three or fewer consecutive circles depending on rim thickness was used again, but the rings were brought closer together in order to scan only the area under the washer rim. Such a scan pattern results in transfer of the ring section only while the "core" is left on the carrier substrate.

As evident by the number of successfully transferred washers of different sizes seen in Figure 50 as the inner diameter of the washer decreased, the number of successful transfers was reduced. Since transfer of circular shapes was demonstrated already, a possible explanation for that occurring is that cutting a circle with a diameter of only 100 μm using a laser spot of about 20 μm results in excessive heat buildup in a small area leading to melting and re-solidification or other structural changes in the polyimide blistering layer (Figure 51).

Table 5. Washer dimensions and transfer rate

From left to right on Figure 50	Outer D, µm	Inner d, µm	Ring, µm	Successful/Attempted Transfers
Column 1	750	100	325	1/6
Column 2	500	300	100	6/6
Column 3	600	100	250	2/6
Column 4	1000	400	300	4/6
Column 5	800	400	200	6/6

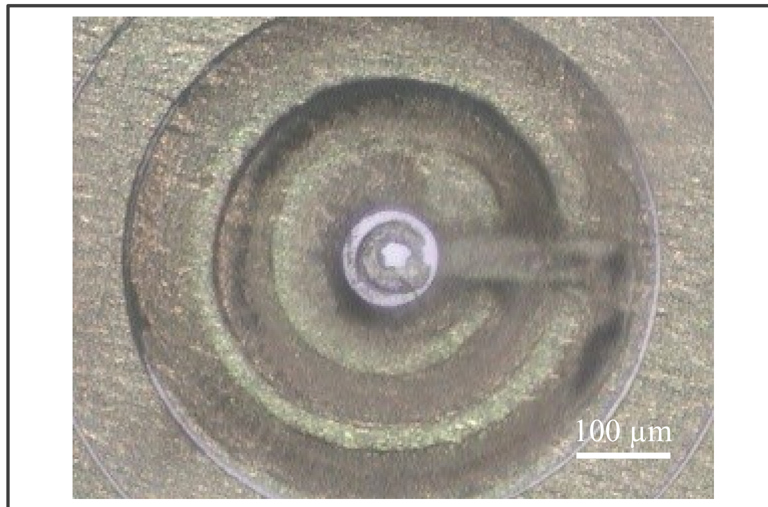

Figure 51. Damage to Dynamic Release Layer sustained in machining of very small circle; image through quartz carrier with back-light.

These initial, proof-of-concept results demonstrate the feasibility of using Laser-Assisted Advanced Assembly for micromachining and transferring components from materials other than silicon. In addition, the last results presented here show once again that the transfer rate and precision of *tm*SLADT as a laser propulsion mechanism are independent of size and geometry at least in the range investigated, that is from 250 µm to about 1500 µm. As LEAP has already been

demonstrated as a viable microelectronics packaging process, the addition of LA^3 to its capability will allow fabricating and assembling not only the electronic, but also the mechanical part of a MEMS device.

5.3. Technology Demonstrator: E-RMCPS (Electromagnetic-Responsive Mobile Cyber-Physical System)

An inter-institutional collaboration proposal between NDSU, SDSU, and UND on a project entitled "Fundamental Research on Electromagnetic-Responsive Metamaterials for High Efficient Mobile Cyber-Physical Systems," provided the opportunity to demonstrate LA^3 as a practical components fabrication, manipulation, and assembly technology.

The envisioned purpose of Electromagnetic-Responsive Mobile Cyber-Physical System (E-RMCPS), developed as a part of this project, is to improve the wireless communication system efficiency within battery powered devices. The control of electromagnetic properties (permittivity) and radiation, as well as environmental sensing will be implemented in this unique electromagnetic-response metamaterial (E-RM), by using a conductive carbon microfiber metamaterial that uses embedded MEMS-based particles [118].

Figure 52 shows schematically the proposed configuration of E-RMCPS. The metamaterial offered will be based on a carbon-fiber composite that will have capacitive spheres with electromagnetic enabled MEMS switches embedded in the matrix. The radiating element will be built around a two element phased antenna design, which is well described in the literature [119]. The topology and placement of the MEMS devices has not been precisely defined at this point, but their number and position will be chosen in a manner such that the electromagnetic field along the length of the array can be controlled by an external field [118].

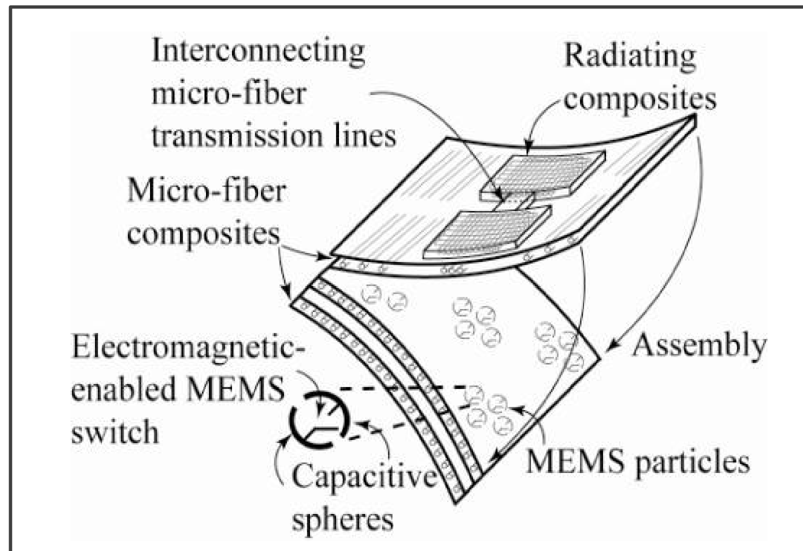

Figure 52. Schematic representation of Electromagnetic-Responsive Mobile Cyber-Physical System E-RMCPS [118].

The MEMS-based magnetic switch action in the presence of a strong direct-current field is schematically illustrated in Figure 53. The switch is part of the so called capacitive spheres and is normally in an open position with a certain known capacitance. When an external electromagnetic field from the conducting carbon fibers is applied (Figure 53), the switch reacts by moving the membrane, therefore changing to a closed position and making a continuity connection with the bottom contact of the capacitive hemisphere. This in turn changes the capacitance of the whole particle and alters the permittivity of this metamaterial. Hence, the placement of the particles in the material needs to be in regions of the metamaterial that will allow the switch to respond to the effect of the external field [118].

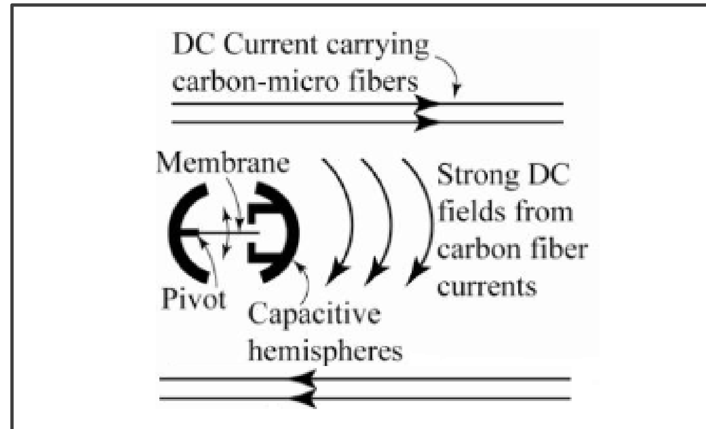

Figure 53. MEMS switches in DC field and basic device schematic [118].

5.4. Magnetically Actuated Switches

The magnetic switches that will make it possible to verify the idea of E-RMCPS metamaterial were designed with two considerations in mind. The first and major consideration is that the switches need to meet the requirements for the MEMS-based magnetic switch, as defined in the project description and briefly described in the previous section. The second consideration addresses the current limitations of the Laser-Assisted Advanced Assembly process. These limitations arise from the design of the process on one hand and the available component fabricating capabilities on the other and are as follows:

1. The LA^3 process can manipulate and transfer components and parts in one direction only, i.e. along the z-axis direction. The x- and y-axis movement can be used merely for aligning purposes but no manipulation using the laser beam is possible along these directions.
2. The starting material for the components that will be transferred need to be in thin-sheet form, preferably pliable or impeccably flat such as the case with bare and functional silicon wafers.

3. The starting materials need to efficiently absorb laser energy at 355 nm, which is the operating wavelength of the frequency-tripled Nd:YVO_4 laser that our system has, in order to allow micromachining of MEMS components from these materials.
4. The components that will be transferred using *tm*SLADT preferably need to be smaller than about 1500 μm which will allow transfer without a need to modify the blistering or adhesive layers of the Dynamic Release Layer.
5. The fixture holding the carrier substrate allows using only 3" diameter quartz discs; hence that is the maximum size of the starting material for parts fabrication.

Based on these restrictions, it was decided that the switch will consist of layered materials such as metal foils and polyimide films that are readily micro-machined by a 355 nm laser. For simplification of the structure in these first attempts of using *tm*SLADT as the MEMS fabrication and assembly technique, the pivoting membrane of the MEMS switch described in the preceding section was substituted by magnetic nickel-coated micro particles that align and form electrically conductive columns in the presence of an external magnetic field. Such particles have recently been demonstrated in anisotropic conductive pastes, and in that application they form continuous columns in the presence of external excitation to achieve electrical contact between substrate pads and IC bumps, for example. Joining of the ensuing layers that will form the MEMS structures can be achieved by using epoxy or otherwise by using alternating layers of adhesive coated and uncoated structural layers.

The described magnetically actuated switches fall easily in the size range typical for MEMS and their intended ability to convert one mode of energy into another based on external excitations makes them a classic MEMS sensor. Because these MEMS structures may be imbedded in a flexible matrix or may need to withstand some pressure during the metamaterial

manufacturing step, they need to be flexible or at least made of a material that is not brittle and allows for some level of elastic deformation. Thin metal foils and polymer materials can fulfill these requirements, but these are not readily micro-machined by traditional MEMS fabrication techniques such as bulk micromachining. The presence of magnetic particles that need to be dispensed in the MEMS switch before final assembly rules out the remaining MEMS fabrication techniques as they do not allow assembly, as discussed previously. The Laser-Assisted Advanced Assembly which was described in the preceding chapter can accommodate all requirements for fabrication, assembly, and functionality of these magnetically actuated structures.

5.4.1. Switch prototypes fabrication and testing

In order to test the idea of building a layered structure magnetic switch for embedding in a composite metamaterial larger prototypes were first build and tested for functionality in the presence of external magnetic field. The magnetic switch prototypes are based on two parallel conducting copper films for contact surfaces with a dielectric layer between them which will contain the micro-machined cavity and magnetic particles (Figure 54). Preferably all starting materials have to be readily available.

For the purpose of this demonstration, the bottom electrode needs to also serve as a support substrate, hence a conventional Cu-clad FR4 board was chosen to serve the purpose of the receiving substrate in the laser assisted assembly. The top electrode was made of a 125 µm (36 gauge) soft Cu sheet. For the dielectric layer, a polyimide film (Kapton®) was chosen as it is readily available and comes in different standard thicknesses.

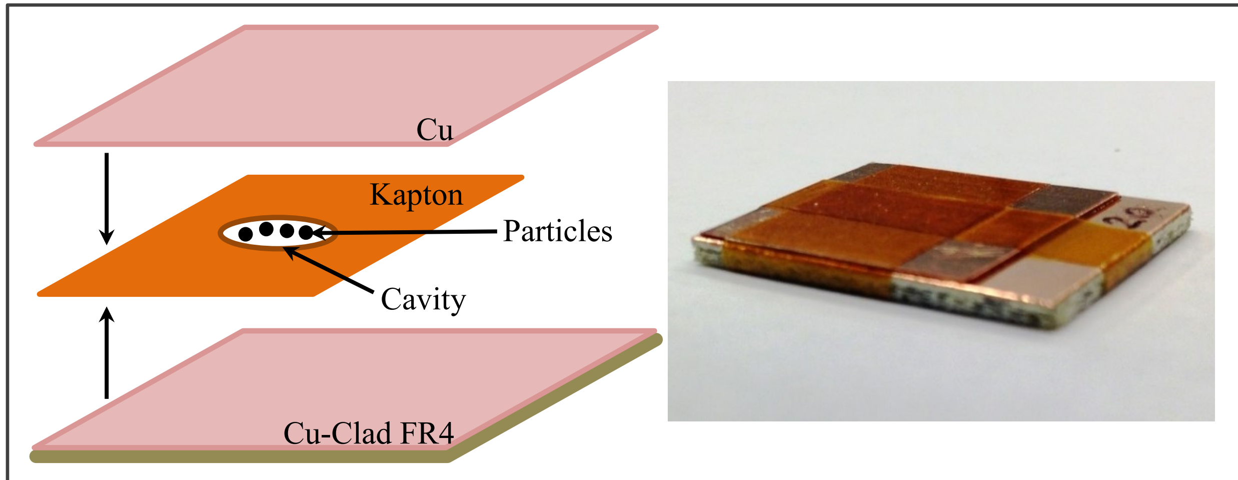

Figure 54. Magnetic switch first prototype; switch parts schematic (*left*) and assembled switch (*right*).

The cavity in those first prototypes that will be referred to as large magnetic switches or simply large switches, was made using a standard office punch which gave a cavity diameter of 7 mm; switches with three different cavity depths were produced by using 125 µm, 575 µm, and 1025 µm Kapton® film . To make the switches, the polyimide film is placed on the FR4 substrate and the cavity is then partially filled with Potters Industries' Conduct-O-Fil SM40P20 Ni-coated magnetic particles that have an average particle size of 40 µm. The mass of every switch is measured before and after magnetic particles are dispensed using an electronic scale with a resolution of 0.0001 gram; this was done in order to be able to compare the behavior of the switches when different amounts of particles are dispensed in the cavity. Finally, the top contact surface is placed on top of the polyimide film and the whole structure is secured with Kapton® tape as seen in Figure 54 right.

In order to observe the behavior of the switch, four large prototypes were made with a 125 µm cavity height and the resistance between the two parallel electrodes was measured without and in the presence of an external magnetic field. The magnetic field was provided by

two rectangular shaped parallel magnets with a fixed distance of about 6 mm between them. The two electrodes were “open” in the absence of a magnetic field and showed a resistance of about 1Ω (0.6Ω to 1.5Ω) when placed in the gap between the two magnets. When the magnetic field is removed the resistance quickly, but not instantly, increases to 50Ω and more (up to hundreds of Ohms), but the switch will not fully “open” unless shaken or bumped in order to fully break the magnetic particle column created in the presence of the magnetic field.

In a separate experiment, a small amount of the Ni-coated magnetic particles was placed in a transparent plastic box with a height of 7 mm and a magnetic field was applied to witness the particle behavior. The set-up this time allowed varying the distance between two couples of round magnets (Figure 55), therefore changing the strength of the magnetic field supplied. As the magnets are brought together the particles initially redistribute in a single layer on the bottom surface of the box. As the strength of the field is increased, concentration of particles right in the area of the magnets occurs and finally they start to build columns and were able to bridge the gap of 7 mm. In this case, with a very big gap between the two surfaces, the columns break instantly as the magnets are removed, but some columnar arrangement on the bottom of the box still remains. The effect is less pronounced when weaker magnetic fields are applied. This shows that appropriate amount of particles for the cavity surface area and volume will be needed in order break contact quickly upon removal of the external excitation.

These low-level experiments showed that the idea of building magnetic based MEMS switches is feasible. In the next step, more of the large switches described were assembled using controlled amounts of particles dispensed in the cavities and their behavior was observed by measuring the resistance between the contacts for different strengths of the magnetic field

(Figure 56). The magnetic field was varied by changing the distance between the two pairs of magnets.

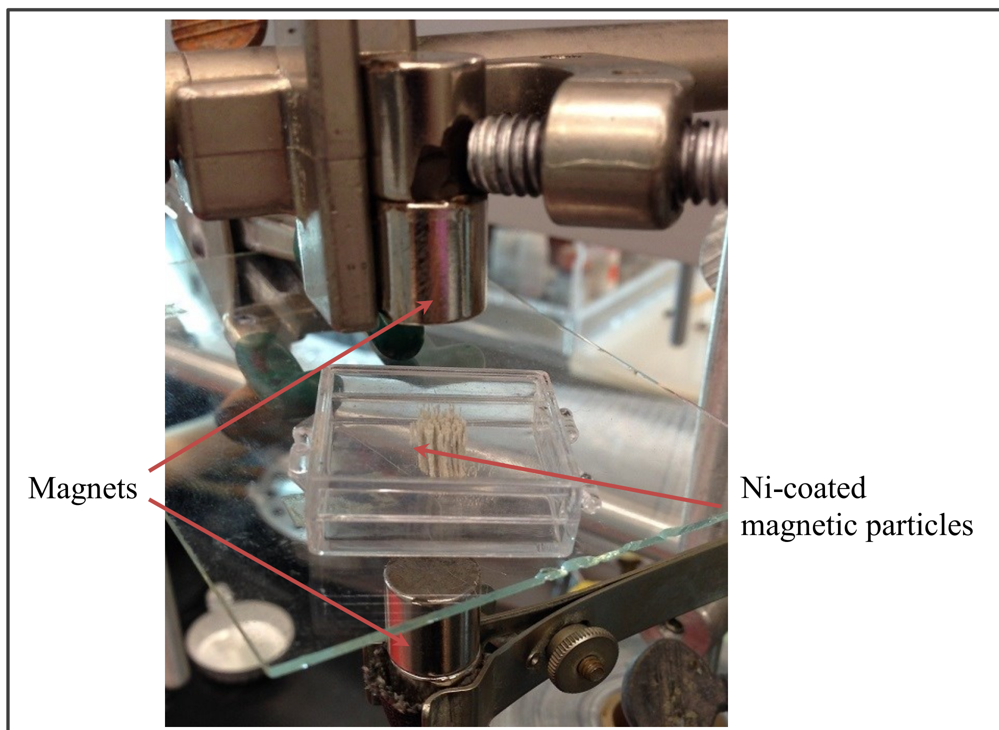

Figure 55. Magnetic particles in a transparent box placed between two magnets; the particles easily bridge the gap of 7 mm between the top and bottom surface. Distance between the magnets is 36 mm, corresponding to a magnetic field strength of 500 Gauss for this set of magnets.

Before the experiment start, the strength of the field was measured at the mid-point between the magnets using a gauss meter and recorded. The strength of the magnetic field as a function of distance between the magnets was measured and plotted to create the calibration plot in Figure 57, which was used in the subsequent experiments. The gauss meter was zeroed in the absence of a magnetic field before each measurement and as evident by the graph provided very good results.

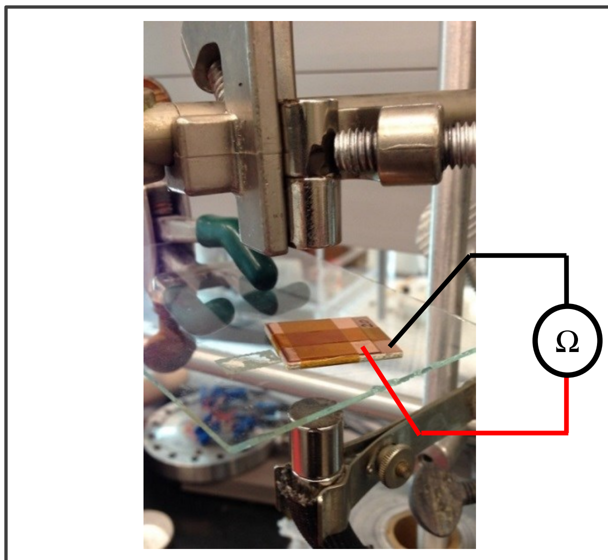

Figure 56. Switch during resistance test.

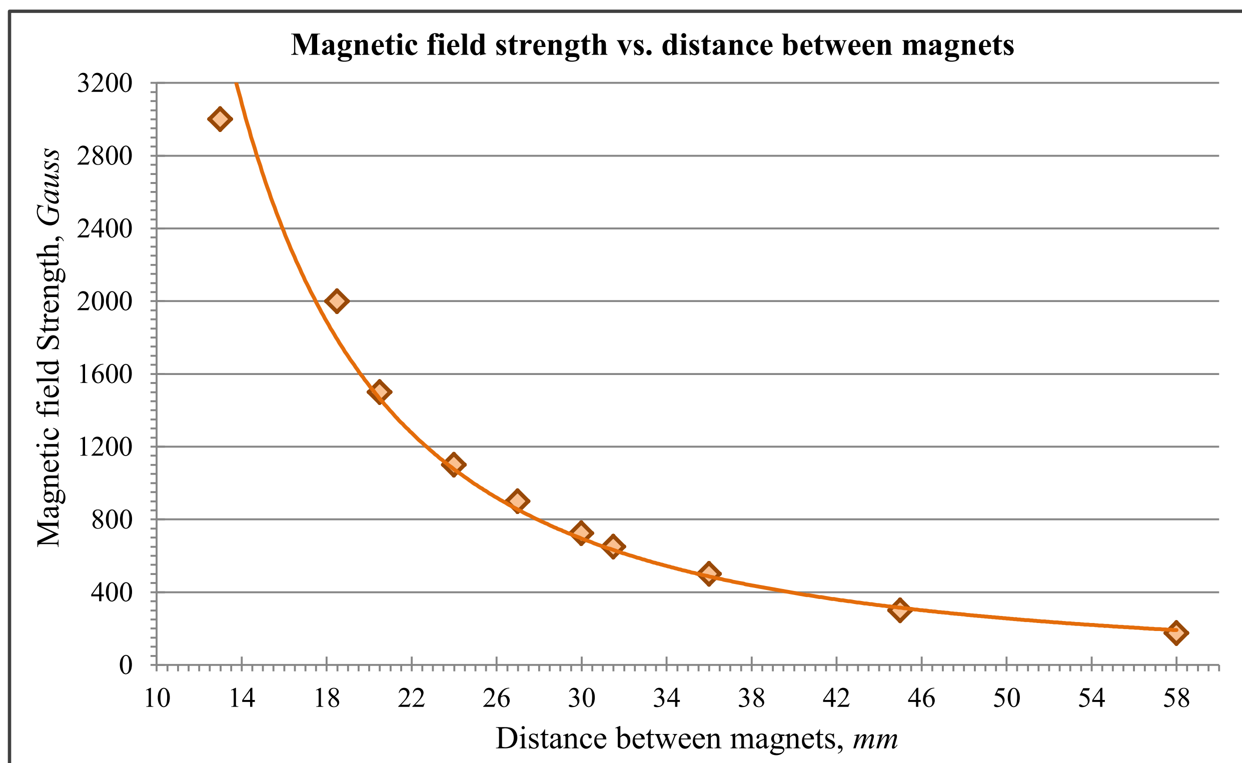

Figure 57. Magnetic field strength vs. distance between the magnets; orange diamonds are values measured, line is the fit.

5.4.1.1. Resistance test. In order to study the behavior of the switch, samples with dielectric layer thicknesses of 125, 575, and 1025 µm were built, keeping the diameter of the cavity constant and equal to 7 mm. Five switches of each different cavity depth were made and each cavity was partially filled with magnetic particles. The particles were first put in isopropyl alcohol to ease dispensing with a manual pipette. As mentioned previously, the mass of the particles dispensed in each cavity was measured and now converted to volume by using the specific weight of the material provided by the manufacturer.

Because the volume of the cavity in each of the three kinds of switches using different dielectric layer thicknesses is not the same a value that is referred to as R-value from now on was introduced. The R-value is equal to the ratio of the volume of the cavity to the volume of the particles in the cavity; this would allow linking the behavior of the dissimilar cavity volume switches in the presence of a magnetic field. In other words, the R-value is used to ensure that the cavities with different depths, therefore different volume, each receive “matching” amounts of particles, i.e. a cavity with a smaller volume will be filled with lesser amount of particles than a cavity with a bigger volume, but both will have the same R-value so if any differences in their behavior is observed it would not be attributed to the changed amount of particles. The R-values that were used were 20, 29, 40, 50, 67, and 100. So, for example, a switch with an R-value of 20 has a cavity volume 20 times bigger than the volume of the particles in it, therefore a switch with R-value of 100 has fewer particles than the switch with R-value of 20. The behavior of these switches was studied in a magnetic field that varied from 300 Gauss to around 1600 Gauss and of interest was how fast the resistance decreased as the magnetic field strength increased and at what point the overall resistance of the switch fell to the low Ohm range, i.e. less than 10 Ω.

Figure 58 shows the behavior of the switches with two different R-values as magnetic field strength is increased. As seen in this figure as the amount of particles in the cavity is increased, the switch resistances reach lower values in the same magnetic field; this makes sense, as more particles are available to form columns. Figure 59 shows resistance behavior as the R-value of the switches decreases (or the amount of particles increases) for different magnetic field strengths; as evident, as the R-value decreases, it is possible to obtain smaller resistance values for the same magnetic field strength.

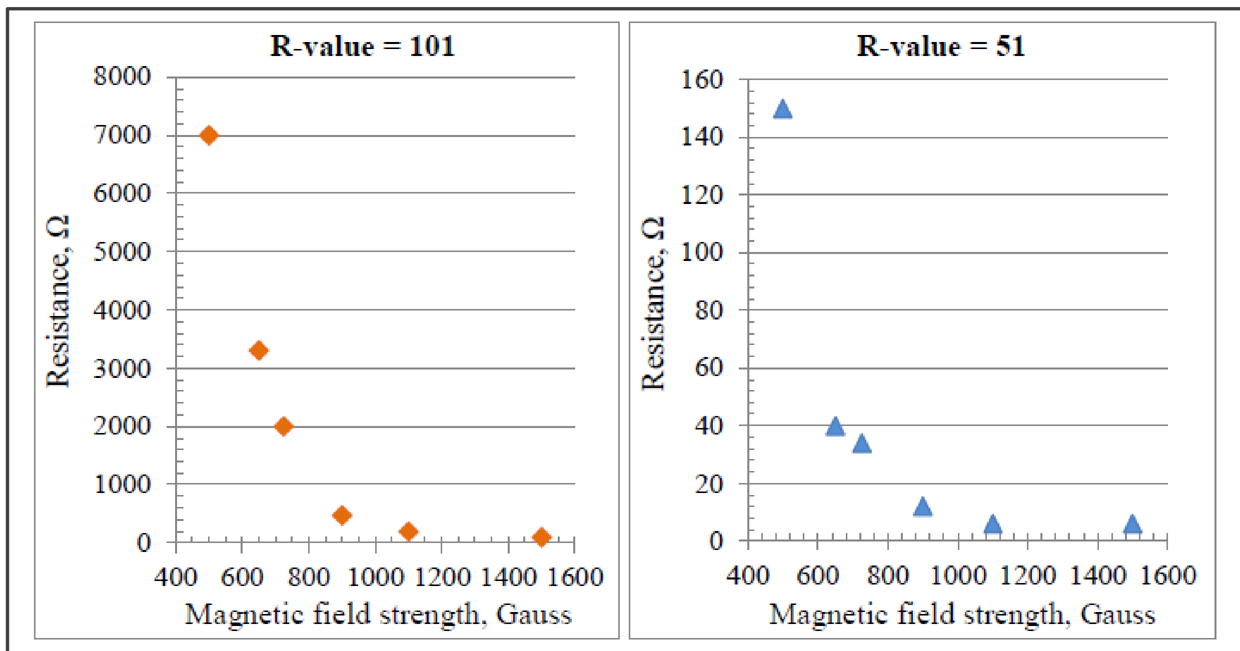

Figure 58. Resistance as a function of magnetic field strength for switches with different R-values; note the similar behavior, but different scale on the y-axis.

During observations of the particles behavior in a magnetic field using the transparent plastic box and based on the results from the resistance experiments, some scaling effects become evident. It was seen that switches with higher volume, hence higher height since diameter was fixed, approached the low resistance values faster and show more stable behavior

than switches with smaller volume/height having the same R-value. Upon closer inspection of particle behavior it was noticed that since the magnets area is bigger than the cavity area as the former are brought together, the particles first redistribute to cover the whole "area" of the magnetic field and as the field is increased the particles start to "climb" on each other to form columns. That means that although a switch with fewer particles may have the same R-value as a switch with more particles, the first will have fewer particles to start forming columns in the same cavity diameter. Hence, in order to reduce the field needed to close the switch it is necessary to decrease the area of the magnetic field (make it more concentrated), or to reduce the area of the switch cavity. Based on these results switches with smaller diameter were built and their behavior was studied.

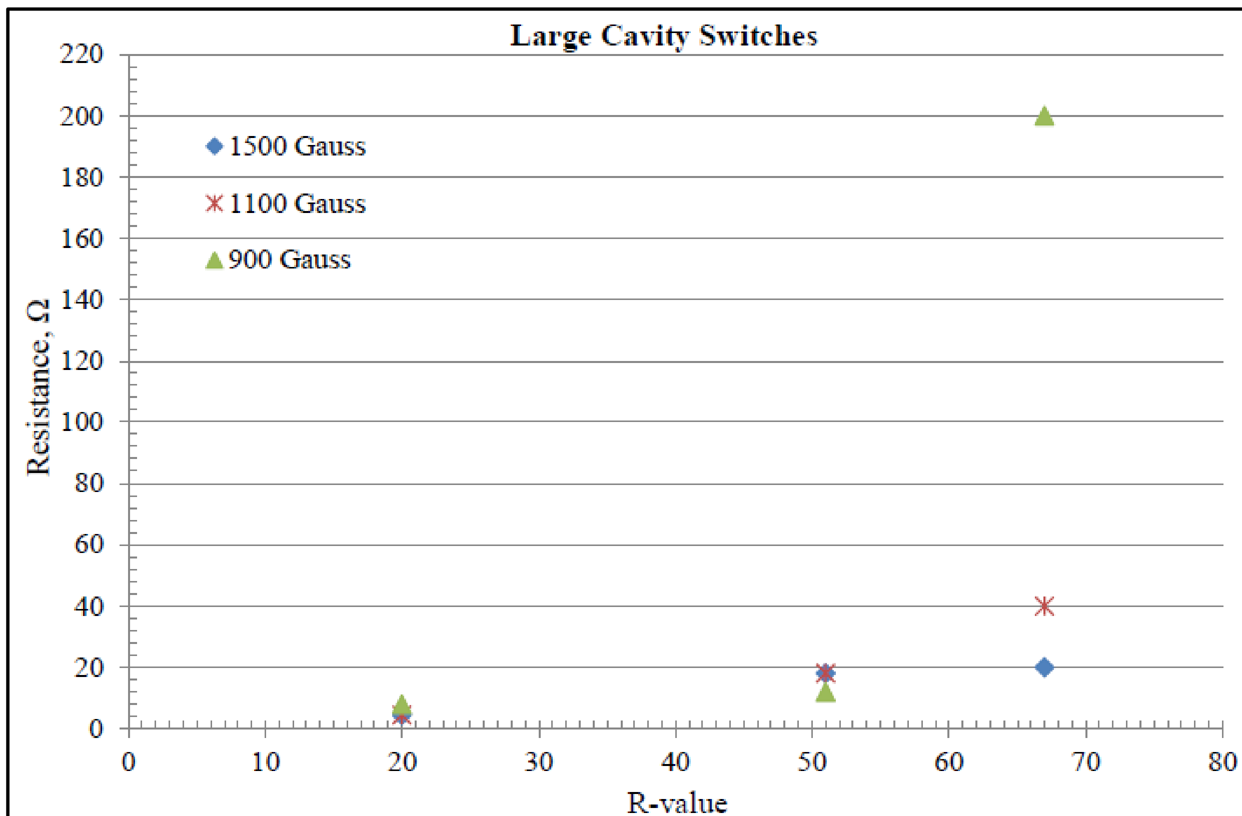

Figure 59. Resistance behavior of a sample of large cavity switches (cavity height of 125 µm) as a function of R-value for different magnetic field strength.

5.4.2. Cavity size scaling effects investigation

As described in the previous section, some scaling effects were observed when the large cavity switches were subjected to external excitation; the effects that reducing the contact area of the cavity has on its resistance and strength of the magnetic field to activate it were investigated. These switches, referred to as small switches from now on, were made with a fixed cavity diameter of 1.5 mm and a height of 125 µm. Five switches were built and their cavities were loaded with particles to achieve R-values of 20, 29, 40, 51, and 67, respectively. As seen in Figure 60 on next page, for comparable R-values, as the area of the cavity decreases, the activation field strength and resistance of the switch decreases. Note that for an R-value of 20, the resistance (y-axis) has the same scale, but the magnetic field strength (x-axis) scale for a small switch starts roughly where the one for a big switch ends; the resistance at 650 Gauss is 2.3 Ω for a small switch and 10 Ω for a big switch. The small switch activates in a magnetic field as low as 175 Gauss, albeit with a relatively high resistance of 17.5Ω. The big switch, however, needs a field of more than 500 Gauss to activate with similar resistance values. The behavior of the switches with R-value of 40 is very similar. The small switch activates at fields as low as 400 Gauss with resistance of 5.5Ω (and drops all the way to 2.8Ω for 650 Gauss magnetic field). On the other hand a big switch shows resistance in the MΩ range for 650 Gauss (this has been reduced for graphic purposes to KΩ).

Otherwise, as Figure 60 shows, the overall response is very similar for big and small switches with different R-values; as you increase the R-value, the activation resistance increases for a constant magnetic field and as you decrease the area of the cavity, the activation field strength drops significantly if you keep the resistance constant. The behavior is consistent for different R-values and across different cavity sizes. If Figures 59 and 61 are compared, it can be

seen that small switches require weaker magnetic field to activate and show smaller resistance values when closed. In addition smaller switches can operate with larger R-values (meaning fewer particles) and still give acceptable resistance values; that is important as fewer particles will mean a smaller possibility for closing the switch if it is tilted on its side and will allow for simpler cavity design.

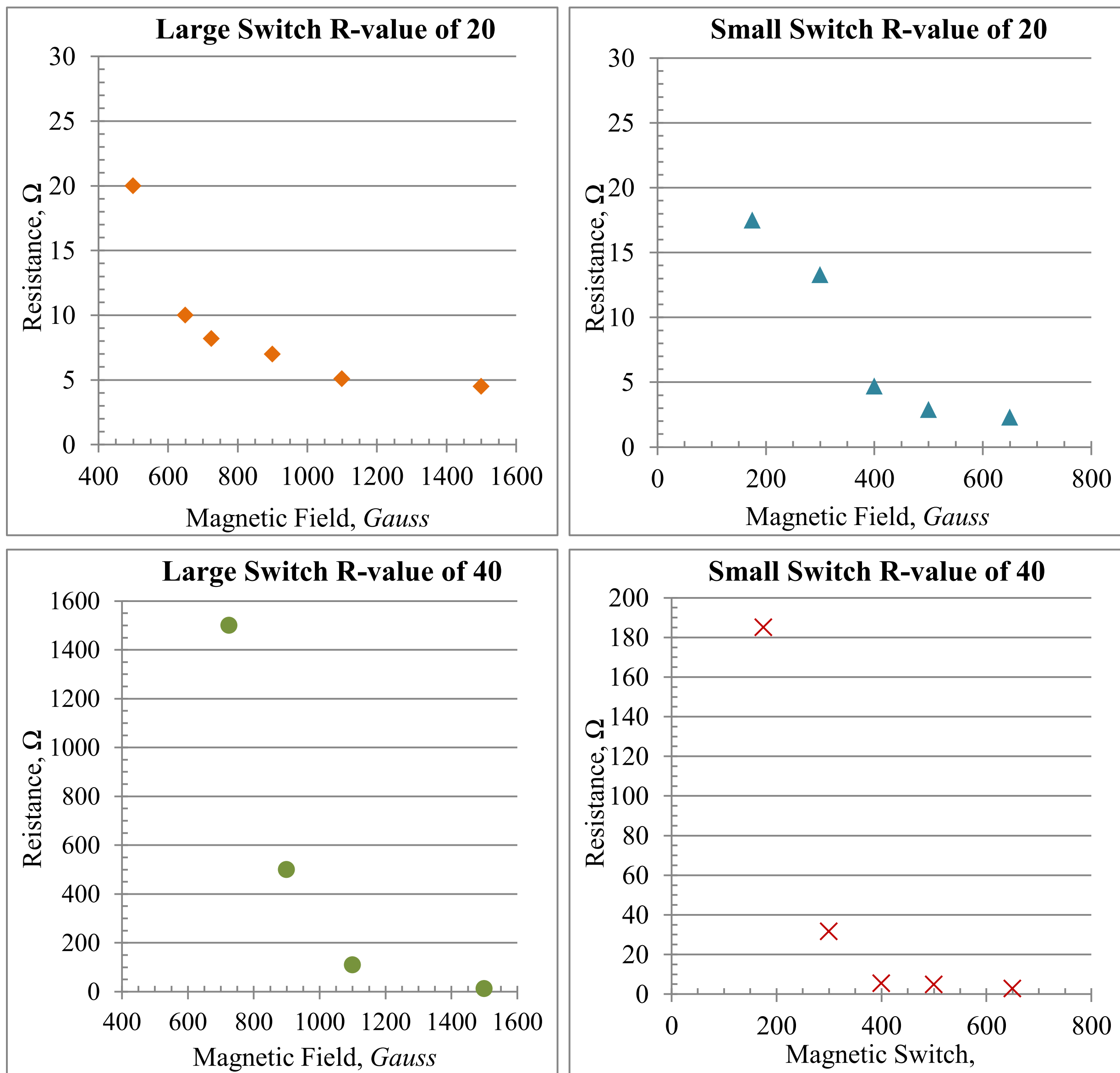

Figure 60. Resistance as a function of magnetic field strength for large (*left*) and small (*right*) switches for two different R-values, 20 (*top*) and 40 (*bottom*). Note the different x- and y-axis scales, but similar behavior.

These results were encouraging in the sense that a weaker field is needed to close a switch with a smaller cavity. If that trend extends to the micron sized switches that will be assembled using Laser-Assisted Advanced Assembly method, the magnetic field needed to control the switches will drop even further which will be beneficial for applications such as embedding in metamaterials.

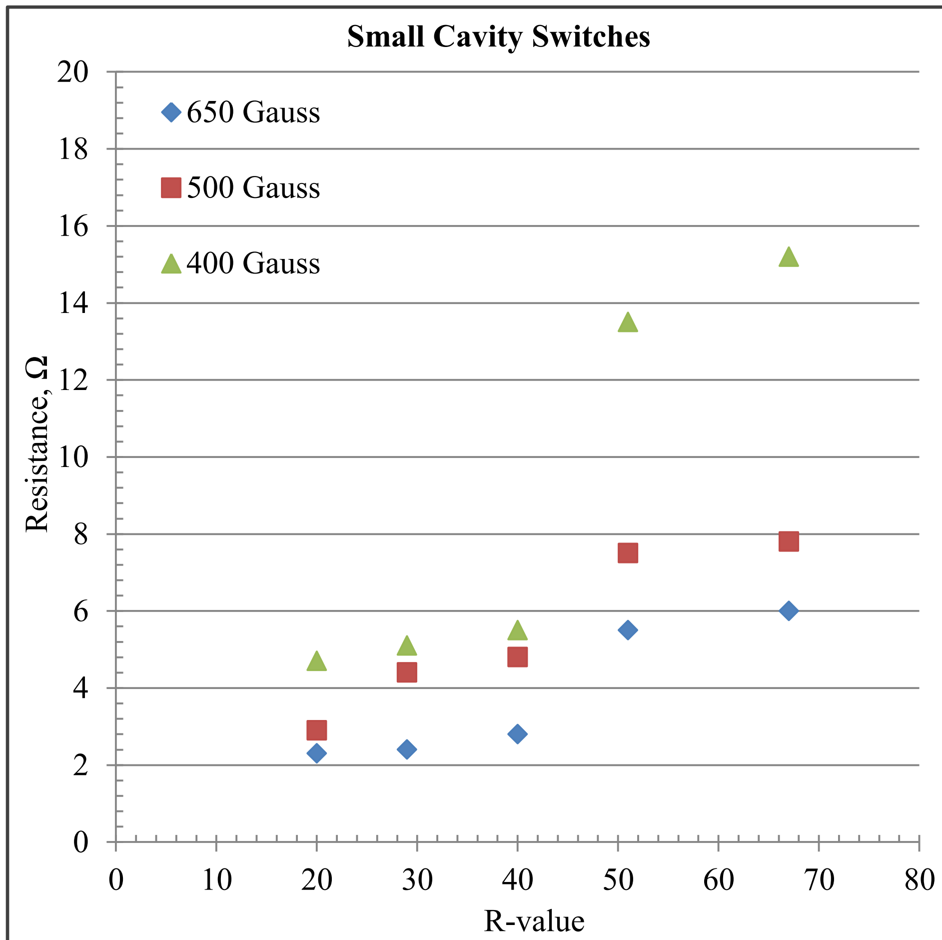

Figure 61. Resistance behavior of small cavity switches (cavity height of 125 μm) as a function of R-value for different magnetic field strength.

5.5. Laser-Assisted Advanced Assembly (LA^3) of Magnetic Switches

The data and knowledge obtained during the two types of proof-of-concept experiments, i.e. for transfer of metal components using *tm*SLADT and magnetic switch prototype trials, were used in the subsequent assembly of micro magnetic switches and their testing which are described in more detail in the next sections of this document.

The switch assembly using LA^3 was done following the process outlined earlier and taking into consideration the limitations described previously.

5.5.1. Substrate and switch cavity fabrication

The starting material for the switch substrate was the Novaclad® G2300 halogen-free copper polyimide laminate from Sheldahl Technical Materials. The material was chosen as it was readily available and is engineered for use in tough environments such as high temperatures and chemical exposure. In addition, Sheldahl's proprietary deposition process uses no adhesives and polyimide is readily micro-machined by the 355nm laser that we have in our component transfer set-up. The dielectric layer thickness of the material used was 180 μm and it was Cu-cladded with a 17 μm metal deposit on each side. In order to remove the copper layer on one of the laminate surfaces, the opposite one was spun on with positive photoresist and the metal layer on the uncoated side was chemically etched using Transene APS-100 copper etchant. At this point the material was ready to be used as a substrate to micro-machine the switches cavities.

For fabrication of the micro magnetic switches using laser assisted assembly, a two-step cavity design was adopted. A schematic cross section of the cavity is shown in Figure 62. The idea behind this design variation is to reduce the possibility of an unintentional closing of the switch if it is tilted on its side after embedding in the metamaterial and during operation. Another change in the cavity was the use of a square rather than a round cross-sectional area. This was

adopted as it was easier to program the laser to micro machine a square two-step blind via hole in the substrate material rather than a round one. These geometrical changes in cavity should not and cannot lead to changes in the switch performance and functionality.

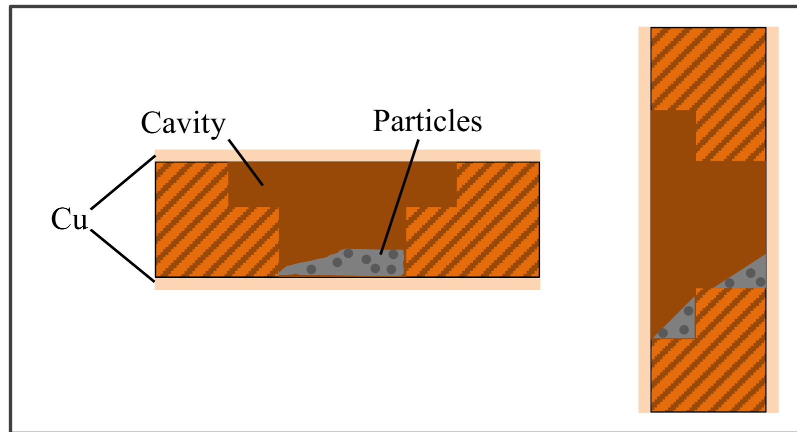

Figure 62. Schematic of two-step laser micro-machined cavity design; tipped on its side (*right*).

The switch cavities were produced by direct laser micromachining using the same Nd:YVO_4 laser and equipment that is later used for component transfers. The substrate is placed directly on the XY stage vacuum chuck and the laser focus is adjusted. Power is calibrated in the beginning or every time the repetition rate or diode current is changed. The laser parameters used for fabrication are shown in Table 6. These parameters result in very slow copper layer removal so the metal layer essentially acts as an ablation stop.

Table 6. Laser parameters used for receiving substrate micromachining

Cavity step	Size, µm	# of passes	Power, mW	Rep. rate, kHz	Diode, %	Wavelength, nm	Beam profile
Step 1	900 x 900	20	370	15	100	355	Gaussian
Step 2	700 x 700	48					

Figure 63 shows the resulting cross-section of a switch cavity made using the number of laser beam passes shown in Table 5. As seen in the figure the ratio of step one to step two is about 1.5 to 1, which should be sufficient to prevent accidental switch closing. The red dotted line is the profile obtained from the contact profilometer (KLA Tencor P-11) while the green solid line is the actual side wall shape. The difference is due to the contact stylus shape and as seen in the graph the actual walls produced are almost vertical.

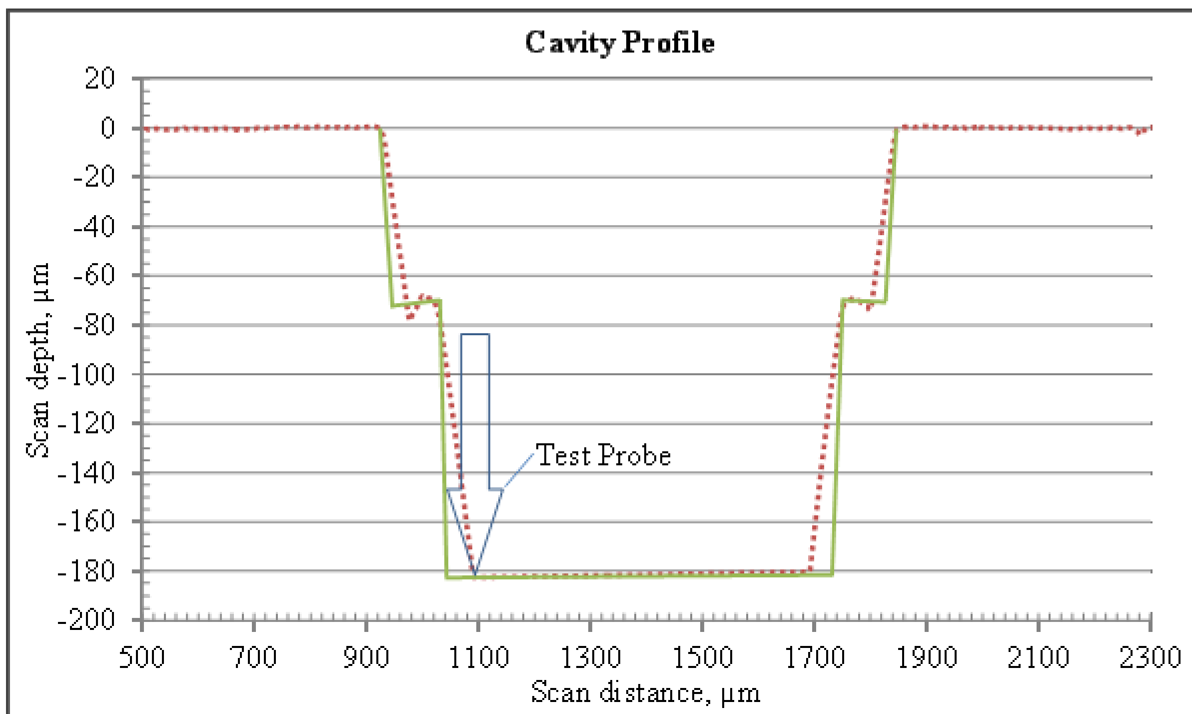

Figure 63. Finished cavity cross section obtained with a contact profilometer.

The cavities were made in sets of five by five matrixes with a fixed 4 mm step size in both x- and y-directions, which would allow aligning only once for the transfer of the whole set of top contact "caps" for a given matrix. The features on all 25 cavities, including aligning marks as seen in Figure 67, of a matrix were micro-machined from start to finish without disturbing the

substrate to avoid losing the initial datum point established. Alignment marks are simply three concentric circles produced by one laser pass each.

After machining, the substrates were placed in an ultrasonic cleaner for 3 minutes in order to remove any residue left from the laser and dried. After the assembly of the first batch of micro switches it was discovered that some polyimide residue is still present on the contact surfaces (Figure 64). The result of these polyimide traces lead to:

1. Higher than expected resistance values.
2. No repeatability in subsequent measurements of the same switch using the same conditions.
3. Sensitivity to position under the magnets, i.e. very small changes in position were leading to very large differences in behavior.
4. A very long time to achieve steady resistance values.
5. No significant drop in resistance with increase in the magnetic field strength or the amount of particles present.

Based on the above observations, a plasma cleaning step was introduced after the ultrasonic cleaning in order to remove the remaining polyimide residuals from the contact surface. This helped to alleviate the problems just described.

Finally, the Ni-coated magnetic particles suspended in isopropyl alcohol (IPA) solution are manually dispensed in each cavity under an optical microscope using an AccuPet Pro pipette that can dispense amounts as small as 0.3 μl. The IPA is left to evaporate before assembly and the receiving substrate is ready for laser-assisted assembly at this point (Figure 65).

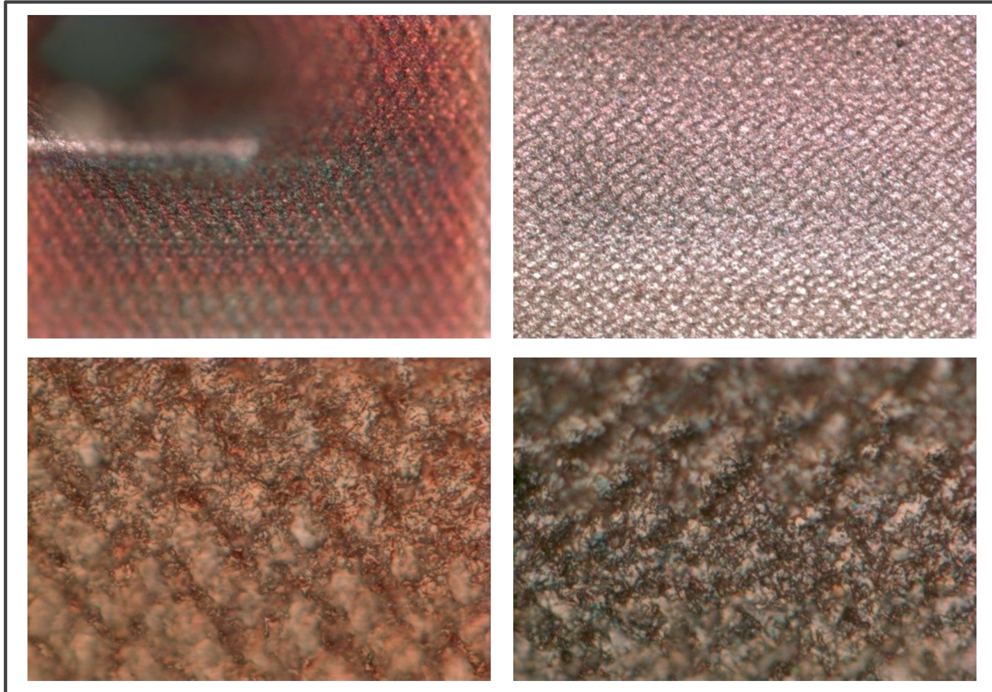

Figure 64. Contact surface of receiving substrate cavity pre- (*left*) and post- (*right*) plasma cleaning; 20X magnification (*top*) and 100X magnification (*bottom*).

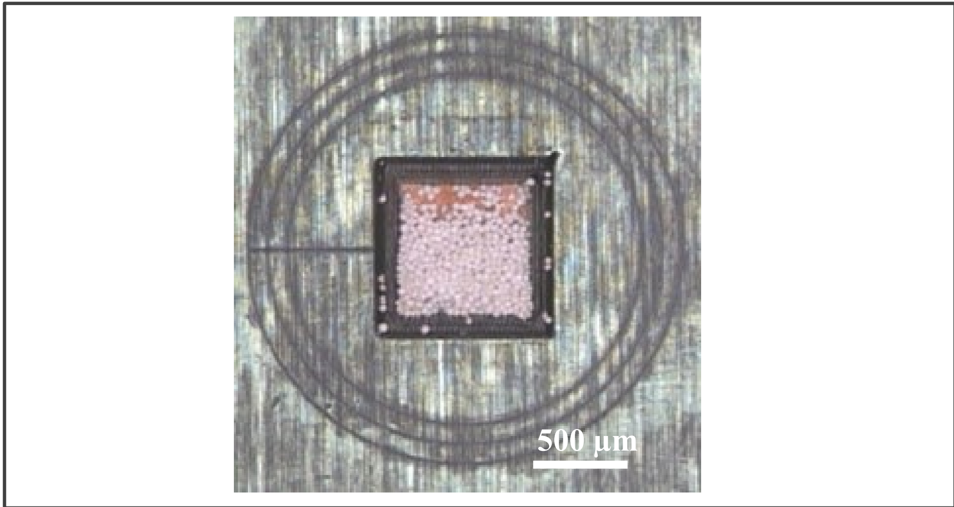

Figure 65. Top view of a micro-machined cavity partially filled with Ni-coated magnetic particles; the three consecutive rings are marks used for aligning before laser transfer.

Since the volume of these micro switch cavities is very small, no R-value could be assigned to each switch. That is due to the fact that the exact amount of particles dispensed in each cavity could not be measured because their mass is smaller than the resolution limit of the electronic scale used to measure the dispensed amount when the prototype switches were made. Instead, images of all filled cavities were taken (Figure 65) in order to be able to help in making conclusions based on the resistance measurement and switch behavior results obtained later. Some estimates of the R-values can later be made if needed by comparing the micro switches performance to their macro counter parts tested earlier as well as the images taken.

5.5.2. Sample for transfer preparation

The laser transparent carrier substrate and the Dynamic Release Layer formulation and processing parameters for these experiments were exactly the same as in previous work performed for transfer of silicon and metal components and will not be repeated here. The difference is in the preparation of the magnetic switch top contacts and it will be shown in more details in this section.

The starting material for preparation of the top contacts or "caps" for the laser assembled magnetic switches was 25.4 mm (1 inch) wide copper tape from 3M. The thickness of the copper film is 25µm and total thickness with adhesive is 66 µm. The tape is supplied on a paper lining with measured thickness of 120 µm. Before the start of the sample preparation a one inch square is cut from the tape and rolled with a roller to flatten it. The flattened square is then pressed between heavy metal plates overnight followed by stretching of the laminate over a glass slide in order to minimize tape handling.

Preparation of the tape samples was started by cutting circles with a diameter of 2 mm in the paper backing by direct laser micromachining. Those circles were cut following the same

five by five matrix with 4 mm step size in both x- and y-directions. As mentioned earlier, this would allow aligning a group of 23 switches at the same time. Next, those circles were carefully removed with a sharp tungsten probe exposing the adhesive layer. The purpose of this was to leave paper material to act as spacing between the adhesive layer and the plate used to apply pressure to the foil material in the next step. The Cu tape sample was placed onto the adhesive layer of the DRL and pressure was applied using weight overnight.

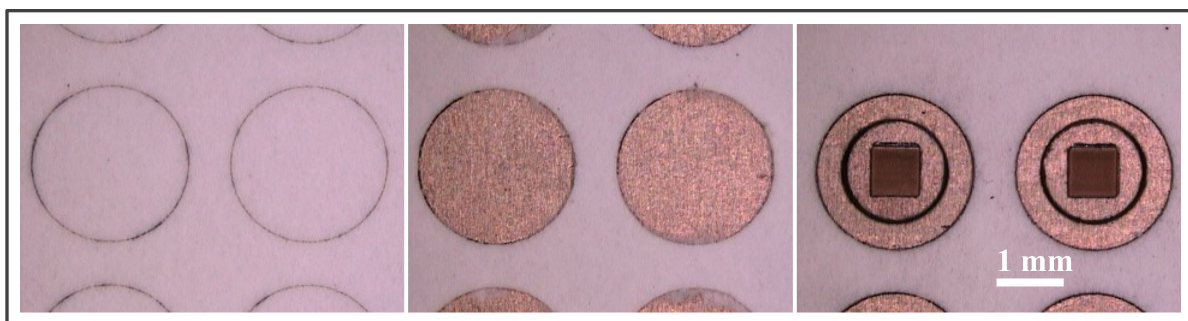

Figure 66. Steps in copper tape preparation for “caps” fabrication.

After the tape is applied to the DRL, the pattern of circles is aligned on the laser XY stage in both directions using the vision system of the laser. After alignment an area of 1 mm x 1 mm square of the adhesive is removed in the middle of each exposed circle to create the contact area. The area is slightly larger than the corresponding area on the cavity in order to account for the precision of transfer and to avoid or at least minimize adhesive penetrating the cavity. Finally a circle with a diameter of 1.5 mm is ablated through the adhesive and copper foil using the laser again (Figure 66). Laser parameters used in these steps are shown in Table 7. At the end the sample is plasma cleaned to remove any traces of adhesive left on the contact surface. The carrier sample is ready for alignment and transfer using *tm*SLADT at this point.

Table 7. Laser parameters used for carrier substrate micromachining

Material/Feature	Power, mW	# of passes	Rep. Rate, kHz	Diode, %	Beam profile	Wavelength, nm
Adhesive removal	600	6	50	80	Gaussian	355
Copper cap micromachining	700	300				

5.5.3. Laser transfer and assembly

After the receiving and carrier substrates are prepared they are each placed in the alignment device shown in Figure 67. The device consists of a frame with four very fine thread pitch screws on each side. The receiving substrate placed on a rectangular glass slide is positioned on top of the smaller frame seen within the bigger one in the left part of the figure below. The bottom screws are used to adjust translation and rotation of the receiving substrate. The 3 inch fused silica disc with the carrier substrate facing down is placed in the top plate which is seen on the right side of Figure 67; the transparent disc is secured with collar and screws. The top plate also has a 200 µm thick lip machined around the circumference of the opening which gives the transfer gap after subtracting the carrier substrate thickness; in this case the transfer gap is 134 µm. The top screws of the outside frame are used for translation and rotation of the carrier substrate plate. The total translation and rotation adjustment that each of the inner plates provide are 20 mm in both x- and y-direction and 8 degrees each for a total of 16 degrees, respectively.

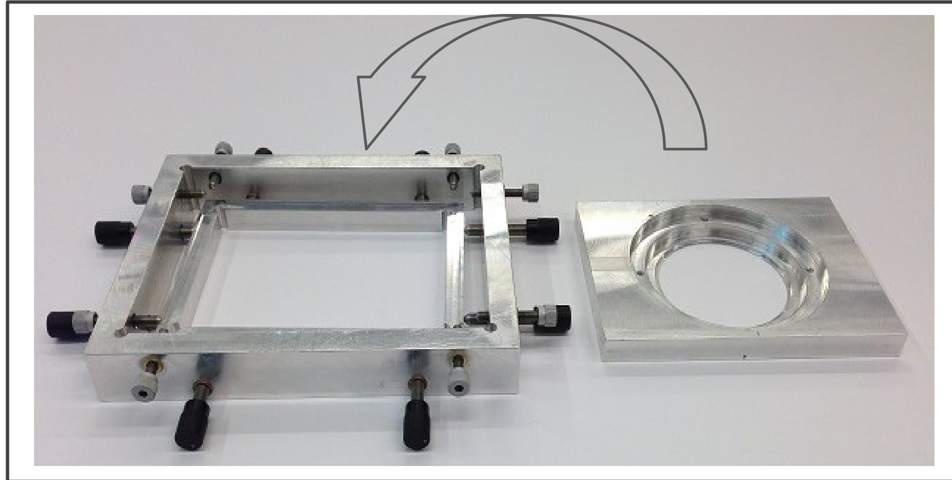

Figure 67. Alignment device for laser transfer of components.

Figure 68 shows a schematic representation of the alignment procedure. First, two diagonal caps are manually removed from the carrier substrate which has already been mounted in the top alignment plate. The top plate is positioned over the receiving substrate which is placed approximately in the middle of the glass slide. Next, the screws are used to align the vacancies from the removed caps with the alignment marks (Figure 68) micro-machined in the receiving substrate around the switch cavities. This fine alignment is done under an optical microscope.

After completing the alignment steps as described above, the fixture is moved onto the XY stage of the laser system and the laser beam is focused at the polyimide-glass interface of the DRL carrier. A schematic of the experimental set-up is shown in Figure 69.

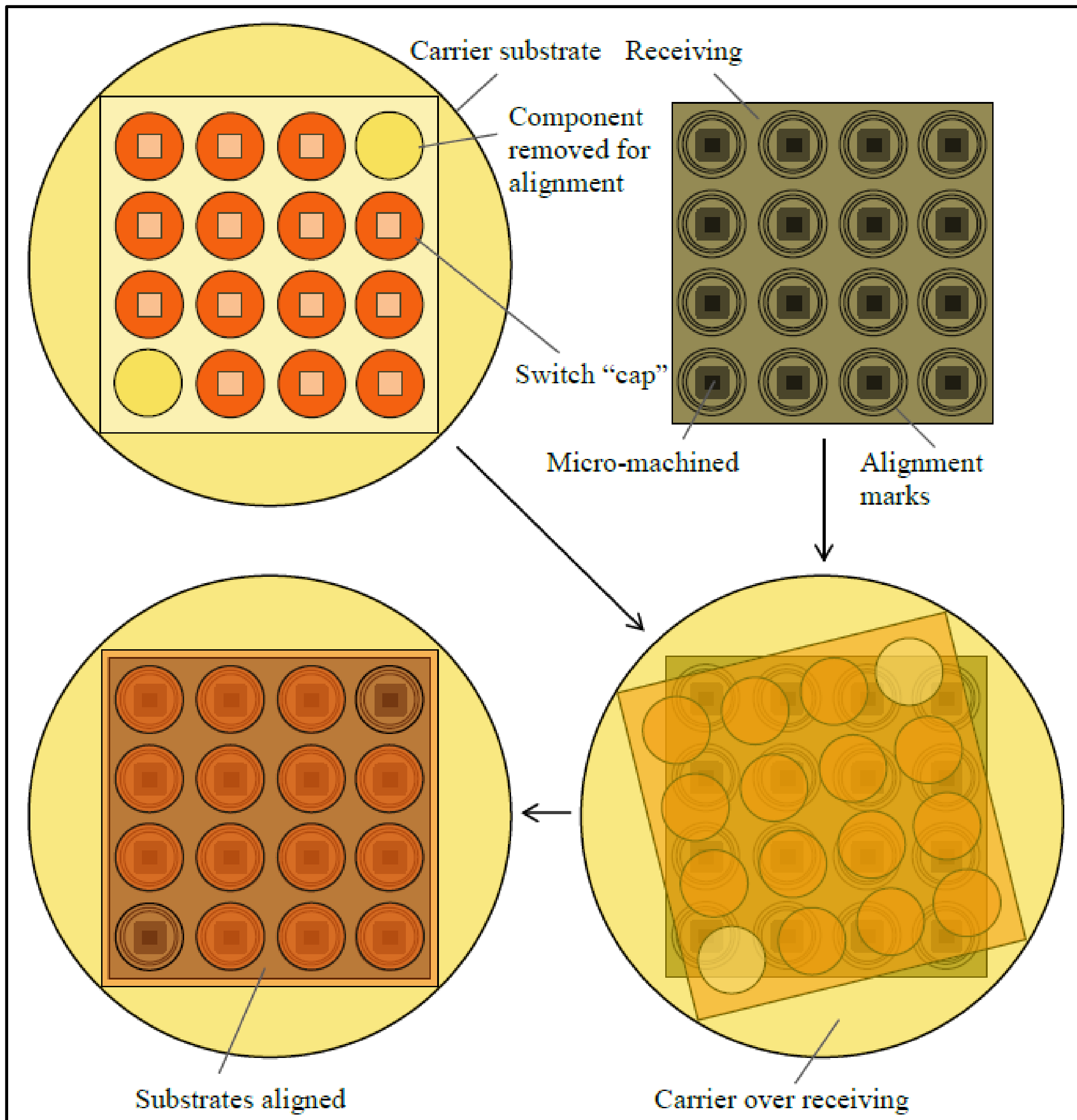

Figure 68. Schematic of substrate alignment.

Prior to each use, a power meter is placed after the laser beam scanner to calibrate the beam power versus waveplate position. The waveplate is mounted in a rotational stage and a Labview® interface is used to control its angular position and from there the power of the laser beam received at the sample. Once the power curve is obtained a fine focus adjustment of the laser beam needs to be performed in order to achieve optimal transfer conditions. In order to find

the focus z-height of the XYZ stage, a polyimide sample such as a piece of Kapton® sheet is irradiated with scribe lines. The height of the stage is changed by a predetermined step size before each scribe line is produced. The smaller the spread between minimum and maximum z-height and the finer the step size is, the more precise is the alignment achieved. The focus height of the stage, or laser beam waist location, is the height at which the thinnest line is ablated on the polyimide sample. After power calibration and fine focus adjustment, the *tm*SLADT sample in the fixture is placed on the motion control stages and the sample position is set, along the axis of the beam, so the beam waist is in the same plane as the polyimide layer of the sample. Scribe lines produced with this set-up in a silicon wafer during previous experiments indicate that a flat top beam waist diameter of 10 μm can be achieved.

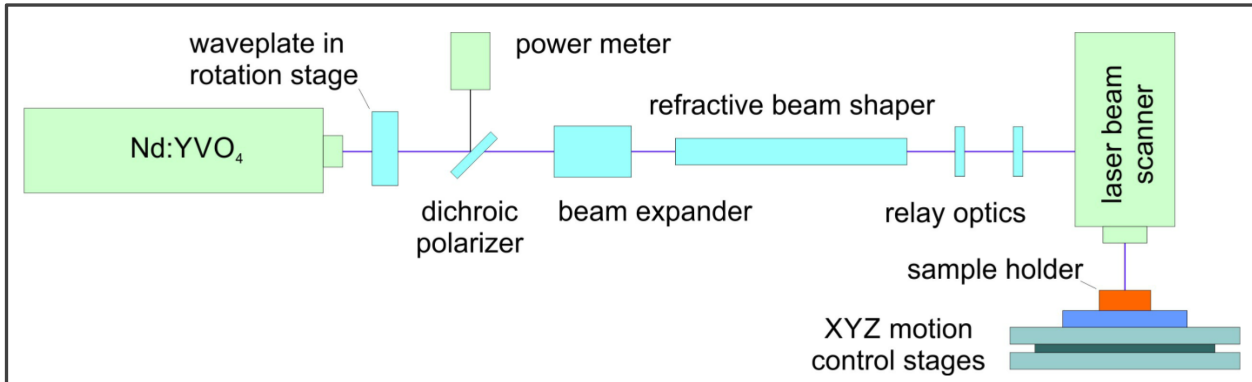

Figure 69. Experimental set-up for Laser-Assisted Advanced Assembly [104].

The laser transfer process needs a top hat profile of the optical beam in order to spread the energy across a larger beam area and to allow irradiation of the polyimide layer without blister rupturing. The image in Figure 70 is a still from the BeamGAUGE program that is used to monitor and adjust the beam shape and intensity profile prior to laser transfer. The top hat profile is produced by the refractive beam shaper, which is otherwise not used in previous

micromachining steps. A pair of relay lenses maintains the uniformity of the top hat beam profile [102] while guiding it to the laser beam scanner (SCANLAB HurryScan® II) which is positioned on a gantry mount and directs the optical beam toward the XYZ stage.

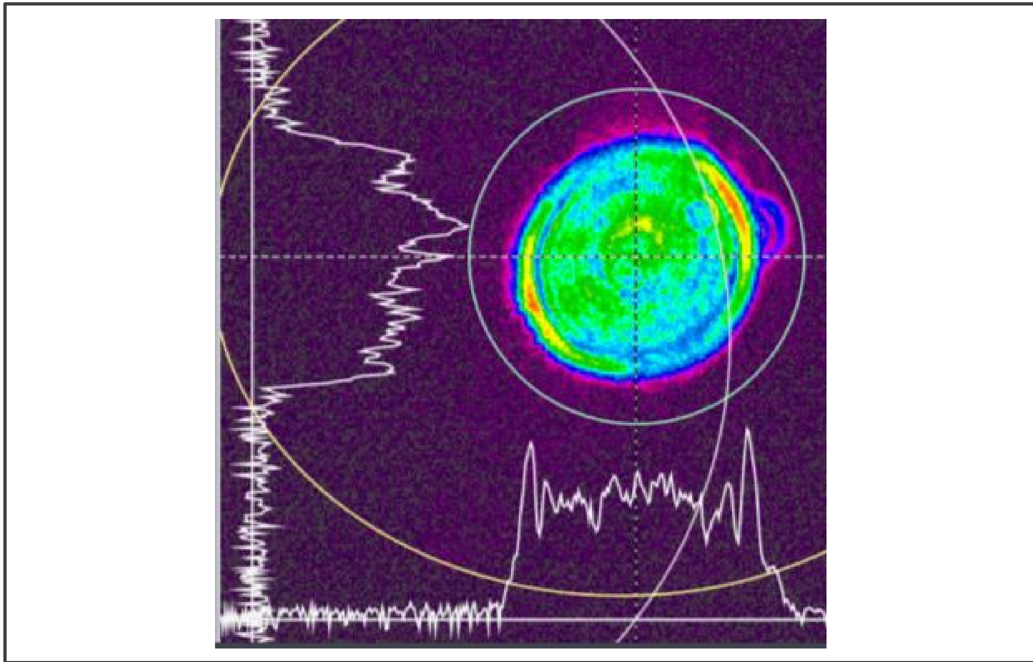

Figure 70. Laser beam top hat profile used in *tm*SLADT. The profile is captured before the beam waist where the optical beam exits the scanhead [102].

The laser transfer was carried out using the Spectra Physics HIPPO Nd:YVO_4 laser whose third harmonic beam (355 nm) passes through a variable attenuator which is a half wave-plate dichroic polarizer. All the steps descibed so far are schematically illustarted in a simplified way in Figure 71. The Dynamic Release Layer was scanned with the three concentric circle pattern described previously using a laser scan speed of 400 mm/second, repetition rate of 15 kHz, and maximum power of 0.46W. The power used was somewhat higher than usual due to the size of the components and in some cases resulted in partial blister rupture. However, this blister rupture did not seem to affect the precision to a great extent, as shown in the next section,

possibly due to the relatively small 2:1 transfer gap to component thickness ratio as well as the size and mass of the components and the presence of adhesive, which does not allow translational sliding or rotation upon contact with the receiving substrate.

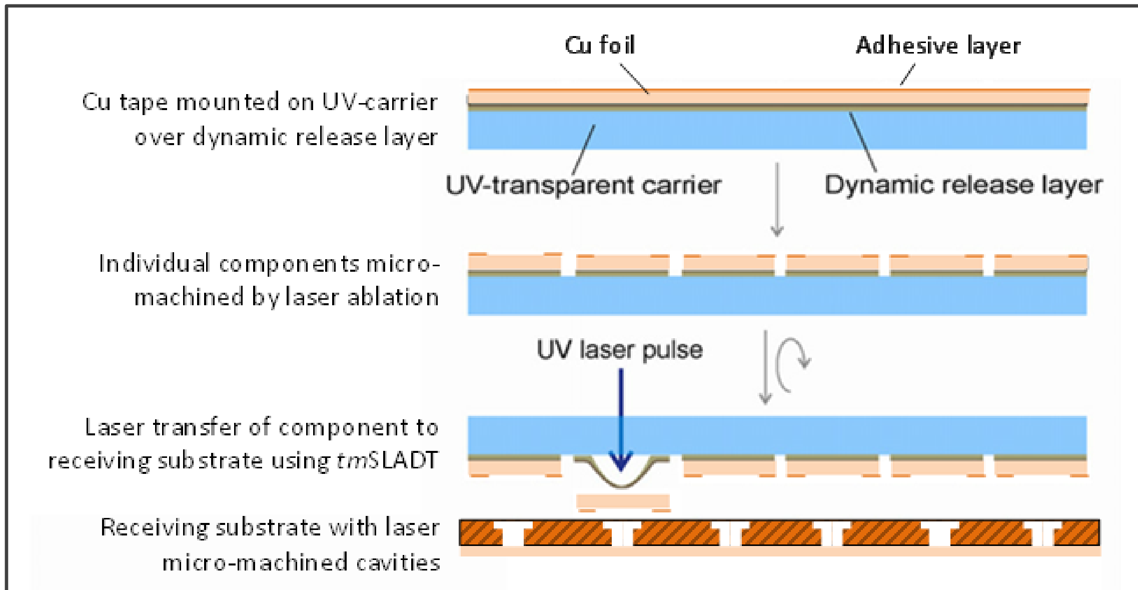

Figure 71. Main steps in magnetic switch fabrication and assembly by Laser-Assisted Advanced Assembly.

5.5.4. Precision of transfer

As discussed earlier the fabrication and transfer and assembly process described in the preceding sections was repeated twice because the first switches assembled showed unsatisfactory resistance and behavior results. Nonetheless, the transfer rate in this first attempt was 19 successful transfers out of 23 attempted or 82.3%; only 23 transfers can be attempted on a single matrix of five by five components because two diagonal ones are removed manually for alignment. Precision of transfer for this first assembly was not measured.

The second assembly of micro-switches that included plasma cleaning steps for receiving and carrier substrates prior to laser-assisted transfer, resulted in 21 successful out of 23 attempted

transfers or 91.3%. The transfer rate results compare well for those obtained in prior experiments for manipulation of metal and silicon components with optimized parameters.

The transfer precision was measured using an Optical Gauging Products (OGP) SmartScope Flash 200 system that provides a resolution of 1 μm. Figure 72 shows the program interface used in measurement. Because the center of the cavity is hidden from view and in order to find the center of the intended landing position of the cap, the alignment marks are used. The cross hair of the software interface is positioned over one end of an alignment mark and this point is established as a datum point. Next, the actual alignment mark diameter is measured and the cross-hair is brought back to one-half the value obtained. The same procedure is repeated in the other direction without disturbing the already acquired diameter. These two steps establish the center of the cavity or the desired landing spot for the center of the cap. In the next step the distances from that spot to the ends of the transferred component are measured; half of the difference between the two provides the translation in the direction measured. The procedure is repeated in the other direction and the results are recorded in a spreadsheet.

Figure 73 shows graphically the actual landing position of every component transferred relative to the ideal one. The average precision obtained for all components measured was 34.4 μm in the x-direction and 27.3 μm in the y-direction, which translates the total deviation from the ideal landing position of 43.9 μm. This result is about two to three times poorer than the precision obtained in transfer of silicon components presented earlier, but there is an additional error introduced in these last transfers by the alignment step. Although the precision obtained was somewhat lower, the accuracy of the results obtained is very good when the components size is taken into account as seen in the insert of Figure 73.

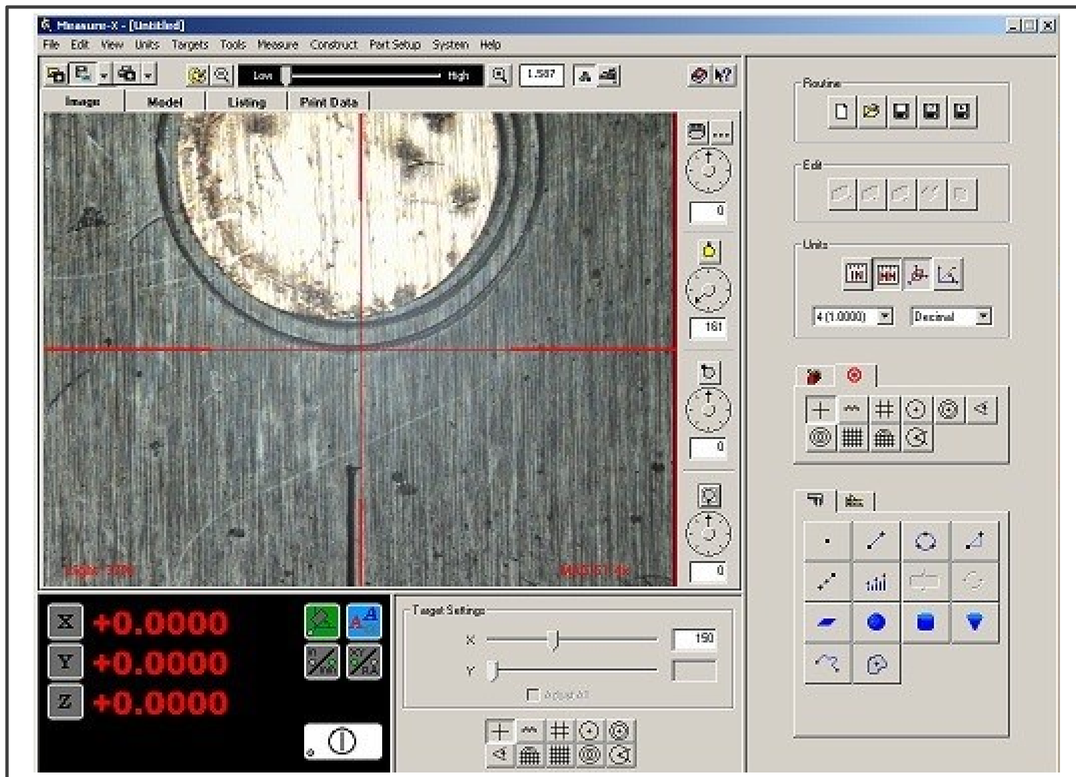

Figure 72. Measuring precision of transfer with OGP Flash 200 system.

The contribution of the aligning step cannot be readily predicted or measured at this point, but it is definitely a major factor. A second reason contributing to the lower precision may be the fact that the blistering layer characteristics such as thickness and cure times as well as adhesive layer strength have been previously optimized for smaller components made of a different material. Additional effects may have occurred during the indirect measurement approach employed and described in the preceding paragraph.

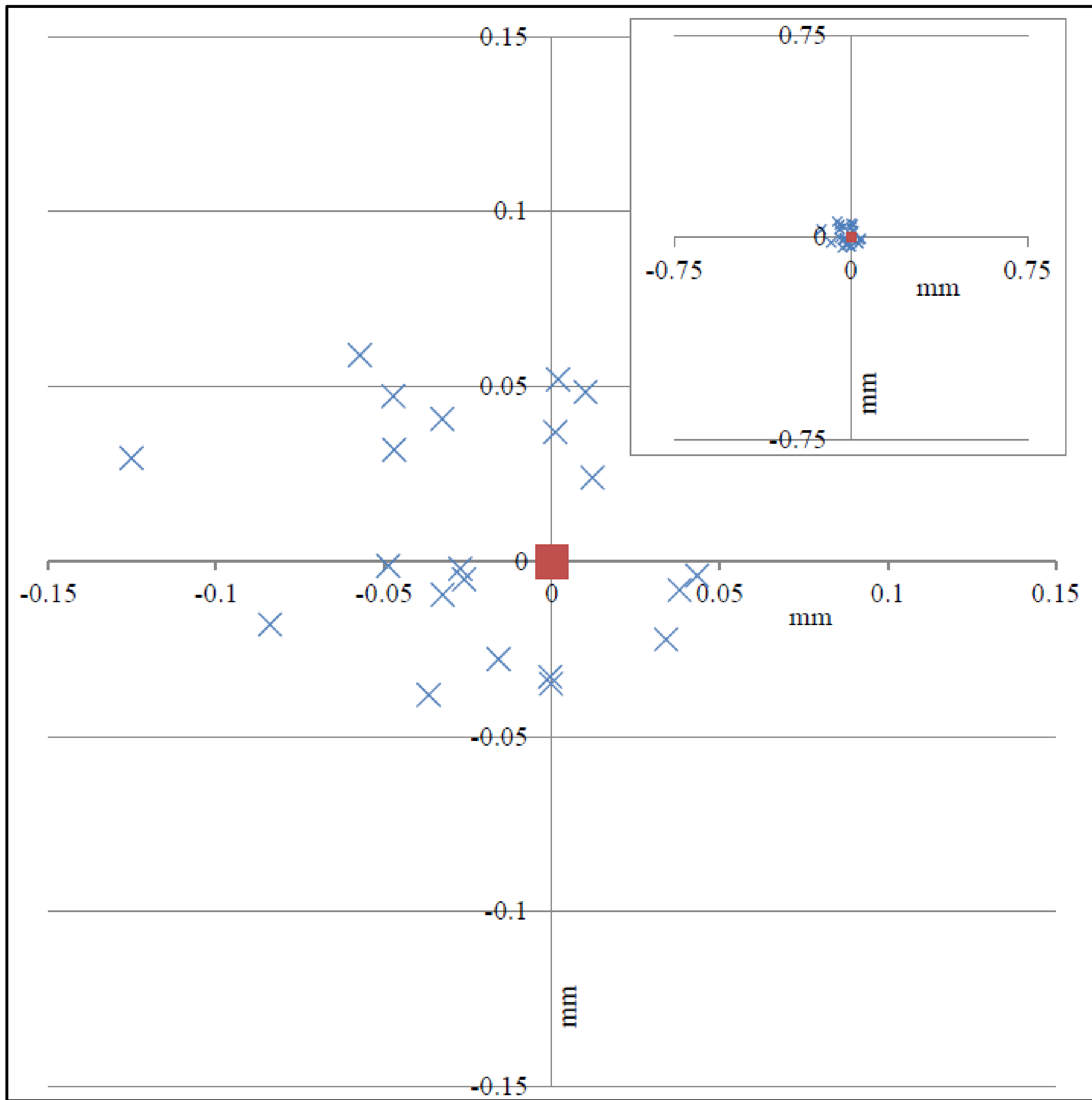

Figure 73. Precision of transfer for laser-assembled switch top contacts; the red square is the position of the center of a perfect transfer, the blue cross-hairs shows the actual position of the center of each cap transferred. The scale for both graphs is in mm.

Due to the oversight in cap design, i.e. a circular shape, rotational precision could not be measured for all components transferred. Traces of blister rupture were found on eight of the final devices and the rotation was measured using the OGP tool software as shown in Figure 74.

The average value obtained was 2.26^{o} and all but one of the components exhibited counter clockwise rotation, which is the direction in which the laser scans the three circle pattern in the blistering layer.

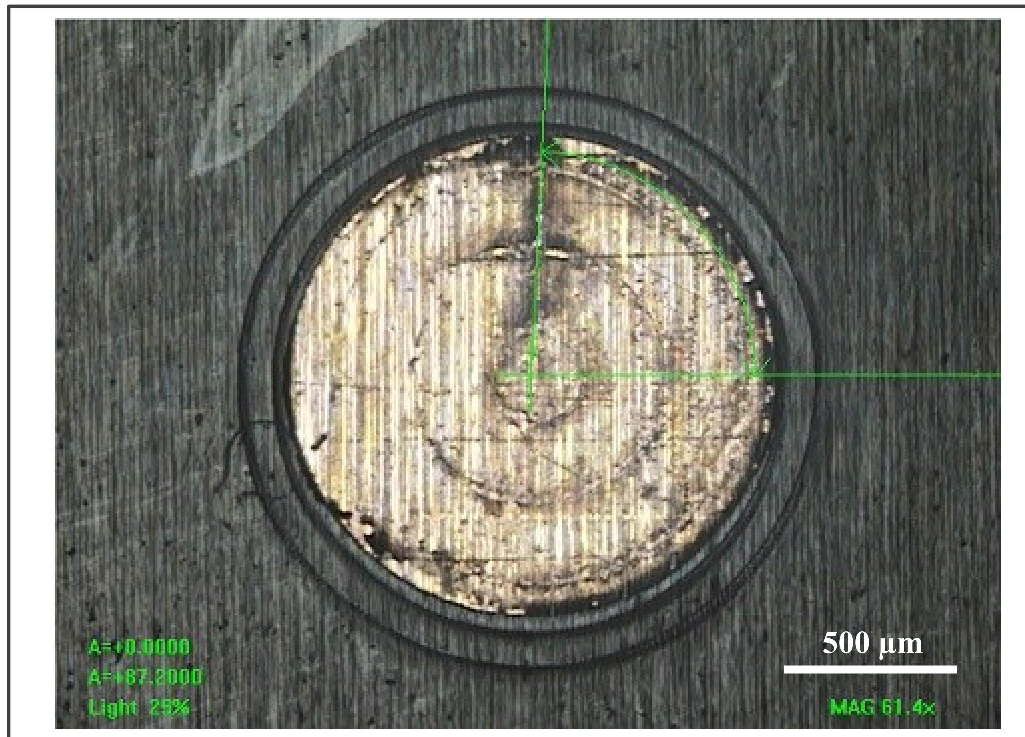

Figure 74. Measurement of rotation for transferred top contacts.

5.6. Switch Functionality Testing

The functionality of the laser assembled magnetically actuated micro switches was measured in a manner similar to the measurements of their macro counterparts presented earlier. The resistance between bottom and top contact surfaces was measured using fine tungsten probes before the individual switches were singulated from the receiving substrate; one probe contacts the top switch directly, while the second one touches the bottom surface through a micromachined via hole in the polyimide substrate. This setup allows measuring all 21 switches by moving only the top probe to the next switch and placing it in the magnetic field. Getting to

the bottom surface of an individual switch for testing after singulation will be impossible due to the small size. Top contact surfaces were carefully cleaned from traces of adhesive and blister layer materials left before resistance measurements. Resistance measurements were done for magnetic field strengths varying from 300 to 1100 Gauss and the average values obtained are graphically presented in Figure 75 and important values tabulated in Table 8.

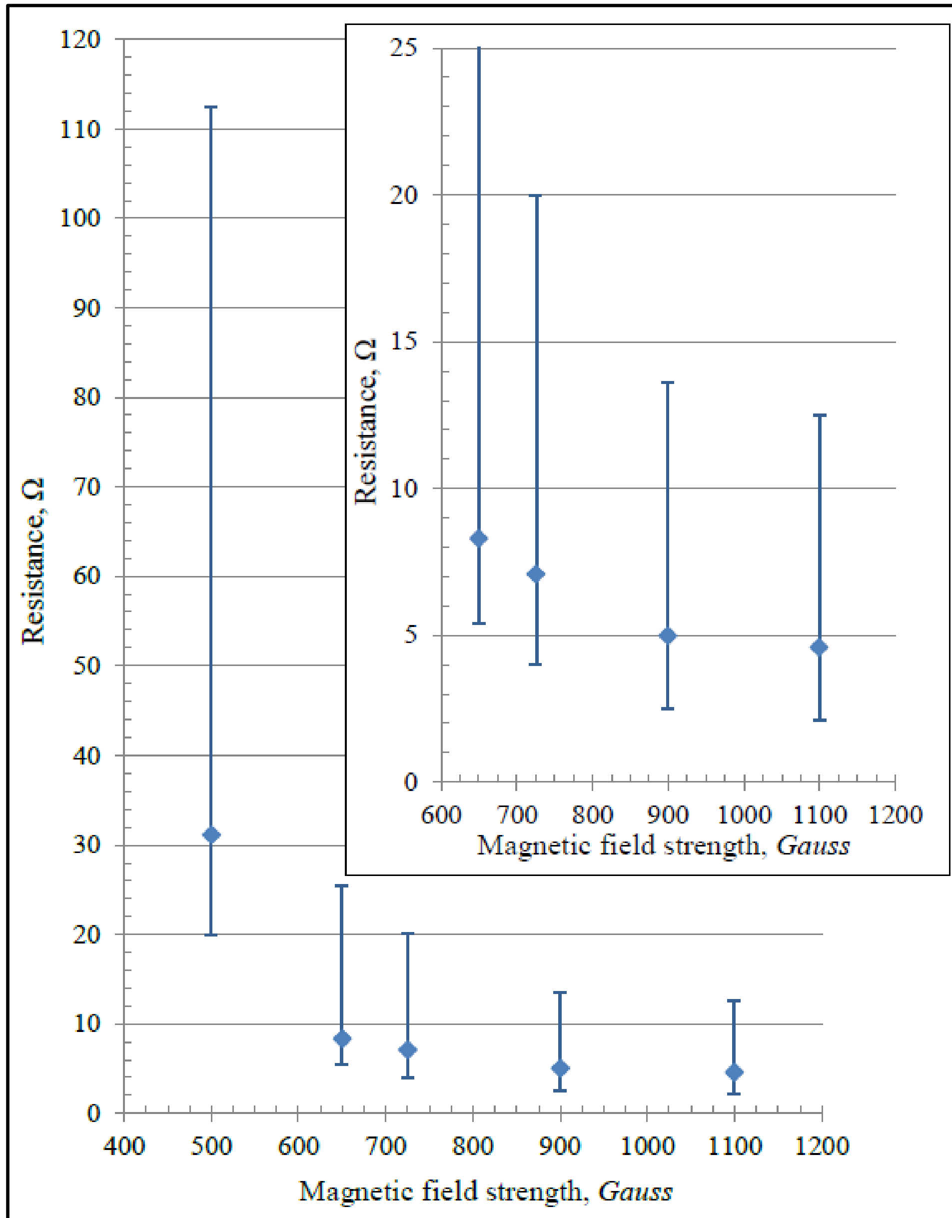

Figure 75. Average resistance values for all 21 switches assembled by Laser-Assisted Advanced Assembly method. Insert is a close-up view.

Table 8. Switch resistance values for laser assembled micro switches

Resistance parameter:	Magnetic field strength, *Gauss*					
	300	500	650	725	900	1100
Average, Ω	45.7	31.1	8.3	7.1	5.0	4.6
Standard deviation, Ω	21.3	19.1	3.4	2.4	1.7	1.5
Minimum, Ω	17.5	11.2	2.9	3.1	2.5	2.5
Maximum, Ω	kΩ	81.4	17.2	12.9	8.6	7.9

As seen from the figure and table above, the switches behave in the presence of a magnetic field as expected based on the preliminary experiment. The resistance values drop exponentially with an increase of the magnetic field and tend to level-off as the field strength reaches higher values. What is not observed in the performance of the laser assembled micro switches is an additional scaling effect. Based on the performance of their large and small macro counterparts it was expected to see further reduction in the lower range of the strength of the magnetic field required to activate them as well as possible further reduction in resistance values. However, the absence of an additional scaling effect should be contributed to the materials and methods used in the fabrication step rather than the assembly step that relied on Laser-Assisted Advanced Assembly technique as discussed next.

First, the average resistance values for all 21 switches assembled is somewhat higher than the expected based on scaling effects, but this is average for all different R-values resulting from the different amount of particles dispensed. As mentioned earlier, with the micron sized cavity used in these devices, measurement of the amount of particles dispensed became impossible with conventional methods. Consequently, the amount of particles was dispensed randomly. It is therefore possible that some of the switches have an R-value higher than 67,

which is the highest R-value used in the small “macro” devices (Figure 76). What is the exact mix of R-values within all 21 switches cannot be determined with certainty at present.

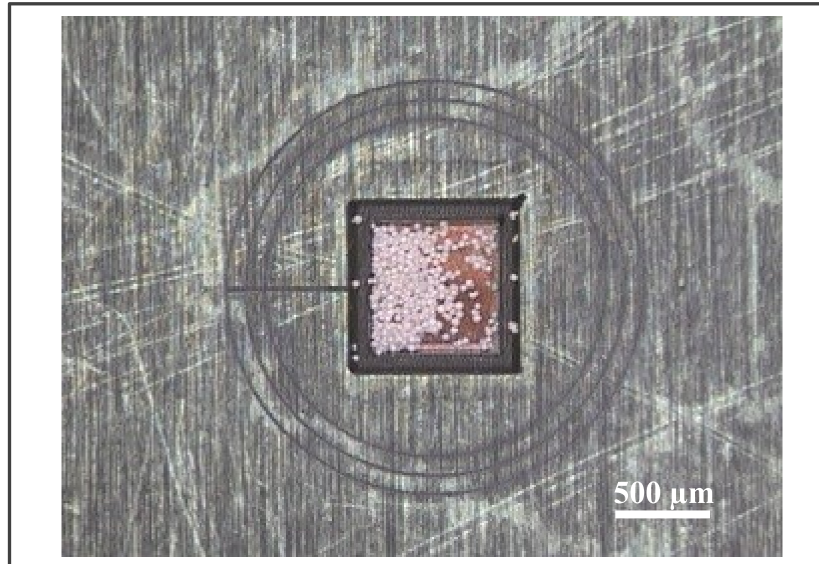

Figure 76. Switch with possible very large R-value.

A second and more important reason that may have led to the observed lack of additional scaling effects and the overall similar if not poorer performance of the micro switches compared to the small macro counterparts (Table 9) is the use of laser micromachining to create the via-hole cavities and to remove adhesive from the caps.

As already discussed, one problem associated with that method of parts fabrication was the traces of polyimide left on the contact surfaces; this was addressed by using plasma cleaning after machining. Plasma cleaning, however, cannot address the issue of surface roughness. Laser micromachining, as any other material cutting operation, creates a particular lay on the surface produced and is capable of achieving a particular minimum surface roughness.

Table 9. Switch resistance for "small" macro switches

		Magnetic Field Strength, *Gauss*				
Sample	R-value	175	300	400	500	650
1	40	185	31.6	5.5	4.8	2.8
2	67	MΩ	KΩ	15.2	7.8	6
3	51	MΩ	KΩ	13.5	7.5	5.5
4	29	100	24.5	5.1	4.4	2.4
5	20	17.5	13.3	4.7	2.9	2.3
Average resistance, Ω		100.8	23.1	8.8	5.5	3.8
Standard deviation, Ω		83.8	9.2	5.1	2.1	1.8
Minimum, Ω		17.5	13.3	4.7	2.9	2.3
Maximum, Ω		MΩ	KΩ	15.2	7.8	6

The surface pattern left by the laser beam can be clearly seen in Figure 64 on page 126. Laser micromachining should be considered a secondary operation rather than a finishing one in the micron scale. In contrast, the copper foil used for the fabrication of the macro switches was employed as received. The difference in surface characteristic between the micromachined copper and the as received rolled copper foil can be seen in Table 10.

Table 10. Surface roughness of laser micromachined copper and copper foil

Roughness parameter	Copper foil	Laser micromachined copper
Average roughness, Ra, µm	0.151	0.669
maxRa, µm	0.165	0.952
Maximum peak height, Rp, µm	0.455	2.68
Maximum valley depth, Rv, µm	0.524	1.94

Surface roughness measurements were taken with a KLA Tencor P-11 contact profilometer and the topography of the surfaces and their likely contact interface with the Ni coated magnetic particles are shown in Figure 77. Based on the average particle size and the topography of the copper contact faces it can be seen that the lower surface roughness and especially the lower surface roughness peak height and valley depth, lead to larger area contact patches in the case of as received copper foil than in micromachined copper. Hence, the laser-assisted transfer method used to assemble the components of the micron-sized magnetic switch devices does not play a negative role in their performance.

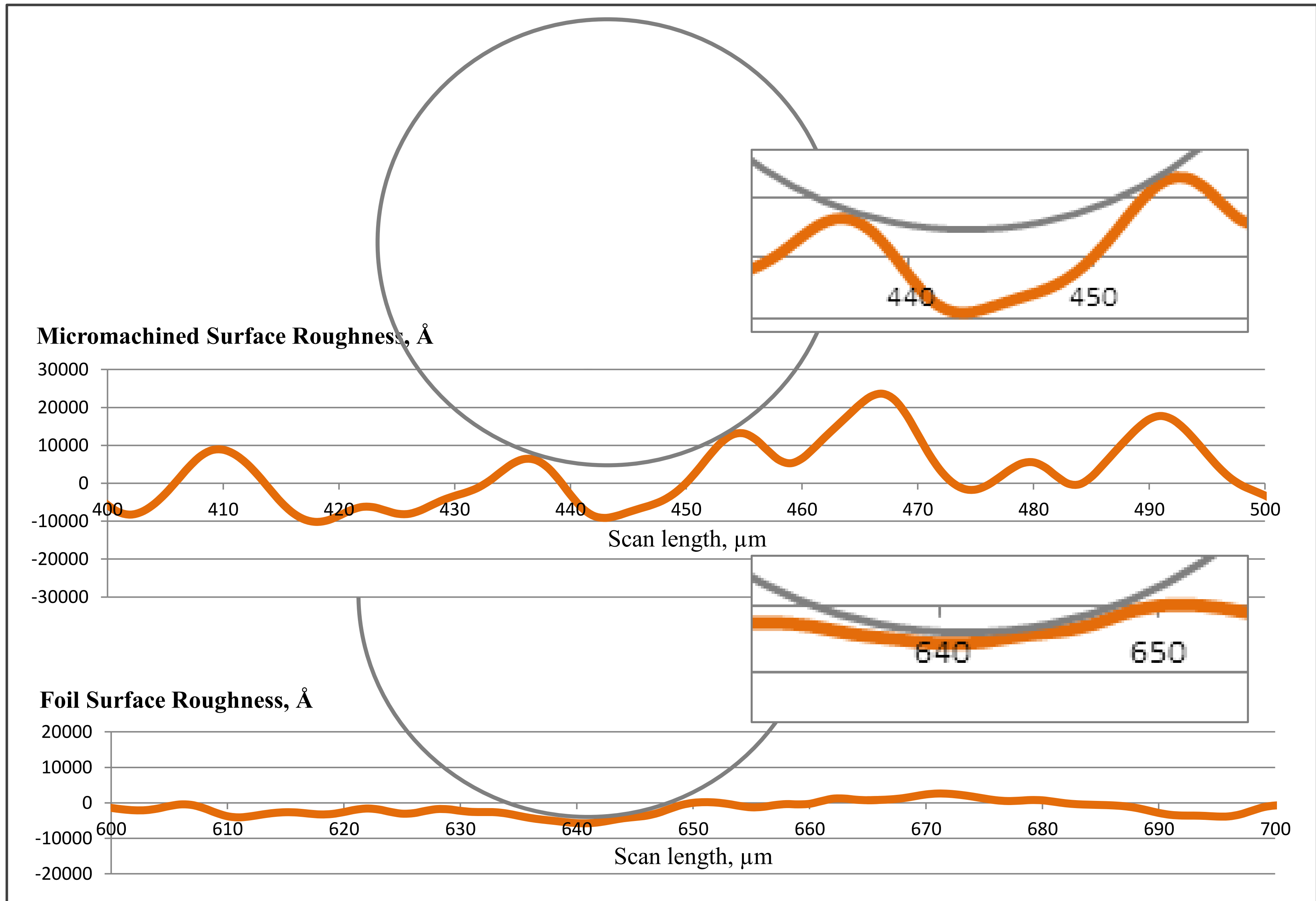

Figure 77. Surface roughness and contact patch (*inserts*) of laser micro-machined copper (*top*) and copper foil (*bottom*).

CHAPTER 6. CONCLUSIONS

- The thermo-mechanical Selective Laser Assisted Die Transfer (*tm*SLADT) mechanism for laser propulsion of small components developed at the Center for Nanoscale Science and Engineering at North Dakota State University has already been proven to provide precision and accuracy of placement bordering if not exceeding the traditional robotic pick-and-place manipulation techniques.
- The Laser Enabled Advanced Packaging process that benefits from all advantages offered by *tm*SLADT is a comprehensive wafer to finished product technology that has already been successfully demonstrated as a viable microelectronics packaging method by extensive studies and functional devices fabrication.
- The effort presented in this document is the first demonstration of a modification of LEAP for fabrication, manipulation, and assembly of individual components for MEMS device production titled Laser-Assisted Advanced Assembly (LA^3).
- The results show once again that the transfer rate and precision of *tm*SLADT as a laser propulsion method for components transfer and assembly are independent of size and geometry in the upper micron and mesoscale range.
- As shown by the latest experimental work the rate and precision of transfer are also independent of the material manipulated (Si, Al, Cu, etc.) expanding the number of materials that can be used in MEMS fabrication.
- The starting material for LA^3 can be any material available in thin-sheet stock, including prior material treatments such as volumetric and surface heat treatment, tribological and biocompatible coatings, surface modifications, biofunctinalization,

and more, in the manufacturing of MEMS devices enhancing their structural, mechanical, and functional properties.

- Laser-Assisted Advanced Assembly and Laser Enabled Advanced Packaging allow fabrication and assembly of not only the mechanical, but also the electronic parts of a MEMS device.
- All these benefits will ultimately help to increase the design complexity and functionality of MEMS devices and therefore expand their application areas and markets penetration.

CHAPTER 7. FUTURE WORK

The most important outcome of the work presented is the possibility for further research in the areas of laser propulsion for micro components and laser-assisted manipulation and assembly of parts for MEMS device fabrication. A great number of questions arose during this research endeavor and although many of them were addressed and answered, an even larger number remain open for impending investigation. Future research that can be performed based on the outcomes of this experimental work includes, but is not limited to

- Further optimization of Dynamic Release Layer blistering and adhesive layer materials to increase day-to-day transfer rate and precision repeatability.
- Modelling of the DRL response to laser irradiation. This would potentially allow varying the blister layer thickness and adhesive strength for optimal results for different component size ranges.
- Modelling and study of the interaction of the laser optical beam with the blistering layer to increase understanding of blister formation and component release mechanisms.
- Investigate the effects of using different types of lasers, i.e. wavelength and especially single pulse laser interactions, on blister formation and transfer dynamics to determine the most suitable type of laser for transfer of components using the thermo-mechanical propulsion mechanism.
- Detailed study of transfer dynamics including release mechanism, initial velocity, velocity on impact, limits of component survivability, and behavior through air gap and the effects of laser power on precision, accuracy , and survivability.

- Study on the limits of component sizes that can be manipulated, both lower and upper, based on particular DRL formulations and laser parameters used and establish relationships between the critical parameters.
- Further investigation of available interconnecting and joining techniques for both electrical and mechanical components.
- Overall process optimization for realization in commercial applications.

BIBLIOGRAPHY

1. Wikipedia. (July 2013). *Metamaterial*. Available: en.wikipeadia.org/wiki/Metamaterial

2. S. Miller, "Lighter, stronger, more affordable: Darpa's quests in the realm of materials science," *DARPA: 50 Years of Bridging the Gap,* pp. 128-33, 2008.

3. A. Sihvola, "Metamaterials in electromagnetics," *Metamaterials,* vol. 1, pp. 2-11, 2007.

4. V. M. Shalaev, "Optical negative-index metamaterials," *Nature photonics,* vol. 1, pp. 41-48, 2007.

5. J. Valentine, S. Zhang, T. Zentgraf, E. Ulin-Avila, D. A. Genov, G. Bartal, and X. Zhang, "Three-dimensional optical metamaterial with a negative refractive index," *nature,* vol. 455, pp. 376-379, 2008.

6. M. N. Exchange. (December 2013). *What is MEMS Technology*. Available: https://www.memsnet.org/about/what-is.html

7. C. Liu. (2010, 18 Feb. 2014). *The Art of MEMS*. Available: http://www.memscentral.com/overview_of_mems.htm

8. J. Bryzek, "Roadmap to a $ Trillion MEMS Market," in *10th Annual MEMS Technology Symposium*, 2012.

9. Plasma-Therm, "Current Trends with DRIE/DSE Processing for MEMS Devices and Structures," Plasma-Therm2012.

10. M. B. Cohn, K. F. Boehringer, J. M. Noworolski, A. Singh, C. G. Keller, K. A. Goldberg, and R. T. Howe, "Microassembly technologies for MEMS," in *Micromachining and Microfabrication*, 1998, pp. 2-16.

11. U. Srinivasan, M. A. Helmbrecht, R. S. Muller, and R. T. Howe, "MEMS: Some self-assembly required," *Optics and Photonics News,* vol. 13, pp. 20-24, 2002.

12. A. S. Holmes, "Laser fabrication and assembly processes for MEMS," in *Photonics West 2001-LASE*, 2001, pp. 297-306.

13. A. Lai, T. Itoh, and C. Caloz, "Composite right/left-handed transmission line metamaterials," *Microwave Magazine, IEEE,* vol. 5, pp. 34-50, 2004.

14. H. Tao, A. C. Strikwerda, K. Fan, W. J. Padilla, X. Zhang, and R. D. Averitt, "MEMS based structurally tunable metamaterials at terahertz frequencies," *Journal of Infrared, Millimeter, and Terahertz Waves,* vol. 32, pp. 580-595, 2011.

15. A. A. Houck, J. B. Brock, and I. L. Chuang, "Experimental observations of a left-handed material that obeys Snell's law," *Physical Review Letters,* vol. 90, p. 137401, 2003.

16. R. A. Shelby, D. R. Smith, and S. Schultz, "Experimental verification of a negative index of refraction," *science,* vol. 292, pp. 77-79, 2001.

17. D. E. Anagnostou, G. Zheng, M. T. Chryssomallis, J. C. Lyke, G. E. Ponchak, J. Papapolymerou, and C. G. Christodoulou, "Design, fabrication, and measurements of an RF-MEMS-based self-similar reconfigurable antenna," *Antennas and Propagation, IEEE Transactions on,* vol. 54, pp. 422-432, 2006.

18. I. Gil, M. Morata, R. Fernández-Garcıa, X. Rottenberg, and W. De Raedt, "Reconfigurable RF-MEMS metamaterials filters," *Session 3A9,* p. 750, 2011.

19. D. Langley, E. A. Moore, R. A. Coutu Jr, and P. J. Collins, "MEMS integrated metamaterials with variable resonance operating at RF frequencies," in *MEMS and Nanotechnology, Volume 4*, ed: Springer, 2011, pp. 159-166.

20. M. Huff, "MEMS fabrication," *Sensor Review,* vol. 22, pp. 18-33, 2002.

21. P. S. Waggoner and H. G. Craighead, "Micro-and nanomechanical sensors for environmental, chemical, and biological detection," *Lab on a Chip,* vol. 7, pp. 1238-1255, 2007.

22. A. Hars, "Wafer Leaders Extend Basis for Global SOI Supply," in *Advanced Substrate News* vol. 2014, A. Hars, Ed., ed, 2012.

23. G. T. Reed and A. P. Knights, *Silicon photonics*: Wiley Online Library, 2008.

24. F. Marty, L. Rousseau, B. Saadany, B. Mercier, O. Français, Y. Mita, and T. Bourouina, "Advanced etching of silicon based on deep reactive ion etching for silicon high aspect ratio microstructures and three-dimensional micro-and nanostructures," *Microelectronics journal,* vol. 36, pp. 673-677, 2005.

25. K. Owen, B. VanDerElzen, R. Peterson, and K. Najafi, "High aspect ratio deep silicon etching," *MEMS'12,* pp. 251-254, 2012.

26. Wikipedia. (March 2014). *LIGA*. Available: http://en.wikipedia.org/wiki/LIGA

27. A. M. Tools. (April 2014). *Hydrofluoric Acid Vapor Etcher*. Available: http://www.ammt.com/products/hydrofluoric-acid-vapor-etcher/

28. U. o. Cincinnati. (April 2014). *Electro Discharge Machining*. Available: http://www.min.uc.edu/ucman/research/electrical-discharge-machining

29. C. Volkert and A. Minor, "Focused ion beam microscopy and micromachining," *MRS bulletin,* vol. 32, pp. 389-399, 2007.

30. Wikipedia. (April 2014). *Focused Ion Beam*. Available: http://en.wikipedia.org/wiki/File:Principe_FIB.jpg

31. F. Ay, K. Wörhoff, R. M. de Ridder, and M. Pollnau, "Focused-ion-beam nanostructuring of Al2O3 dielectric layers for photonic applications," *Journal of Micromechanics and Microengineering,* vol. 22, p. 105008, 2012.

32. R. S. Fearing, "Survey of sticking effects for micro parts handling," in *Intelligent Robots and Systems 95.'Human Robot Interaction and Cooperative Robots', Proceedings. 1995 IEEE/RSJ International Conference on*, 1995, pp. 212-217.

33. U. Srinivasan, D. Liepmann, and R. T. Howe, "Microstructure to substrate self-assembly using capillary forces," *Microelectromechanical Systems, Journal of,* vol. 10, pp. 17-24, 2001.

34. H. J. J. Yeh and J. S. Smith, "Fluidic self-assembly for the integration of GaAs light-emitting diodes on Si substrates," *Photonics Technology Letters, IEEE,* vol. 6, pp. 706-708, 1994.

35. H. Noda and M. Usami, "0.075× 0.075 mm 2 ultra-small 7.5 μm ultra-thin RFID-chip mounting technology," in *Electronic Components and Technology Conference, 2008. ECTC 2008. 58th*, 2008, pp. 366-370.

36. J. Govaerts, W. Christiaens, E. Bosman, and J. Vanfleteren, "Fabrication processes for embedding thin chips in flat flexible substrates," *Advanced Packaging, IEEE Transactions on,* vol. 32, pp. 77-83, 2009.

37. F. Iker, D. Tezcan, R. Teixeira, P. Soussan, P. De Moor, E. Beyne, and K. Baert, "3D Embedding and Interconnection of Ultra Thin (≪ 20 μm) Silicon Dies," in *Electronics Packaging Technology Conference, 2007. EPTC 2007. 9th*, 2007, pp. 222-226.

38. R. Das, "Chip versus chipless for RFID applications," in *ACM International Conference Proceeding Series*, 2005, pp. 23-26.

39. R. Dekker, M. Dumling, J.-H. Fock, O. Gourhant, C. Jonville, T. Michielsen, H. Pohlmann, W. Schnitt, and A. Tombeur, "A 10 µm thick RF-ID tag for chip-in-paper applications," in *Bipolar/BiCMOS Circuits and Technology Meeting, 2005. Proceedings of the*, 2005, pp. 18-21.

40. V. R. Marinov, O. Swenson, Y. Atanasov, and N. Schneck, "Laser-assisted ultrathin bare die packaging: a route to a new class of microelectronic devices," in *SPIE LASE*, 2013, pp. 86080L-86080L-19.

41. J. C. Miller and R. F. Haglund, "Laser Ablation Mechanisms and Applications," in *Laser Ablation Mechanisms and Applications*, 1991.

42. L. Lucas and J. Zhang. (2012). *Femtosecond laser micromachining: A back-to-basics primer Social Media Tools*.

43. M. Gower, "Excimer lasers: principles of operation and equipment," in *Laser Processing in Manufacturing*, ed: Springer, 1993, pp. 163-187.

44. R. Pethig, J. Burt, A. Parton, N. Rizvi, M. Talary, and J. Tame, "Development of biofactory-on-a-chip technology using excimer laser micromachining," *Journal of Micromechanics and Microengineering,* vol. 8, p. 57, 1998.

45. J. Li and G. Ananthasuresh, "A quality study on the excimer laser micromachining of electro-thermal-compliant micro devices," *Journal of Micromechanics and microengineering,* vol. 11, p. 38, 2001.

46. W. Pfleging, A. Ludwig, K. Seemann, R. Preu, H. Mäckel, and S. Glunz, "Laser micromachining for applications in thin film technology," *Applied surface science,* vol. 154, pp. 633-639, 2000.

47. A. S. Holmes, "Laser processes for MEMS manufacture," in *Second International Symposium on Laser Precision Micromachining*, 2002, pp. 203-209.

48. C. Rowan, "Excimer lasers drill precise holes with higher yield," *Laser Focus World,* August 1995.

49. J. Arnold, U. Dasbach, W. Ehrfeld, K. Hesch, and H. Löwe, "Combination of excimer laser micromachining and replication processes suited for large scale production," *Applied Surface Science,* vol. 86, pp. 251-258, 1995.

50. R. Lawes, A. Holmes, and F. Goodall, "The formation of moulds for 3D microstructures using excimer laser ablation," *Microsystem technologies,* vol. 3, pp. 17-19, 1996.

51. M. Alonso-Amigo and W. Röpke, "Laser ablation/hot embossing in plastic microfabrication," in *Proc. ICALO*, 2000, pp. D10-15.

52. A. Braun, K. Zimmer, B. Hösselbarth, J. Meinhardt, F. Bigl, and R. Mehnert, "Excimer laser micromachining and replication of 3D optical surfaces," *Applied surface science,* vol. 127, pp. 911-914, 1998.

53. A. Holmes, S. Saidam, and R. Lawes, "Low-cost LIGA processes," in *COLLOQUIUM DIGEST-IEE*, 1997, pp. 2-2.

54. H. Ota, T. Oda, and M. Kobayashi, "Development of coil winding process for radial gap type electromagnetic micro-rotating machine," in *Micro Electro Mechanical Systems, 1995, MEMS'95, Proceedings. IEEE*, 1995, p. 197.

55. D. Bäuerle, *Chemical processing with lasers*: Springer, 1986.

56. G. T. Kovacs, N. I. Maluf, and K. E. Petersen, "Bulk micromachining of silicon," *Proceedings of the IEEE,* vol. 86, pp. 1536-1551, 1998.

57. M. Mullenborn, H. Dirac, J. Petersen, and S. Bouwstra, "Fast 3D laser micromachining of silicon for micromechanical and microfluidic applications," in *Solid-State Sensors and Actuators, 1995 and Eurosensors IX.. Transducers' 95. The 8th International Conference on*, 1995, pp. 166-169.

58. M. Müllenborn, F. Grey, and S. Bouwstra, "Laser direct writing on structured substrates," *Journal of Micromechanics and Microengineering,* vol. 7, p. 125, 1997.

59. D. o. A. Physiscs. (March 2014). *Pulsed Laser Deposition*. Available: http://physics.aalto.fi/groups/nanospin/facilities/pulsed-laser-deposition/

60. K. Ikuta, M. Hayashi, T. Matsuura, and H. Fujishiro, "Shape memory alloy thin film fabricated by laser ablation," in *Micro Electro Mechanical Systems, 1994, MEMS'94, Proceedings, IEEE Workshop on*, 1994, pp. 355-360.

61. R. Maeda, K. M. Kikuchi, A. Schroth, A. Umezawa, and S. Matsumoto, "Deposition of PZT thin films by pulsed laser ablation for MEMS application," in *Far East and Pacific Rim Symposium on Smart Materials, Structures, and MEMS*, 1997, pp. 372-379.

62. J. Robertson, "Diamond-like amorphous carbon," *Materials Science and Engineering: R: Reports,* vol. 37, pp. 129-281, 2002.

63. S. Allen, "Laser chemical vapor deposition: A technique for selective area deposition," *Journal of Applied Physics,* vol. 52, pp. 6501-6505, 1981.

64. M. C. Wanke, O. Lehmann, K. Müller, Q. Wen, and M. Stuke, "Laser rapid prototyping of photonic band-gap microstructures," *Science,* vol. 275, pp. 1284-1286, 1997.

65. E. Makino and T. Shibata, "Micromachining compatible metal patterning technique using localized decomposition of an organometallic compound by laser irradiation," *Journal of Micromechanics and Microengineering,* vol. 8, p. 177, 1998.

66. M. Renn and B. King, "Laser guided direct writing of electronic components," in *Proc. ICALEO*, 2000, pp. D46-50.

67. K. Ikuta and K. Hirowatari, "Real three dimensional micro fabrication using stereo lithography and metal molding," in *Micro Electro Mechanical Systems, 1993, MEMS'93, Proceedings An Investigation of Micro Structures, Sensors, Actuators, Machines and Systems. IEEE.*, 1993, pp. 42-47.

68. K. Ikuta, K. Hirowatari, and T. Ogata, "Three dimensional micro integrated fluid systems (MIFS) fabricated by stereo lithography," in *Micro Electro Mechanical Systems, 1994, MEMS'94, Proceedings, IEEE Workshop on*, 1994, pp. 1-6.

69. K. Ikuta, S. Maruo, Y. Fukaya, and T. Fujisawa, "Biochemical IC chip toward cell free DNA protein synthesis," in *Micro Electro Mechanical Systems, 1998. MEMS 98. Proceedings., The Eleventh Annual International Workshop on*, 1998, pp. 131-136.

70. K. Ikuta, S. Maruo, and S. Kojima, "New micro stereo lithography for freely movable 3D micro structure-super IH process with submicron resolution," in *Micro Electro Mechanical Systems, 1998. MEMS 98. Proceedings., The Eleventh Annual International Workshop on*, 1998, pp. 290-295.

71. A. Bertsch, H. Lorenz, and P. Renaud, "3D microfabrication by combining microstereolithography and thick resist UV lithography," *Sensors and Actuators A: Physical,* vol. 73, pp. 14-23, 1999.

72. A. S. Holmes, S. M. Saidam, and C. Wang, "Laser-Assisted Assembly for Hybrid Microelectromechanical Systems," *Laser Microfabrication,* pp. 1-9, 2000.

73. R. S. Muller and K. Y. Lau, "Surface-micromachined microoptical elements and systems," *Proceedings of the IEEE,* vol. 86, pp. 1705-1720, 1998.

74. G. K. Fedder and R. T. Howe, "Thermal assembly of polysilicon microstructures," in *Micro Electro Mechanical Systems, 1991, MEMS'91, Proceedings. An Investigation of Micro Structures, Sensors, Actuators, Machines and Robots. IEEE*, 1991, pp. 63-68.

75. M. Geiger, W. Becker, and F. Vollertsen, "Microbending and precision straightening by pulsed UV laser radiation," *Laser und Optoelektronik,* vol. 29, pp. 67-75, 1997.

76. R. R. Syms, "Surface tension powered self-assembly of 3-D micro-optomechanical structures," 1999.

77. A. S. Holmes and S. M. Saidam, "Sacrificial layer process with laser-driven release for batch assembly operations," *Microelectromechanical Systems, Journal of,* vol. 7, pp. 416-422, 1998.

78. K.-P. Kamper, J. Dopper, W. Ehrfeld, and S. Oberbeck, "A self-filling low-cost membrane micropump," in *Micro Electro Mechanical Systems, 1998. MEMS 98. Proceedings., The Eleventh Annual International Workshop on*, 1998, pp. 432-437.

79. I. Miyamoto, A. Horn, J. Gottmann, D. Wortmann, and F. Yoshino, "Fusion welding of glass using femtosecond laser pulses with high-repetition rates," *Zvaranie/Svarovani,* vol. 60, pp. 59-66, 2011.

80. T. Tamaki, W. Watanabe, J. Nishii, and K. Itoh, "Welding of transparent materials using femtosecond laser pulses," *Japanese journal of applied physics,* vol. 44, p. L687, 2005.

81. C. Wang and A. S. Holmes, "Laser-assisted bumping for flip chip assembly," *Electronics Packaging Manufacturing, IEEE Transactions on,* vol. 24, pp. 109-114, 2001.

82. N. Karlitskaya, *Laser die transfer: laser-induced transfer of microcomponents*: University of Twente, 2011.

83. N. S. Karlitskaya, J. Meijer, D. F. de Lange, and H. Kettelarij, "Laser propulsion of microelectronic components: releasing mechanism investigation," in *High-Power Laser Ablation 2006*, 2006, pp. 62612P-62612P-10.

84. N. S. Karlitskaya, D. F. de Lange, R. Sanders, and J. Meijer, "Study of laser die release by Q-switched Nd: YAG laser pulses," in *High-Power Laser Ablation 2004*, 2004, pp. 935-943.

85. A. Piqué, H. Kim, and C. B. Arnold, "Laser forward transfer of electronic and power generating materials," in *Laser Ablation and Its Applications*, ed: Springer, 2007, pp. 339-373.

86. S. A. Mathews, R. C. Auyeung, and A. Piqué, "Use of laser direct-write in microelectronics assembly," *Journal of Laser Micro/Nanoengineering,* vol. 2, pp. 103-107, 2007.

87. A. Piqué, B. Pratap, S. A. Mathews, B. J. Karns, R. C. Auyeung, M. Kasser, M. Ollinger, H. Kim, S. Lakeou, and C. B. Arnold, "Laser direct-write of embedded electronic components and circuits," in *Lasers and Applications in Science and Engineering*, 2005, pp. 223-230.

88. J. R. Sheats, "Printing silicon integrated circuits," in *In Proc. of Printed Electronics USA*, San Hose, CA, 2008.

89. M. Feil, C. Adler, D. Hemmetzberger, M. Konig, and K. Bock, "The challenge of ultra thin chip assembly," in *Electronic Components and Technology Conference, 2004. Proceedings. 54th*, 2004, pp. 35-40.

90. A. Piqué, S. Mathews, B. Pratap, R. Auyeung, B. Karns, and S. Lakeou, "Embedding electronic circuits by laser direct-write," *Microelectronic engineering,* vol. 83, pp. 2527-2533, 2006.

91. F. Arai, D. Andou, and T. Fukuda, "Adhesion forces reduction for micro manipulation based on micro physics," in *Micro Electro Mechanical Systems, 1996, MEMS'96, Proceedings. An Investigation of Micro Structures, Sensors, Actuators, Machines and Systems. IEEE, The Ninth Annual International Workshop on*, 1996, pp. 354-359.

92. M. Mastrangeli, S. Abbasi, C. Varel, C. Van Hoof, J.-P. Celis, and K. F. Böhringer, "Self-assembly from milli-to nanoscales: methods and applications," *Journal of micromechanics and microengineering,* vol. 19, p. 083001, 2009.

93. J. W. Balde, *3-D Assemblies of Stacked Chips and other Thin Packages*: Springer, 2003.

94. C. Banda, R. W. Johnson, T. Zhang, Z. Hou, and H. K. Charles, "Flip chip assembly of thinned silicon die on flex substrates," *Electronics Packaging Manufacturing, IEEE Transactions on,* vol. 31, pp. 1-8, 2008.

95. K. Y. Chen, R. L. Zenner, M. Ameson, and D. Mountain, "Ultra-thin electronic device package," *Advanced Packaging, IEEE Transactions on,* vol. 23, pp. 22-26, 2000.

96. B. Pahl, C. Kallmayer, R. Aschenbrenner, and H. Reichl, "Ultrathin assemblies on flexible substrates," in *Electronic Packaging Technology Conference, 2005. EPTC 2005. Proceedings of 7th*, 2005, p. 6 pp.

97. R. Fabbro, J. Fournier, P. Ballard, D. Devaux, and J. Virmont, "Physical study of laser-produced plasma in confined geometry," *Journal of Applied Physics,* vol. 68, pp. 775-784, 1990.

98. R. Griffin, B. Justus, A. Campillo, and L. Goldberg, "Interferometric studies of the pressure of a confined laser-heated plasma," *Journal of applied physics,* vol. 59, pp. 1968-1971, 1986.

99. A. Zweig and T. Deutsch, "Shock waves generated by confined XeCl excimer laser ablation of polyimide," *Applied Physics B,* vol. 54, pp. 76-82, 1992.

100. P. Dyer and J. Sidhu, "Excimer laser ablation and thermal coupling efficiency to polymer films," *Journal of applied physics,* vol. 57, pp. 1420-1422, 1985.

101. A. Pique, "Application of laser direct-write for embedding microelectronics," in *in Proc. of Advance Alser Technologies*, Brasov, Romania, 2006.

102. R. Miller, V. Marinov, O. Swenson, Z. Chen, and M. Semler, "Noncontact Selective Laser-Assisted Placement of Thinned Semiconductor Dice," *Components, Packaging and Manufacturing Technology, IEEE Transactions on,* vol. 2, pp. 971-978, 2012.

103. M. S. Brown, N. T. Kattamis, and C. B. Arnold, "Time-resolved study of polyimide absorption layers for blister-actuated laser-induced forward transfer," *Journal of Applied Physics,* vol. 107, p. 083103, 2010.

104. V. R. Marinov, O. Swenson, Y. Atanasov, and N. Schneck, "Laser-assisted ultrathin die packaging: Insights from a process study," *Microelectronic Engineering,* vol. 101, pp. 23-30, 2013.

105. V. Marinov, O. Swenson, R. Miller, F. Sarwar, Y. Atanasov, M. Semler, and S. Datta, "Laser-enabled advanced packaging of ultrathin bare dice in flexible substrates," *Components, Packaging and Manufacturing Technology, IEEE Transactions on,* vol. 2, pp. 569-577, 2012.

106. J. Chen and I. De Wolf, "Study of damage and stress induced by backgrinding in Si wafers," *Semiconductor Science and Technology,* vol. 18, p. 261, 2003.

107. Z. Pei, S. Billingsley, and S. Miura, "Grinding induced subsurface cracks in silicon wafers," *International Journal of Machine Tools and Manufacture,* vol. 39, pp. 1103-1116, 1999.

108. M. Reiche and G. Wagner, "Wafer thinning techniques for ultra-thin wafers," *Advanced Packaging,* vol. 12, pp. 29-30, 2003.

109. H. Tonshoff, B. Karpuschewski, M. Hartmann, and C. Spengler, "Grinding-and-slicing technique as an advanced technology for silicon wafer slicing," *Machining Science and Technology,* vol. 1, pp. 33-47, 1997.

110. I. Zarudi and L. Zhang, "Subsurface damage in single-crystal silicon due to grinding and polishing," *Journal of Materials Science Letters,* vol. 15, pp. 586-587, 1996.

111. S. Pinel, J. Tasselli, J. Bailbé, A. Marty, P. Puech, and D. Estève, "Mechanical lapping, handling and transfer of ultra-thin wafers," *Journal of Micromechanics and Microengineering,* vol. 8, p. 338, 1998.

112. J. N. Burghartz, *Ultra-thin chip technology and applications*: Springer, 2011.

113. N. McLellan, N. Fan, S. Liu, K. Lau, and J. Wu, "Effects of wafer thinning condition on the roughness, morphology and fracture strength of silicon die," *Journal of Electronic Packaging,* vol. 126, pp. 110-114, 2004.

114. T. Harder and W. Reinert, "Low-Profile and Flexible Electronic Assemblies Using Ultra-Thin Silicon—The European FLEX-SI Project," in *Foldable Flex and Thinned Silicon Multichip Packaging Technology*, ed: Springer, 2003, pp. 69-99.

115. M. Feil, C. Alder, G. Klink, M. König, C. Landesberger, S. Scherbaum, G. Schwinn, and H. Spöhrle, "Ultra thin ICs and MEMS elements: techniques for wafer thinning, stress-free separation, assembly and interconnection," *Microsystem technologies,* vol. 9, pp. 176-182, 2003.

116. K. Hungar and W. Mokwa, "Gold/tin soldering of flexible silicon chips onto polymer tapes," *Journal of Micromechanics and Microengineering,* vol. 18, p. 064002, 2008.

117. C. Landesberger, S. Scherbaum, G. Schwinn, and H. Spöhrle, "New process scheme for wafer thinning and stress-free separation of ultra thin ICs," *Proc. Microsyst. Technol,* pp. 431-436, 2001.

118. V. M. Benjamin Braaten, Zhong Hu, Sima Noghanian, and Isaac Chang, "Fundamental Research on Electromagnetic-Responsive Metamaterials for High Efficient Mobile Cyber-Physical Systems," unpublished|.

119. W. L. Stutzman and G. Thiele, "Antenna theory and design, 1981," *New York,* pp. 530-536.